

ABSOLUTE QUANTITATIVE MATRIX-ASSISTED LASER DESORPTION/IONIZATION MASS
SPECTROMETRY AND IMAGING MASS SPECTROMETRY OF PHARMACEUTICAL DRUGS FROM
BIOLOGICAL SPECIMENS

By

Chad Walter Chumbley

Dissertation

Submitted to the Faculty of the
Graduate School of Vanderbilt University
in partial fulfillment of the requirements
for the degree of

DOCTOR OF PHILOSOPHY

in

Chemistry

May, 2016

Nashville, Tennessee

Approved:

Richard M. Caprioli, Ph.D.

John A. McLean, Ph.D.

Kevin L. Schey, Ph.D.

David E. Cliffel, Ph.D.

Copyright © 2016 by Chad Walter Chumbley
All Rights Reserved

ACKNOWLEDGEMENTS

There are many people I would like to thank for their support and encouragement throughout this entire process. I would like to thank my advisor, Richard Caprioli, for giving me the opportunity to learn about imaging mass spectrometry in his laboratory. I truly appreciate the resources he provides and all of his guidance helping me to avoid the “trolls under the bridge” along my journey to a Ph.D. I also want to thank my current and former committee members: John McLean, David Hachey, Kevin Schey, and David Clffel. Each of you has provided excellent support and advice throughout my time at Vanderbilt.

I also want to thank Mitch Reyzer, who I affectionately refer to as my “research mom.” She introduced the idea of quantitative imaging mass spectrometry during my rotation, provided great support throughout the process, and helped me take care of the LTQ. She is also an excellent doubles partner. I want to thank Boone Prentice for enlightening discussions on linear ion traps and quantitation, which is not to be confused with “quantification.” I would like to acknowledge a fellowship from Aegis Sciences Corporation and the NIH/NIGMS grants R01-GM058008 and P41-GM103391 for funding my research. I would like to thank my collaborators: Wellington Pham and Richard McClure for starting the promethazine project and Clifton Barry, III, Laura Via, and Wendy Marriner for beginning and continuing their research on antibiotics for tuberculosis. I also want to acknowledge Tina Tsui for her efforts creating the software in MATLAB to perform quantitative imaging. I want to thank the rest of the current and past members of the Mass Spectrometry Research Center. It has been an amazing place to grow scientifically and personally. Specifically, Jamie Allen and Jessica Moore have been excellent colleagues and friends throughout the entire process of becoming who I am today.

I also want to thank my Nashville and Vanderbilt family and friends. They have definitely helped keep me sane throughout the last six years, and I really appreciate them. This includes my wonderful dog, Kimmie, who has been with me since joining the Caprioli lab. I also want to thank Alex Kammerer and our dog, Scout. Alex has definitely been my rock since I met him, and it has been great raising Scout together. I cannot wait to start the next phase of our journey together, no matter where it takes us.

I also want to recognize Darrin Smith for introducing me to analytical chemistry and allowing me to perform research in his laboratory. He encouraged me to continue with mass spectrometry toward a Ph.D. I would like to thank Chelsea Coffey for all of the long conversations about graduate school and life. Even from miles away, she has been an excellent friend. I can only hope I was able to do the same for her.

I want to thank my entire family. My dad, Farley Chumbley, and my sister, Tracie Colvin, have provided unwavering love and support. I know they are very proud of me and of what I have become. I now have a new team to always cheer for against the Kentucky Wildcats. Go Commodores!

Finally, I would like to thank my mom Rhonda Graf and Jelly Green. She has provided any and everything I have needed throughout my entire life. It certainly was not always easy, especially with an argumentative, stubborn son like me. She is the strongest person I know. She instilled in me the idea that education is very important for success, and I now will have a Ph.D. I know she is very proud, and I cannot wait to get my Henry VIII hat! It has been a long journey, but I could not have done it without her. She always believes in me, always supports me, and always loves me. I would not and could not ask for a better mom!

TABLE OF CONTENTS

	Page
ACKNOWLEDGEMENTS.....	iii
LIST OF ABBREVIATIONS	vii
LIST OF TABLES.....	viii
LIST OF FIGURES.....	x
Chapter	
I. BACKGROUND AND RESEARCH OBJECTIVES.....	1
Introduction	1
Matrix-Assisted Laser Desorption/Ionization Mass Spectrometry.....	2
Time-of-Flight/Time-of-Flight Mass Spectrometers	5
Linear Ion Trap Mass Spectrometers	8
Classic Approaches to Pharmaceutical Drug Quantitation	11
Internal Standards for Drug Quantitation in Mass Spectrometry	12
Quantitative MALDI Imaging Mass Spectrometry	13
Summary and Research Objectives	16
References	17
II. MULTIPLEXED QUANTITATIVE MATRIX-ASSISTED LASER DESORPTION/IONIZATION TANDEM MASS SPECTROMETRY OF PHARMACEUTICAL DRUGS.....	20
Introduction	20
High-Speed MALDI MS/MS Imaging Mass Spectrometry of Rifampicin.....	26
Multiplexed MS/MS from a Single Laser Shot	35
Quantitation of Enalapril in Plasma with Ramipril as the Internal Standard	41
Quantitation Assay for Multiple Drugs in Plasma using Multiplexed MS/MS.....	45
Conclusions	52
References	53

III.	METHOD DEVELOPMENT AND VALIDATION OF QUANTITATIVE MATRIX-ASSISTED LASER DESORPTION/IONIZATION IMAGING MASS SPECTROMETRY OF RIFAMPICIN DIRECTLY FROM TISSUE SECTIONS	57
	Introduction	57
	Development of a Standard Tissue Homogeneously Dosed <i>in vitro</i>	61
	Measuring the Droplet Size of the Acoustic Robotic Spotter	63
	Determining the Optimal Internal Standard Application Method for MALDI IMS.....	64
	Quantitative MALDI IMS of Liver Tissue Sections Dosed <i>in vivo</i>	75
	Quantitative MALDI IMS of Liver Using Multiplexed MALDI TOF/TOF.....	81
	Conclusions	85
	References	86
IV.	QUANTITATIVE MATRIX-ASSISTED LASER DESORPTION/IONIZATION IMAGING MASS SPECTROMETRY OF PROMETHAZINE DIRECTLY FROM LIVER AND KIDNEY TISSUE SECTIONS.....	89
	Introduction	89
	Detection of Promethazine as a Potential Probe for Amyloid Beta in the Brain	90
	Quantitative MALDI IMS of Promethazine in Liver Tissue Sections	100
	MALDI MS/MS of Calibration Standards Applied to Different Tissue Types	108
	Quantitative MALDI IMS of Promethazine in Kidney Tissue Sections	119
	Conclusions	127
	References	127
V.	CONCLUSIONS AND PERSPECTIVES.....	131
	High-Throughput MALDI MS/MS Imaging of Pharmaceutical Drugs.....	131
	Quantitative Multiplexed MALDI MS/MS of Pharmaceutical Drugs in Plasma	132
	Quantitative MALDI IMS of Pharmaceutical Drugs in Thin Tissue Sections	133
	Future Research Directions.....	135
	Conclusions	137
	References	137
VI.	APPENDIX.....	139
	Curriculum Vitae	139

LIST OF ABBREVIATIONS

A β : Amyloid Beta
CHCA: α -Cyano-4-Hydroxycinnamic Acid
CID: Collision Induced Dissociation
DC: Direct Current
DHB: 2,5-Dihydroxybenzoic Acid
ENP: Enalapril
FTICR: Fourier Transform Ion Cyclotron Resonance
Glu-Fib: [Glu1]-Fibrinopeptide B
HATCO: High-Throughput A β -Thoflavin Competitive Binding Optical
HPLC: High-Performance Liquid Chromatography
IMS: Imaging Mass Spectrometry
LLOQ: Lower Limit of Quantitation
MALDI: Matrix-Assisted Laser Desorption/Ionization
MRI: Magnetic Resonance Imaging
MS: Mass Spectrometry
MS/MS: Tandem Mass Spectrometry
MSⁿ: Tandem Mass Spectrometry
m/z: Mass-to-Charge Ratio
Nd:YAG: Neodymium-Doped Yttrium Aluminum Garnet
Nd:YLF: Neodymium-Doped Yttrium Lithium Fluoride
PET: Positron Emission Tomography
PMZ: Promethazine
PSD: Post-Source Decay
QC: Quality Control
QQQ: Triple Quadrupole
QWBA: Quantitative Whole-Body Autoradiography
RF: Radio Frequency
RIF: Rifampicin
RSD: Relative Standard Deviation
SA: Sinapinic Acid
THAP: 2,4,6-Trihydroxyacetophenone
TIS: Timed Ion Selector
TOF: Time-of-Flight
TOF/TOF: Time-of-Flight/Time-of-Flight
UV: Ultraviolet
VPM: Verapamil

LIST OF TABLES

Table	Page
2.1. Detected Abundances and Normalized Abundance Ratios for Enalapril Quantitation.....	43
2.2. Quality Control Results for Enalapril Quantitation in Plasma.....	44
2.3. Detected Abundances and Abundance Ratios of Promethazine, Enalapril, and Verapamil in Plasma.....	49
2.4. Quality Control Results for Promethazine, Enalapril, and Verapamil in Plasma	50
3.1. Rifampicin Concentrations of Tissues Dosed <i>in vitro</i> Detected using Different Methods of MALDI IMS Standard Application and HPLC-MS/MS.....	70
3.2. Analysis of Variance for Different Methods of MALDI IMS Standard Application on Standard Tissue 1 Dosed <i>in vitro</i>	71
3.3. Analysis of Variance for Different Methods of MALDI IMS Standard Application on Standard Tissue 2 Dosed <i>in vitro</i>	71
3.4. Post Hoc Tukey Test for Differences for Different Methods of MALDI IMS Standard Application on Standard Tissue 1 Dosed <i>in vitro</i>	72
3.5. Post Hoc Tukey Test for Differences for Different Methods of MALDI IMS Standard Application on Standard Tissue 2 Dosed <i>in vitro</i>	73
3.6. Relative Standard Deviations and Quality Control Errors for Four Trials of Quantitative MALDI IMS on a Liver Tissue Dosed <i>in vivo</i> with Rifampicin	78
3.7. Rifampicin Concentrations Detected Using HPLC-MS/MS and MALDI IMS from a Liver Tissue Dosed <i>in vivo</i>	79
4.1. Promethazine Concentrations Detected Using HPLC-MS/MS and MALDI IMS from Liver Tissues of 5XFAD and Wildtype Mice Dosed <i>in vivo</i>	107
4.2. Analysis of Variance for the Intensities of the Internal Standard Detected from the 5.00 μ M PMZ Calibration Standard on Different Tissue Types.....	110
4.3. Analysis of Variance for the Intensities of the Internal Standard Detected from the 10.0 μ M PMZ Calibration Standard on Different Tissue Types.....	110

4.4. Analysis of Variance for the Intensities of the Internal Standard Detected from the 20.0 μM PMZ Calibration Standard on Different Tissue Types	111
4.5. Analysis of Variance for the Intensities of the Internal Standard Detected from the 40.0 μM PMZ Calibration Standard on Different Tissue Types	111
4.6. Analysis of Variance for the Intensities of the Internal Standard Detected from the 75.0 μM PMZ Calibration Standard on Different Tissue Types	111
4.7. Post Hoc Tukey Test for Differences in the Detected Internal Standard Intensities from the 5.00 μM PMZ Calibration Standard on Different Tissue Types	113
4.8. Post Hoc Tukey Test for Differences in the Detected Internal Standard Intensities from the 10.0 μM PMZ Calibration Standard on Different Tissue Types	114
4.9. Post Hoc Tukey Test for Differences in the Detected Internal Standard Intensities from the 20.0 μM PMZ Calibration Standard on Different Tissue Types	115
4.10. Post Hoc Tukey Test for Differences in the Detected Internal Standard Intensities from the 40.0 μM PMZ Calibration Standard on Different Tissue Types	116
4.11. Post Hoc Tukey Test for Differences in the Detected Internal Standard Intensities from the 75.0 μM PMZ Calibration Standard on Different Tissue Types	117
4.12. Promethazine Concentrations Detected Using HPLC-MS/MS and MALDI IMS from Kidney Tissues of 5XFAD and Wildtype Mice Dosed <i>in vivo</i>	126

LIST OF FIGURES

Figure	Page
1.1. Schematic of the MALDI Process	3
1.2. Diagram of a MALDI TOF/TOF Mass Spectrometer	7
1.3. Diagram of a MALDI Linear Ion Trap Mass Spectrometer	8
1.4. Graphical Representation of the Mathieu Equations for Three m/z Values	10
1.5. Workflow for MALDI IMS	15
2.1. Graphical Representation of the Relationship between the Number of Pixels and Spatial Resolution in MALDI IMS	21
2.2. Full Scan MALDI IMS of a Lipid and Rifampicin in a Kidney Dosed <i>in vitro</i>	29
2.3. MALDI MS/MS Image of Rifampicin in a Kidney Dosed <i>in vitro</i>	31
2.4. Full Scan MALDI IMS and MALDI MS/MS Image of Rifampicin in a Liver Dosed <i>in vivo</i>	34
2.5. Schematic of Multiplexed MS/MS with a MALDI TOF/TOF Mass Spectrometer	36
2.6. Multiplexed MS/MS Analysis of Two Peptide Ions	38
2.7. Multiplexed MS/MS Spectrum and Individual MS/MS Spectra of Ramipril and Enalapril....	39
2.8. Calibration Curves of Enalapril and Enalapril Normalized to Ramipril	44
2.9. Multiplexed MS/MS Spectrum and Individual MS/MS Spectra of Promethazine, Enalapril, and Verapamil	48
2.10. Calibration Curves for Promethazine, Enalapril, and Verapamil With and Without Normalization.....	51
3.1. Illustration of Four Methods of Applying Internal and Calibration Standards for Quantitative MALDI IMS	59
3.2. MALDI IMS of a Standard Tissue Dosed <i>in vitro</i> with Rifampicin	62

3.3. Diagram of a MALDI Target with the Applied Microspots for Analyzing Different Methods of MALDI IMS Standard Application.....	66
3.4. MALDI MS/MS Product Ion Spectra of Rifampicin and its Internal Standard on Liver.....	67
3.5. Calibration Curves for Different Methods of MALDI IMS Standard Application and the Detected Rifampicin Concentrations from Tissues Dosed <i>in vitro</i>	69
3.6. Graphs of the Average Detected Intensities for Rifampicin and for the Internal Standard when using Different Methods of MALDI Standard Application on Tissues Dosed <i>in vitro</i>	74
3.7. Quantitative MALDI MS/MS Image of Rifampicin in a Liver Tissue Dosed <i>in vivo</i>	77
3.8. Repeat Quantitative MALDI MS/MS Images of Rifampicin in a Liver Tissue Dosed <i>in vivo</i> ..	80
3.9. Multiplexed MS/MS Spectrum of Rifampicin and Rifapentine and Calibration Curve of Rifampicin Deposited onto Non-Dosed Liver Tissue	83
3.10. Quantitative MALDI IMS of Rifampicin in a Liver Tissue Dosed <i>in vivo</i> using Multiplexed MALDI TOF/TOF	84
4.1. High-Throughput Amyloid Beta-Thioflavin Competitive Binding Optical Assay with Different Compounds.....	94
4.2. MALDI IMS Workflow for Analyzing the Same Tissue Section for Promethazine and Amyloid Beta Peptides	96
4.3. MALDI IMS of Wildtype and 5XFAD Mouse Brains for Promethazine and Amyloid Beta	98
4.4. Tandem Mass Spectrum for the Identification of an Amyloid Beta Peptide.....	99
4.5. MALDI MS/MS Product Ion Spectrum of Promethazine and its Internal Standard on Liver Tissue	103
4.6. MALDI MS/MS Calibration Curve and Quantitative MALDI IMS of Promethazine in Liver Tissue Sections	104
4.7. HPLC-MS/MS Calibration Curves of Promethazine in Liver Tissue Homogenates	106
4.8. Detected Internal Standard Intensities for Promethazine Calibration Standards Deposited on Different Tissue Types	110
4.9. MALDI MS/MS Calibration Curves of Promethazine on Different Tissue Types	118

4.10. MALDI MS/MS Product Ion Spectra of Promethazine and its Internal Standard on Kidney Tissue	121
4.11. Quantitative MALDI IMS of Promethazine in Dosed Kidneys and MALDI MS/MS Calibration Curves of Promethazine Deposited onto the Cortex and Medulla of Kidney Tissue	123
4.12. MALDI IMS of Promethazine in a Dosed Kidney	124
4.13. HPLC-MS/MS Calibration Curves of Promethazine in Kidney Tissue Homogenates	125

CHAPTER I

BACKGROUND AND RESEARCH OBJECTIVES

Introduction

The pharmaceutical drug discovery and development process is arduous, taking an average of 10-15 years from start to finish for a single drug.¹ Mass spectrometry (MS), pioneered by J. J. Thomson in the early twentieth century,^{2, 3} is commonly used throughout this process to evaluate molecular targets, identify proteins and/or peptides, characterize potential pharmaceutical drug candidates, and quantify various analytes of interest. After discovering a potential pharmaceutical drug, research into its absorption, distribution, metabolism, excretion, and toxicology begin along with *in vitro* and *in vivo* pharmacodynamics and pharmacokinetics studies. These results provide insight into what the potential therapeutic does, how it works, and the side effects or safety issues it may cause.

Understanding the quantitative distributions of a potential therapeutic and its metabolite(s) is critically important for evaluating its efficacy and toxicity. Classic approaches to pharmaceutical drug quantitation include high-performance liquid chromatography-mass spectrometry (HPLC-MS) and quantitative whole-body autoradiography (QWBA). Though both technologies provide quantitative information about a therapeutic, quantitative matrix-assisted laser desorption/ionization (MALDI) imaging mass spectrometry (IMS) combines the benefits of these two approaches into a single analysis. MALDI IMS provides molecular specificity by directly detecting the analyte of interest while maintaining the spatial localization throughout a

thin tissue section. Fully validating quantitative MALDI IMS, however, remains a challenge, because few other technologies have the capability of quantitatively analyzing individual analytes in regions the size of a single pixel in an imaging experiment (~10-500 μm diameter spot on a 3-20 μm thick tissue section).

Matrix-Assisted Laser Desorption/Ionization Mass Spectrometry

MS is an analytical technology allowing for the detection of analytes without prior knowledge of the particular analytes of interest. MS requires the detection of analytes as either positive or negative ions in the gas phase, and the mass spectrometer detects these ions by their mass-to-charge ratios (m/z). These analyses may be targeted for a particular m/z or untargeted analyzing for all m/z values within a range. One method for ion generation is MALDI, which was developed concurrently in the late 1980s by Koichi Tanaka⁴ and Franz Hillenkamp^{5, 6} as a soft ionization method for biomolecules. MALDI has been utilized to analyze many types of biomolecules including metabolites, pharmaceutical drugs, lipids, peptides, and proteins.

In a MALDI experiment the analyte(s) of interest must first be mixed and co-crystallized with a matrix. Most matrixes are small, organic acids used to aid the processes of desorbing and ionizing the analytes. The matrix absorbs the incident photon energy from the laser and allows for the desorption and ionization of analytes typically into singly charged ions (Figure 1.1). Ultraviolet MALDI MS instruments are equipped with lasers using nitrogen (N_2 - 337 nm), frequency tripled neodymium-doped yttrium aluminum garnet (Nd:YAG - 355 nm), or frequency tripled neodymium-doped yttrium lithium fluoride (Nd:YLF - 349 nm). Some common matrices absorbing light in this wavelength regime include sinapinic acid (SA), α -cyano-4-

hydroxycinnamic acid (CHCA), 2,5-dihydroxybenzoic acid (DHB), and 2,4,6-trihydroxyacetophenone (THAP). The ions produced by MALDI typically are singly charged with little fragmentation caused by the ionization process allowing for easy spectral interpretation. The ions fragmented by this process can be used for structural confirmation as described later.

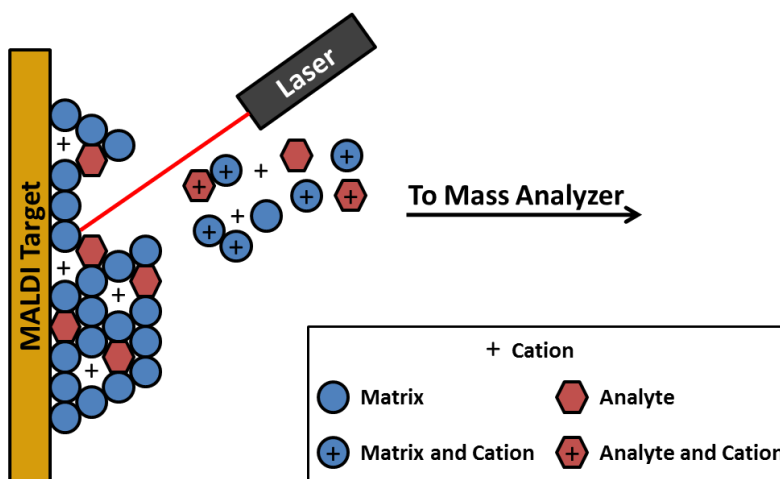


Figure 1.1. Schematic of the MALDI process. A laser is used to irradiate the mixture of the analyte and the matrix. The matrix absorbs the incident laser energy and aids the desorption and ionization of the analytes. Ions from the matrix and analyte are pulsed toward the mass analyzer.

The analysis of small molecules, including pharmaceutical drugs, using MALDI MS is complicated by their small molecular weights. Because the matrix is also a small molecule, it can yield signals interfering with signal from the pharmaceutical drug. Different mass spectrometric techniques have been developed to distinguish analytes of interest from interfering ions. Two approaches for detecting a particular analyte of interest using MALDI MS include using a high mass resolving power instrument or an instrument capable of performing tandem mass spectrometry (MS/MS or MSⁿ).

The use of an instrument with high mass resolving power allows for the separation of analytes of interest from background ions based upon the accurate measurement of their unique m/z . This provides an untargeted analysis in which no knowledge of the analytes of interest is required prior to performing the experiment. Instruments with high mass accuracy and high resolving power include Fourier transform ion cyclotron resonance (FTICR)⁷⁻¹⁰ and orbitrap¹¹⁻¹³ mass spectrometers. However, these instruments do not have the capability of distinguishing isobaric species, since they depend upon measuring accurate masses. Other separation methods are required before mass analysis to identify these species with these instruments.

When performing tandem mass spectrometry, the precursor ion for the analyte of interest is selected and fragmented into unique fragment ions. The fragment ions are detected and used to confirm the structural identity of the precursor ion.¹⁴ Therefore, these experiments must be targeted for a known analyte of interest. Instruments capable of tandem mass spectrometry include hybrid mass spectrometers, such as triple quadrupole mass spectrometers^{15, 16} or time-of-flight/time-of-flight mass spectrometers (TOF/TOF),¹⁷ and ion trap mass spectrometers,¹⁸ such as linear or three-dimensional ion trap and FTICR mass spectrometers. Hybrid mass spectrometers perform tandem in space mass measurements in which the isolation and fragmentation components are physically separated from one another. Ion trap and FTICR mass spectrometers perform tandem in time mass measurements in which the ions remain in the same location throughout the isolation and fragmentation processes. This allows for MSⁿ analyses in which iterations of isolation and fragmentation can be performed for further structural confirmation. For example, MS³ analysis involves the isolation and fragmentation of

a precursor ion's fragment ion into its fragment ions to obtain ions specific to the molecule's chemical structure.

Time-of-Flight/Time-of-Flight Mass Spectrometers

Hybrid instruments employing tandem in space fragmentation, such as TOF/TOF mass spectrometers, are inherently faster for MS/MS analyses than those implementing tandem in time fragmentation.^{17, 19} Lasers with repetition rates of 5 kHz have recently been added to MALDI TOF and MALDI TOF/TOF mass spectrometers to allow for rapid MALDI analysis.¹⁹⁻²¹ These instruments do not require trapping the ions within a particular region of the instrument; instead, they allow the ions to continue their trajectory while being fragmented by neutral gas molecules.

TOF mass analysis is derived from the time required for an ion with a given kinetic energy to traverse a field-free region. All ions are given the same kinetic energy by an accelerating electrode. Therefore, ions with different masses have differing velocities, causing them to reach the detector at the end of the field-free region at different times. The kinetic energy of an ion is described by Equation 1.1.

$$KE = zU = \frac{1}{2}mv^2$$

Equation 1.1. Kinetic energy equation for an ion accelerated by an electric field. KE is the kinetic energy of the ion, U represents the acceleration voltage, z is the charge of the ion, *m* is the mass of the ion, and *v* is the velocity of the ion.

Because all ions are given the same kinetic energy and velocity is defined as the distance covered over the course of time, the time required for a particular ion to reach the detector is obtained using Equation 1.2. The distance covered is equal to the length of the flight tube for that particular TOF mass analyzer.

$$t = d \sqrt{\frac{m}{2zU}}$$

Equation 1.2. Time-of-flight equation for a particular ion. The time, t , required for an ion to travel a distance, d , with an acceleration voltage, U , is proportional to the mass-to-charge ratio (m/z) of the ion.

Based upon Equation 1.2, the m/z of an ion is proportional to the time it takes to travel the length (d) of the flight tube. Therefore, ions with high m/z values will reach the detector at a later time than those with smaller m/z values. In a TOF/TOF configuration (Figure 1.2), these equations apply to the parent ions prior to the timed ion selector (TIS) and the fragment ions when they are reaccelerated for the second TOF mass analysis. The fragment ions allow for the structural confirmation of the precursor ion and provide specificity in the analysis.

MALDI TOF/TOF mass spectrometers have the capability of delivering rapid tandem mass spectrometric analyses of multiple samples on a single target.¹⁹ The first TOF mass analyzer is used to separate the precursor ions generated by MALDI. Fragmentation of the ions often occurs by post-source decay (PSD) within these instruments. In PSD, residual energy from the MALDI process results in fragmentation of the ions after they have exited the source of the instrument but before they reach the second TOF source.²²⁻²⁵ Because fragmentation occurs

after the initial acceleration, the fragment ions have the same velocity as the precursor ion and can be selected by a TIS for reacceleration into the second field-free region TOF mass analyzer. The TIS for a TOF/TOF MS can typically isolate a window of m/z 3.0-5.0 based upon the time-of-flight of the precursor ion. The second TOF mass analyzer measures the masses of the fragment ions generated from the precursor ions. A reflectron may also be used in the second analyzer region. The reflectron generates an electric field to repel the ions toward the detector. This expands the time-of-flight region and reduces the dispersion of ions with the same m/z .

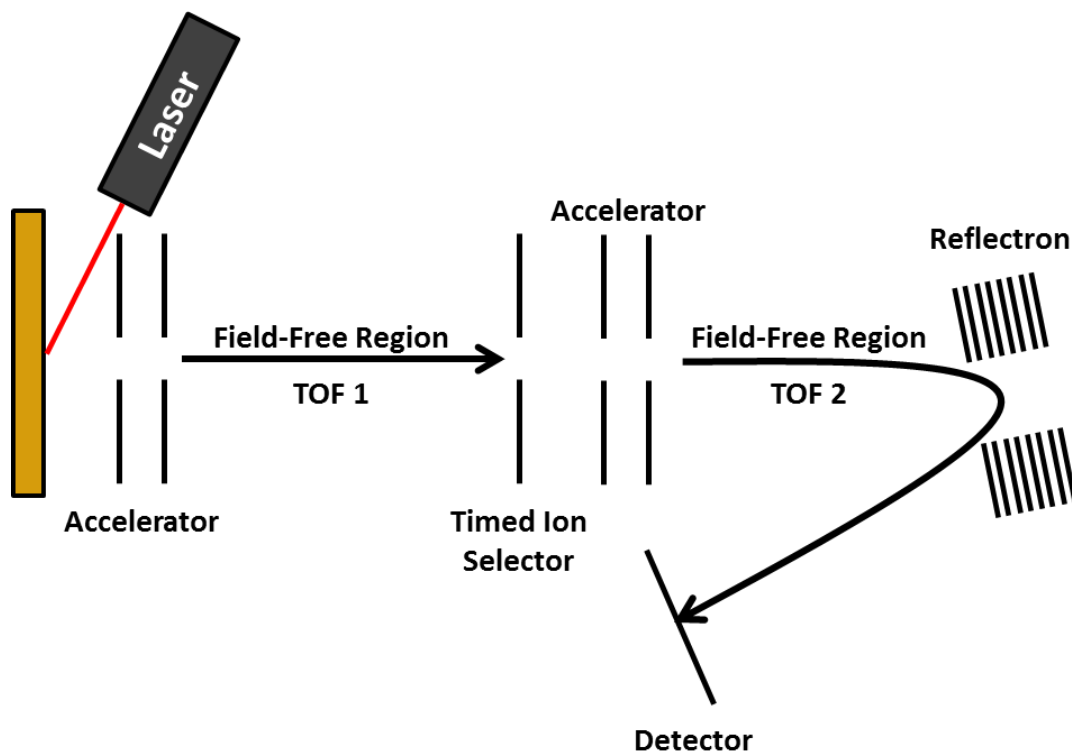


Figure 1.2. Diagram of a MALDI TOF/TOF mass spectrometer. The ions are generated by MALDI and accelerated through the first field-free region (TOF 1) to separate the precursor ions. A timed ion selector selects the precursor ion of interest and reaccelerates it and the fragment ions created by PSD through a second field free region (TOF 2) with a reflectron to the detector.

Linear Ion Trap Mass Spectrometers

Because of its MS^n capabilities, a linear ion trap mass spectrometer has been used for many small molecule and pharmaceutical drug applications.²⁶ Once ions are generated by MALDI in the case of the MALDI LTQ XL (Thermo Scientific, Waltham, MA), there are two quadrupoles and an octapole to guide the ions into a segmented linear ion trap (Figure 1.3). The ion trap stores the ions generated from the sample. These ions may be scanned for mass analysis or an ion of interest may be isolated and fragmented using collision induced dissociation (CID). In CID, neutral gas molecules are leaked into the trap to collide with the selected ions of interest to induce fragmentation. This version of the linear ion trap allows for radial ejection of the ions through slits in the rods to two different detectors.

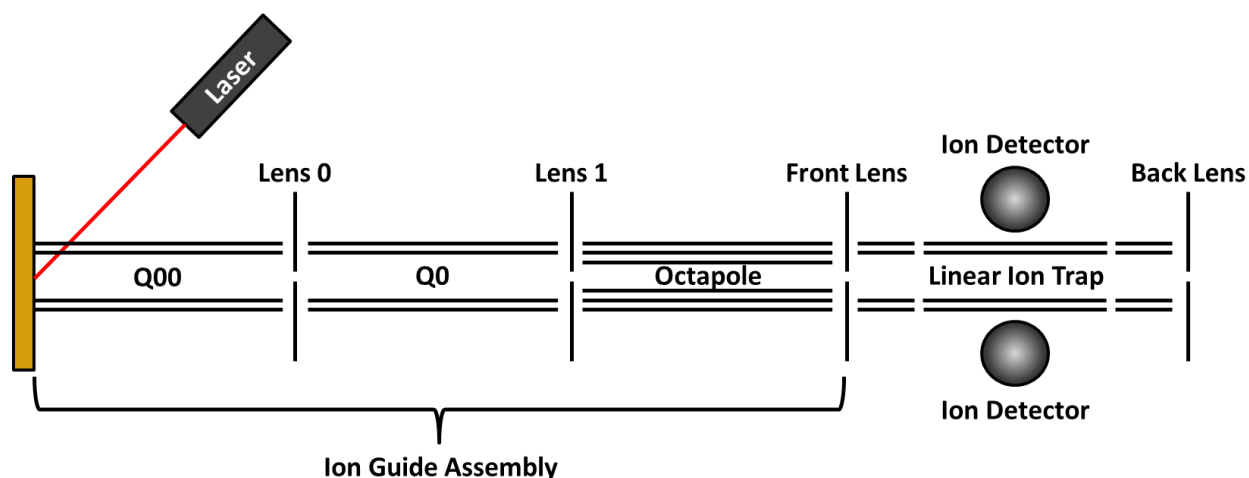


Figure 1.3. Diagram of a MALDI linear ion trap mass spectrometer. The ions are generated by MALDI and directed into the segmented ion trap by two quadrupoles (Q00 and Q0) and an octapole. The ions are trapped by the front and back lenses. Upon scanning the voltages in the trap, the ions are ejected radially through slits in the rods into two different detectors.

In a typical scan on a linear ion trap, the amplitude of the radio frequency (RF) potential is linearly ramped allowing for the ejection of increasing m/z values to the detectors. The ions ejected from the trap can be determined using a stability diagram generated by graphing the known solutions to the Mathieu equations (Equation 1.3).^{27, 28} Ions with solutions located within the bounds of the two equations have a stable trajectory and are contained within the ion trap. Ions outside of this region, however, have unstable trajectories and are ejected from the ion trap.²⁹

$$a_x = -a_y = \frac{8zU}{mr_0^2\Omega^2}$$

$$q_x = -q_y = -\frac{4zV}{mr_0^2\Omega^2}$$

Equation 1.3. Mathieu equations for the stability of ions in a quadrupole linear ion trap. These equations form the borders of the stability diagram indicating which ions have stable trajectories based upon the applied potentials. The subscripts x and y represent the motions perpendicular to and between the end caps, respectively, z is the charge of the ion, m is the mass of the ion, r_0 is the inscribed radius of the ring electrode, Ω is the angular RF frequency, U is the applied direct current potential, and V is the applied RF potential.

A graphical representation of the Mathieu equations demonstrating the stability diagrams for three different m/z values ($m/z C > m/z B > m/z A$) is shown in Figure 1.4. As demonstrated in the graph, different m/z values have different stability diagrams based upon the Mathieu equations. Altering the combination of applied RF and direct current (DC) voltages influences whether ions with a particular m/z ratio are stable within the trap. If the combination of applied RF and DC voltages is outside of the stability diagram for a particular m/z value, those ions will develop an unstable trajectory and be ejected from the ion trap. If the combination is

within the bounds of the stability diagram, the ions with that m/z value will remain in the linear ion trap. Furthermore, a particular m/z of interest can be isolated within the ion trap by utilizing a voltage combination near the apex of its stability diagram. This would yield an unstable trajectory for other m/z values causing those ions to be ejected. A typical ion trap has the capability of isolating a window of m/z 0.5-1.0.

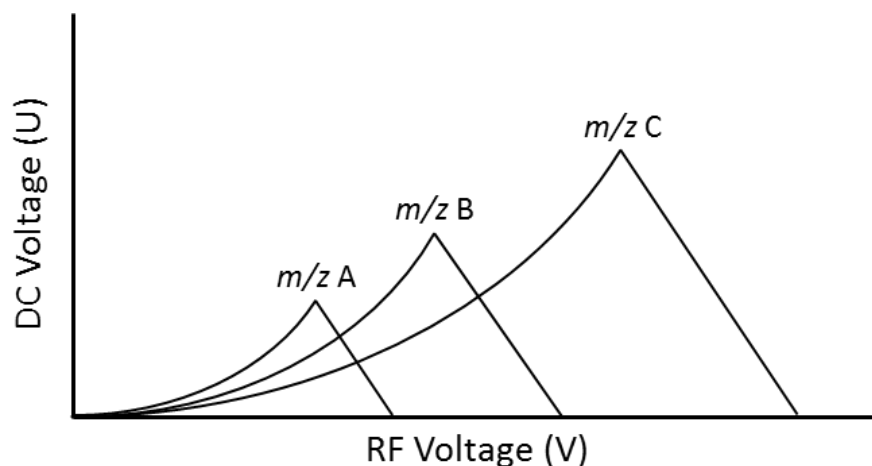


Figure 1.4. Graphical representation of the Mathieu equations for three different m/z values ($m/z C > m/z B > m/z A$) showing the bounds of their stability diagrams. Voltage combinations within the bounds of the lines allow for the stability of the ion of interest. Combinations outside of the lines cause instability and ejection of that particular m/z value.

CID is commonly used when performing tandem mass spectrometry in a linear ion trap to fragment molecules of interest for structural confirmation.³⁰ The dissociation of the ion of interest occurs after an energetic collision between the accelerated ion and thermally neutral target molecules, such as an inert gas. Within the quadrupole ion trap, CID is performed by accelerating the precursor ions with a supplemental alternating current applied to the end-cap electrodes. These collisions with inert gas molecules convert the kinetic translational energy

into internal energy. Because of this increase in internal energy, the precursor ion fragments into smaller ions. Detection of the fragment ions allows for the structural confirmation of the precursor ion and for further specificity in the analysis.

Classic Approaches to Pharmaceutical Drug Quantitation

Initially, small molecule quantitation was performed using high-performance liquid chromatography (HPLC) coupled to ultraviolet (UV) detection. UV detection requires the analyte of interest to contain a chromophore absorbing wavelengths of light in the range of 190-400 nm.³¹⁻³⁴ These methods, however, limit the quantitation to only those compounds containing a chromophore and lack specificity if the analyte of interest is metabolized and/or elutes at the same retention time. Today, pharmaceutical drug quantitation from dosed tissues typically involves either performing HPLC-MS or QWBA for the analysis. While both technologies provide quantitative measurements of a pharmaceutical drug in dosed tissues, neither provides the spatial specificity and molecular specificity provided by quantitative MALDI IMS analyses.

Considered the gold standard for pharmaceutical drug quantitation from tissue, HPLC-MS analyses require homogenization of the tissue.^{35, 36} The analytes of interest are then extracted from the tissue homogenate into a solvent, and the extract is analyzed using HPLC-MS. HPLC separates the analytes of interest from the biological matrix, and the detection of a particular m/z for each analyte using MS allows for that analyte to be accurately quantified. Because of the homogenization procedure, however, this analysis does not provide the spatial distribution of the analytes within the tissue. For example, when a kidney is homogenized and a pharmaceutical drug is quantified in the homogenate, the quantitative concentrations in the

medulla and cortex regions in the kidney remain unknown. These tissue microenvironments can be very important for pharmacokinetics, pharmacodynamics, and toxicity studies.³⁷

QWBA is a technology in which a radioactive label on the analyte of interest is required for detection.³⁸⁻⁴⁰ A radioactive analogue of the pharmaceutical drug must first be administered to the animal being studied. The analogue is metabolized normally, and after sacrificing the animal, the quantitative distribution of the radioactive label is measured in a thin tissue section using autoradioluminography or autoradiography. This technology provides spatial information throughout the tissue section but may provide false information with respect to the compound. For example, when the analogue is metabolized, the radioactive label may be cleaved or conserved but would still be detected by the instrument. Therefore, metabolites as well as the pharmaceutical drug are detected and quantified in this type of analysis.

Because HPLC-MS does not allow for the spatial distribution of a pharmaceutical drug to be detected and QWBA does not provide the molecular specificity to detect only the pharmaceutical drug of interest, quantitative MALDI IMS has emerged. Quantitative IMS allows for the detection of a particular m/z across a thin tissue section, combining the benefits of both technologies into a single analysis.

Internal Standards for Drug Quantitation in Mass Spectrometry

Because of the complex biological matrix present within tissues, an internal standard is commonly used to account for the dilution, derivatization, extraction, ionization variability, and sample heterogeneity that may be present in a quantitative MS experiment.⁴¹ In order to provide accurate quantitation, the internal standard should have similar chemical properties to the analyte of interest allowing it to mimic the extraction, derivatization, ionization efficiency,

and interaction of the analyte in tissues from dosed animals.⁴² The optimal internal standard meeting these requirements is a stable, isotopically labeled analogue of the analyte of interest. Though it typically requires specialized synthesis and can be expensive, an isotopically labeled analogue is the most structurally and chemically similar compound to the analyte of interest.

Internal standards are added at the beginning of the experiment prior to performing any sample preparation required for the analysis. This ensures the internal standard will account for potential systematic errors in the experiment. This also allows the internal standard to interact with the biological matrix throughout the entire analytical procedure. Additionally, the amount of the added internal standard should be above the limit of quantitation for the experiment but should not suppress the ionization of the analyte of interest. Therefore, the internal standard should be added in a concentration within the analytical calibration curve of the experiment.

Quantitative MALDI Imaging Mass Spectrometry

Since MALDI IMS was first utilized to detect peptides, proteins, and pharmaceutical drugs directly from thin tissue sections, it has become an increasingly important tool to elucidate the distribution of compounds within tissues of interest.⁴³⁻⁴⁵ Because of the wide range of molecules suitable for detection, MALDI IMS has many diverse applications within the medicinal and pharmaceutical drug discovery fields. MALDI IMS may be applied to large tissue sections if spatial resolution is not paramount for the experiment, and it may be applied at higher spatial resolutions to small areas of a tissue section. For example, pharmaceutical drug distributions throughout an entire mouse tissue section at a spatial resolution of 400 μm ⁴⁶ and within a kidney tissue section at a spatial resolution of 10 μm ⁴⁷ have been elucidated using this

technology. Drug distributions have also been measured with peptide and protein distributions within brain tissue sections to reveal potential interactions.⁴⁸ These measurements provide information about the localization, metabolism, and mechanism of action for a pharmaceutical drug after administration.

In a typical MALDI IMS experiment (Figure 1.5) a cryostat is used to cut a thin tissue section, which is thaw-mounted onto a MALDI target. Samples for IMS may be as large as an entire animal⁴⁶ or as small as a single cell.⁴⁹ The tissue sections are typically 3-20 μm thick, and the target may be a glass slide or gold-coated stainless steel. Matrix is added to the target either as a homogeneous coating or in a spotted array. For a homogeneous coating, a solution of matrix may be sprayed onto the surface, or the matrix may be sublimated onto the target. A spotted array of matrix may be deposited manually, with a robotic spotter,⁵⁰ or with an inkjet printer.⁵¹ After matrix deposition, the laser is fired at the target in a raster pattern to generate ions and a mass spectrum at each x and y location across the tissue. In the case of a spotted array of matrix, the laser fires at each matrix spot on the tissue. The spatial resolution of the image is a function of the laser spot size and the lateral distance between laser shots on the tissue section. With a spotted array, the spatial resolution is dictated by the distance between each matrix spot. Molecular images are generated by plotting the intensity of the m/z value of interest in the spectrum at each coordinate location. Molecular images may be generated for any m/z value detected by the mass spectrometer.

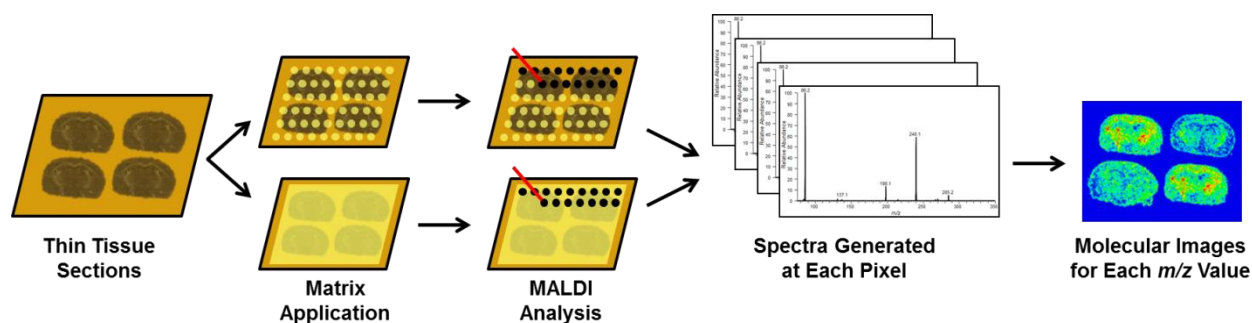


Figure 1.5. Workflow for MALDI IMS. Thin tissue sections are first thaw-mounted onto a MALDI target. Matrix is applied either as a spotted array or as a homogeneous coating. The laser is fired in a raster pattern across the sample to collect spectra. An image is generated by plotting the intensity of the m/z values across the tissue sections.

The quantitative capabilities of MALDI MS have been explored greatly to reduce the preparation and analysis time required for many HPLC-MS experiments.^{52, 53} The potential for quantitative MALDI IMS has typically been reported through the correlation of MALDI IMS signal response to that from classical analytical techniques such as HPLC-MS,^{45, 54-56} QWBA,⁵⁶ and gas chromatography with electron capture detection.⁵⁷ Absolute pixel-to-pixel quantitation by MALDI IMS in which each pixel in the image represents an accurate quantitative value of the detected analyte, however, is challenging because of matrix and tissue heterogeneity, inefficient analyte extraction, and ionization suppression effects.

One approach to quantitative MALDI IMS is the creation of surrogate tissue models in which a tissue homogenate dosed with varying concentrations of the analyte is prepared and then compared to an entire tissue section from a tissue dosed *in vivo*.⁹⁻¹¹ This requires preparing a tissue homogenate spiked with different concentrations of the drug for each microenvironment in a tissue. For example, both the medulla and cortex of the kidney or the white and grey matter of the brain would have to be prepared. This may not be feasible with smaller

microenvironments within a particular tissue. Others have used a tissue extinction coefficient that must be evaluated for each analyte in every microenvironment of the tissue.¹² This also may not be feasible for smaller microenvironments within a particular tissue section. Finally, a standard addition method in which calibration standards are applied to the dosed tissue section has also been utilized to determine the concentration of small molecules in tissue sections by MALDI IMS.¹³⁻¹⁵ Though data utilizing these published methods correspond well with HPLC-MS results, they remove the spatial advantage of MALDI IMS by reducing the analysis to a bulk quantitative measurement of the analyte within the entire tissue section, thereby largely ignoring the microenvironments.¹⁶

Utilizing a stable, isotopically labeled internal standard has been reported to mitigate many of the heterogeneity, extraction, and suppression effects on absolute quantitation with MALDI IMS, but it has only been validated for entire tissue sections in bulk.⁵⁸⁻⁶¹ The application and analysis of the isotopically labeled internal standard and calibration standards have not been validated at the size regime of single pixels within an image (~10-1,000 μm diameter spot on a 3-20 μm thick tissue section). Therefore, limited spatial information has been obtained using these published methods.⁶²⁻⁶⁴

Summary and Research Objectives

The objectives of this dissertation are to develop a multiplexed quantitative MALDI MS/MS quantitation assay as well as quantitative pixel-to-pixel MALDI IMS. Both methods were developed to analyze pharmaceutical drugs in biological specimens using internal standards. Initially, a high-throughput, multiplexed quantitative MALDI MS/MS assay was developed using a high-speed MALDI TOF/TOF mass spectrometer to analyze pharmaceutical drugs in plasma.

The use of internal standards was imperative to these experiments allowing for more accurate and precise quantitation. Next, a method to homogeneously dose a tissue *in vitro* with a pharmaceutical drug was developed to determine the optimal method of robotically microspotting internal standards for quantitative MALDI IMS. Finally, quantitative MALDI IMS was used to determine the distributions of two drugs in different tissue types after the animals were dosed *in vivo*.

The developments of multiplexed MS/MS on a high-speed MALDI TOF/TOF platform and quantitative MALDI IMS methodologies allowed for important advancements in the scientific community. Multiplexed MS/MS allows for higher throughput along with structural confirmation when screening plasma for different pharmaceutical drugs at both therapeutic and toxic levels. Quantitative MALDI IMS allows for the direct quantitation of pharmaceutical drugs in relation to histological and anatomical features within tissue sections, providing unparalleled information about drugs and their targets.

References

1. T. Kennedy, *Drug Discovery Today*, 1997, **2**, 436-444.
2. J. J. Thomson, *Philosophical Magazine*, 1907, **13**, 561-575.
3. J. J. Thomson, *Philosophical Magazine*, 1910, **20**, 752-767.
4. K. Tanaka, H. Waki, Y. Ido, S. Akita, Y. Yoshida and T. Yoshida, *Rapid Communications in Mass Spectrometry*, 1988, **2**, 151-153.
5. M. Karas, D. Bachmann, U. Bahr and F. Hillenkamp, *International Journal of Mass Spectrometry and Ion Processes*, 1987, **78**, 53-68.
6. M. Karas and F. Hillenkamp, *Analytical Chemistry*, 1988, **60**, 2299-2301.
7. M. B. Comisaró and A. G. Marshall, *Chemical Physics Letters*, 1974, **25**, 282-283.
8. I. J. Amster, *Journal of Mass Spectrometry*, 1996, **31**, 1325-1337.
9. A. G. Marshall, C. L. Hendrickson and G. S. Jackson, *Mass Spectrometry Reviews*, 1998, **17**, 1-35.
10. A. G. Marshall and C. L. Hendrickson, *International Journal of Mass Spectrometry*, 2002, **215**, 59-75.
11. A. Makarov, *Analytical Chemistry*, 2000, **72**, 1156-1162.
12. M. Hardman and A. Makarov, *Analytical Chemistry*, 2003, **75**, 1699-1705.

13. Q. Z. Hu, R. J. Noll, H. Y. Li, A. Makarov, M. Hardman and R. G. Cooks, *Journal of Mass Spectrometry*, 2005, **40**, 430-443.
14. E. deHoffmann, *Journal of Mass Spectrometry*, 1996, **31**, 129-137.
15. R. A. Yost and C. G. Enke, *Analytical Chemistry*, 1979, **51**, 1251-&.
16. D. F. Hunt, J. Shabanowitz and A. B. Giordani, *Analytical Chemistry*, 1980, **52**, 386-390.
17. K. Schey, R. G. Cooks, R. Grix and H. Wollnik, *International Journal of Mass Spectrometry and Ion Processes*, 1987, **77**, 49-61.
18. J. N. Louris, R. G. Cooks, J. E. P. Syka, P. E. Kelley, G. C. Stafford and J. F. J. Todd, *Analytical Chemistry*, 1987, **59**, 1677-1685.
19. B. M. Prentice, C. W. Chumbley and R. M. Caprioli, *Journal of Mass Spectrometry*, 2015, **50**, 703-710.
20. P. J. Trim, M. Djidja, S. J. Atkinson, K. Oakes, L. M. Cole, D. M. G. Anderson, P. J. Hart, S. Francese and M. R. Clench, *Analytical and Bioanalytical Chemistry*, 2010, **397**, 3409-3419.
21. J. M. Spraggins and R. M. Caprioli, *Journal of the American Society for Mass Spectrometry*, 2011, **22**, 1022-1031.
22. X. J. Tang, W. Ens, K. G. Standing and J. B. Westmore, *Analytical Chemistry*, 1988, **60**, 1791-1799.
23. U. Boesl, R. Weinkauff and E. W. Schlag, *International Journal of Mass Spectrometry and Ion Processes*, 1992, **112**, 121-166.
24. R. Kaufmann, D. Kirsch and B. Spengler, *International Journal of Mass Spectrometry and Ion Processes*, 1994, **131**, 355-385.
25. D. Suckau, A. Resemann, M. Schuerenberg, P. Hufnagel, J. Franzen and A. Holle, *Analytical and Bioanalytical Chemistry*, 2003, **376**, 952-965.
26. D. J. Douglas, A. J. Frank and D. M. Mao, *Mass Spectrometry Reviews*, 2005, **24**, 1-29.
27. J. C. Schwartz, M. W. Senko and J. E. P. Syka, *Journal of the American Society for Mass Spectrometry*, 2002, **13**, 659-669.
28. J. W. Hager, *Rapid Communications in Mass Spectrometry*, 2002, **16**, 512-526.
29. R. E. March, *Journal of Mass Spectrometry*, 1997, **32**, 351-369.
30. S. A. McLuckey, G. J. Vanberkel and G. L. Glish, *Journal of the American Society for Mass Spectrometry*, 1992, **3**, 60-70.
31. C. A. Burtis, *Journal of Chromatography*, 1970, **52**, 97-&.
32. G. Alibert, *Journal of Chromatography*, 1973, **80**, 173-185.
33. W. Lindner, R. W. Frei and W. Santi, *Journal of Chromatography*, 1975, **111**, 365-371.
34. C. Frahnert, M. L. Rao and K. Grasmader, *Journal of Chromatography B-Analytical Technologies in the Biomedical and Life Sciences*, 2003, **794**, 35-47.
35. J. D. Henion, *Analytical Chemistry*, 1978, **50**, 1687-1693.
36. H. H. Maurer, *Analytical and Bioanalytical Chemistry*, 2007, **388**, 1315-1325.
37. M. R. Groseclose, S. B. Laffan, K. S. Frazier, A. Hughes-Earle and S. Castellino, *Journal of the American Society for Mass Spectrometry*, 2015, **26**, 887-898.
38. L. Bachmann and M. M. Salpeter, *Journal of Histochemistry & Cytochemistry*, 1966, **14**, 753-&.
39. S. A. M. Cross, A. D. Groves and T. Hesselbo, *International Journal of Applied Radiation and Isotopes*, 1974, **25**, 381-386.

40. E. G. Solon and L. Kraus, *Journal of Pharmacological and Toxicological Methods*, 2001, **46**, 73-81.
41. A. M. Tan, I. A. Levesque, I. M. Levesque, F. Viel, N. Boudreau and A. Levesque, *Journal of Chromatography B-Analytical Technologies in the Biomedical and Life Sciences*, 2011, **879**, 1954-1960.
42. E. Stokvis, H. Rosing and J. H. Beijnen, *Rapid Communications in Mass Spectrometry*, 2005, **19**, 401-407.
43. R. M. Caprioli, T. B. Farmer and J. Gile, *Analytical Chemistry*, 1997, **69**, 4751-4760.
44. F. J. Troendle, C. D. Reddick and R. A. Yost, *Journal of the American Society for Mass Spectrometry*, 1999, **10**, 1315-1321.
45. M. L. Reyzer, Y. S. Hsieh, K. Ng, W. A. Korfmacher and R. M. Caprioli, *Journal of Mass Spectrometry*, 2003, **38**, 1081-1092.
46. S. Khatib-Shahidi, M. Andersson, J. L. Herman, T. A. Gillespie and R. M. Caprioli, *Analytical Chemistry*, 2006, **78**, 6448-6456.
47. A. Roempp, S. Guenther, Z. Takats and B. Spengler, *Analytical and Bioanalytical Chemistry*, 2011, **401**, 65-73.
48. R. A. McClure, C. W. Chumbley, M. L. Reyzer, K. Wilson, R. M. Caprioli, J. C. Gore and W. Pham, *Neuroimage-Clinical*, 2013, **2**, 620-629.
49. A. Zavalin, E. M. Todd, P. D. Rawhouser, J. Yang, J. L. Norris and R. M. Caprioli, *Journal of Mass Spectrometry*, 2012, **47**, 1473-1481.
50. H. R. Aerni, D. S. Cornett and R. M. Caprioli, *Analytical Chemistry*, 2006, **78**, 827-834.
51. D. L. Baluya, T. J. Garrett and R. A. Yost, *Analytical Chemistry*, 2007, **79**, 6862-6867.
52. K. Tang, S. L. Allman, R. B. Jones and C. H. Chen, *Analytical Chemistry*, 1993, **65**, 2164-2166.
53. D. Bungert, E. Heinzle and A. Tholey, *Analytical Biochemistry*, 2004, **326**, 167-175.
54. J. A. Hankin and R. C. Murphy, *Analytical Chemistry*, 2010, **82**, 8476-8484.
55. S. L. Koeniger, N. Talaty, Y. P. Luo, D. Ready, M. Voorbach, T. Seifert, S. Cepa, J. A. Fagerland, J. Bouska, W. Buck, R. W. Johnson and S. Spanton, *Rapid Communications in Mass Spectrometry*, 2011, **25**, 503-510.
56. N. Takai, Y. Tanaka, K. Inazawa and H. Saji, *Rapid Communications in Mass Spectrometry*, 2012, **26**, 1549-1556.
57. M. Lagarrigue, R. Lavigne, E. Tabet, V. Genet, J. Thome, K. Rondel, B. Guevel, L. Multigner, M. Samson and C. Pineau, *Analytical Chemistry*, 2014, **86**, 5775-5783.
58. R. F. Reich, K. Cudzilo, J. A. Levisky and R. A. Yost, *Journal of the American Society for Mass Spectrometry*, 2010, **21**, 564-571.
59. J. Stauber, *Bioanalysis*, 2012, **4**, 2095-2098.
60. B. Prideaux and M. Stoeckli, *Journal of Proteomics*, 2012, **75**, 4999-5013.
61. A. Kubo, M. Kajimura and M. Suematsu, *Mass Spectrom (Tokyo)*, 2012, **1**.
62. S. R. Ellis, A. L. Bruinen and R. M. A. Heeren, *Analytical and Bioanalytical Chemistry*, 2014, **406**, 1275-1289.
63. T. Porta, A. Lesur, E. Varesio and G. Hopfgartner, *Analytical and Bioanalytical Chemistry*, 2015, **407**, 2177-2187.
64. D. A. Pirman, *Bioanalysis*, 2015, **7**, 2649-2656.

CHAPTER II

MULTIPLEXED QUANTITATIVE MATRIX-ASSISTED LASER DESORPTION/IONIZATION TIME-OF-FLIGHT/TIME-OF-FLIGHT MASS SPECTROMETRY OF PHARMACEUTICAL DRUGS

Introduction

Large portions of this section were adapted from B. M. Prentice et al., *Journal of Mass Spectrometry*, Copyright 2015 John Wiley & Sons, Ltd.¹

The rapid development of matrix-assisted laser desorption/ionization (MALDI) imaging mass spectrometry (IMS) technology in recent years has focused on advanced instrumentation, sample preparation, and data acquisition methods to improve the throughput, specificity, and sensitivity of these types of measurements.²⁻¹⁰ The importance of these types of improvements is especially evident in experiments involving biological tissue specimens. As previously described in Chapter I, a thinly sectioned tissue specimen is first mounted onto a target and then coated with a MALDI matrix in a manner which preserves the spatial integrity of the analytes of interest. A raster of the laser across the tissue surface is performed to generate a mass spectrum at each x, y coordinate.¹¹ Ion intensity maps are then constructed as a function of x, y position for any single ion of interest. Therefore, the total number of pixels in an image is a function of both the raster step size and the analyzed area. As this is a quadratic relationship, the number of pixels required to sample a large tissue area¹²⁻¹⁵ and/or a tissue area at high spatial resolution^{3, 16-19} can be quite large (Figure 2.1). For example, a 1 cm² tissue section imaged at 100 μm spatial resolution requires a 10,000 pixel image, whereas the same

area imaged at 10 μm spatial resolution results in a 1,000,000 pixel image. Typical spectral acquisition rates ($\sim 2,000$ to $\sim 7,000$ pixels/hour) can then require many hours or days to analyze these types of samples.

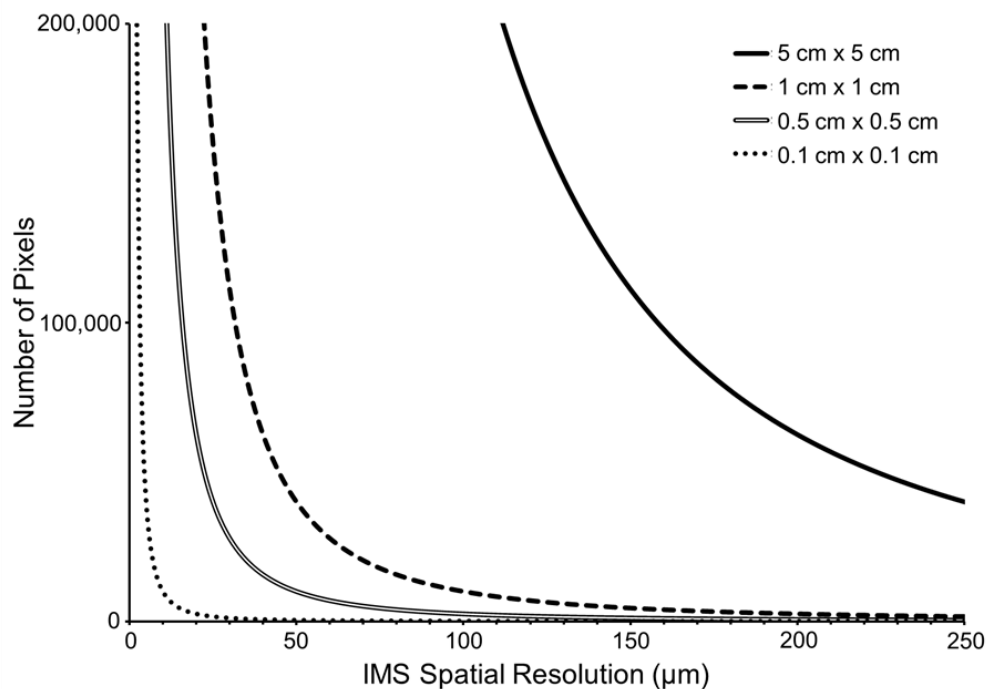


Figure 2.1. Graphical representation of the relationship between the number of pixels and spatial resolution in a MALDI IMS experiment. The number of pixels required to image a specified area is inversely related to the square of the spatial resolution defined across that area.

With the recent advances in laser technology, the analysis time is typically no longer limited by the laser repetition rate;^{18, 20, 21} rather, it is limited by the instrument configuration, the acquisition mode, and the type of mass analyzer. Traditional IMS experiments are performed by moving the sample stage in discrete steps under a stationary laser. At each step, the stage is stopped to fire the laser a set number of times within the defined pixel area before moving to

the next raster step. A second acquisition mode, termed continuous laser raster sampling, has also been described in which the laser is fired continuously as the sample stage is moved at a constant velocity across an area of interest.^{22, 23} A pixel size or the spatial resolution is defined by Equation 2.1. Continuous laser raster sampling has been demonstrated to give 5-fold to 10-fold improvements in throughput and is very well suited to imaging platforms in which the laser acquisition mode is potentially time-limiting. This is the case with time-of-flight (TOF) mass spectrometers.²³

$$R = HA \times \left(\frac{v_{\text{stage}}}{f_{\text{rep}}} \right)$$

Equation 2.1. Lateral spatial resolution (R) is a function of the hardware average (HA) of laser shots per pixel, the laser repetition rate (f_{rep}), and the stage velocity (v_{stage}).

In addition to throughput, specificity is extremely important when analyzing biological tissue specimens. Especially for small metabolites, there exist many isomeric, isobaric, and nearly-isobaric species that contribute to spectral complexity and cloud interpretation. In an imaging experiment, it is especially important to consider these potentially interfering species, since plotting the spatial distribution of a single peak may not represent the spatial distribution of a single ion; instead, an image may represent the confluence of several ions which have overlapping m/z values, giving a distorted picture of the molecular distribution. In instances where a potential lack of specificity is due to nearly-isobaric species, the use of a high mass resolving power instrument platform, such as an orbitrap or Fourier transform ion cyclotron resonance (FTICR) mass spectrometer, may provide enhanced molecular specificity.^{24, 25} In

instances where isomeric and truly isobaric compounds are a concern, ion mobility^{13, 26} and tandem mass spectrometry (MS/MS or MSⁿ)^{13, 27-29} approaches have been successfully employed. In addition to enhancing specificity, these gas phase approaches can improve sensitivity by eliminating chemical noise due to biological contaminants and/or the MALDI matrix. The ability of tandem imaging mass spectrometry approaches to also simultaneously identify the chemical structure of an analyte is particularly attractive. Consequently, imaging MS/MS methods have been successfully employed on several trap-based instrument platforms, including quadrupole-TOF,¹³ linear ion trap, and linear ion trap-orbitrap²⁷⁻²⁹ mass spectrometers. However, trap-based MS/MS methods require lengthier experimental times, decreasing throughput. Tandem in space MS/MS methods in which the ion beam is transmitted through a collision cell without trapping, such as triple quadrupole (QQQ)³⁰ as well as in-source decay TOF³¹ and TOF/TOF³² imaging setups, are inherently faster but have seen far less use in imaging experiments.

MALDI TOF MS has become a popular qualitative analysis tool due to its extensive mass range, rapid analysis time, sensitivity, and minimal sample preparation.³³⁻³⁶ However, the use of MALDI TOF as a quantitative analysis tool has been less widespread.³⁷ Historically, quantitative MALDI approaches have suffered from poor accuracy and precision as well as poor dynamic range, mainly due to sample heterogeneity. Sample heterogeneity issues persist due to variability in MALDI matrix crystallization resulting in a non-uniform distribution of matrix and analyte across the target surface.³⁸ This can cause variations in ion current from laser shots fired at the same sample position (shot-to-shot reproducibility), at different locations on the

target surface (region-to-region reproducibility), and between identical samples on different targets (sample-to-sample reproducibility).

Despite these challenges, MALDI quantitation has been successfully performed in the analysis of many different types of analytes, including polymers,³⁹ drugs,⁴⁰⁻⁴² oligonucleotides,⁴³ oligosaccharides,⁴⁴ peptides,⁴⁵ and proteins.⁴⁶ In these experiments, carefully designed sample preparation is typically extremely important. For example, the uses of a thin matrix layer,⁴⁷ matrix/comatrix approach,⁴⁸ ionic liquid matrix,⁴⁹ electrospray deposition,⁵⁰ acoustic spotting,⁵¹ and matrix seeding⁵²⁻⁵⁴ approaches have all been employed to improve sample homogeneity. In most cases, the use of an internal standard is vital to allow for corrections in sample variability and ionization suppression.^{55, 56} In order to combat region-to-region heterogeneity, many spectra are typically averaged across the target surface to generate a more representative mass spectrum. Preprocessing techniques such as background subtraction and normalization can also help improve quantitative MALDI MS experiments.³⁸ Other quantitative assays have utilized profiling to mitigate the effects of sample heterogeneity.⁵⁷⁻⁵⁹ Despite these advances, accurate quantitation by MALDI MS remains difficult.

The accurate quantitation of small molecules and metabolites with MALDI MS presents an additional challenge.⁶⁰ The analysis of low mass analytes is complicated by the vast excess of MALDI matrix signal and other endogenous sample species that can dominate ion signal in the low m/z region of the mass spectrum. One method to combat this issue is the use of high resolution/accurate mass measurements to distinguish matrix ions from analyte ions on the basis of mass defect. However, these types of measurements typically require more expensive instrument platforms, such as Fourier transform or quadrupole-TOF (Q-TOF) mass

spectrometers. Off-line chromatographic separation and standard addition approaches have been used to simplify the analysis of highly complex samples, but these approaches are still sensitive to matrix effects.⁶¹ Tandem mass spectrometry (MS/MS) can also be used to ensure chemical specificity as well as improve signal to noise ratios by eliminating interferences from chemical noise, alleviating some concerns about dynamic range. MS/MS experiments typically rely on the use isotopically labeled internal standards to perform quantitative analysis.⁶² In these experiments, the quantitative analysis is either performed at the MS⁶¹ or the MS/MS level. The isolation window for MS/MS analyses can be widened sufficiently to pass both the analyte and internal standard ions, or multiple isolation windows can be used to isolate ions of disparate m/z .⁶³ Though an ideal choice because of their speed, TOF/TOF measurements have not been routinely utilized to perform multiple isolation events in a single laser shot and have seen far less use in quantitative MALDI analyses.

A high-speed TOF/TOF imaging platform was utilized to increase the speed of MALDI MS/MS imaging while demonstrating the sensitivity improvements of MS/MS from thin tissue sections. The tissues were dosed *in vitro* and *in vivo* with rifampicin (RIF), an antibiotic used to treat tuberculosis. The instrument, which is capable of isolating and fragmenting multiple precursor ions in a single laser shot, was also used to develop quantitative assays analyzing for multiple pharmaceutical drugs in plasma. The multiplexing capabilities of the instrument allowed for structurally similar drugs, enalapril and ramipril, to be analyzed in the same laser shot, thereby reducing shot-to-shot variability. Finally, three pharmaceutical drugs (enalapril, verapamil, and promethazine) along with isotopically labeled internal standards were analyzed in a single laser shot to develop a quantitative assay.

High-Speed MALDI MS/MS Imaging Mass Spectrometry of Rifampicin

Large portions of this section were adapted from B. M. Prentice et al., *Journal of Mass Spectrometry*, Copyright 2015 John Wiley & Sons, Ltd.¹

Especially for low molecular weight drugs and metabolites, there exist many isomeric, isobaric, and nearly-isobaric species that contribute to spectral complexity. This can be particularly important when examining the biodistribution of a drug.²⁵ On instrument platforms where high resolution MS analysis is not an option, MS/MS is often used to maintain a high level of molecular specificity and ensure accurate results. In instances where large tissue areas are being examined, the high throughput capabilities of a MALDI TOF/TOF platform equipped with continuous laser raster sampling are attractive. This is exemplified by imaging in negative ion mode the distribution of RIF, an antibiotic frequently used in the treatment of tuberculosis, in a rat kidney dosed *in vitro*.

A rat kidney (637 mg) was dosed *in vitro* by immersion with agitation in a solution of RIF (200 μ M) for a total of 100 hours. The kidney was then flash-frozen and stored at -80°C until analysis. The kidney, along with a control kidney, was cryosectioned into 12 μ m thick coronal sections and thaw-mounted onto a gold-coated stainless steel target. Matrix (20 mg/mL 2,4,6-trihydroxyacetophenone [THAP] in 50% ethanol/water) was manually applied using a thin-layer chromatography sprayer.⁶⁴ A serial tissue section was stained with hematoxylin and eosin (H&E) for histological comparisons.

Imaging experiments analyzing for RIF were performed on a continuous laser raster sampling MALDI TOF/TOF mass spectrometer (300 Tandem, SimulTOF Systems, Sudbury, MA).⁶⁵⁻⁶⁷ This instrument is a dual polarity TOF/TOF system with an effective path length of 2.584 m operated

at 8 kV in reflectron MS mode. In MS/MS mode (which is operated at 4 kV), the effective path length of TOF 1 is 78.4 cm to the timed ion selector (TIS) focal plane, the region between the TIS and the TOF 2 two-stage source region is 14.8 cm, the distance between the TOF 2 source region and the two-stage reflectron is 33 cm, and the distance between the reflectron and the detector focal plane is 113.6 cm. This system is equipped with a 349 nm, diode-pumped, frequency-tripled neodymium-doped yttrium lithium fluoride (Nd:YLF) laser (Spectra-Physics, Santa Clara, CA) capable of laser repetition rates up to 5 kHz. The laser beam is oriented at a 90° angle with respect to the target surface, and the laser energy is controlled by adjusting the current applied to the diode. All laser energies reported are measured prior to attenuation, which is kept constant. Ions are extracted from the source region of the instrument via pulsed extraction using grid-less ion optics. The ion beam is then directed through 6 sets of deflector plates to steer the ion beam around the laser optics and place the ion beam trajectory on plane with the detector.

In MS/MS mode, a precision TIS located at the velocity focal distance is used to isolate a precursor ion of interest. Following isolation, the ions enter an 8.6 cm long collision cell and are then reaccelerated to 2 kV in the second source region. Fragmentation can be achieved using either post-source decay (PSD) without a collision gas or high energy collision induced (CID) dissociation using a collision gas. Residual energy from the MALDI process results in PSD, which is fragmentation after the ions have exited the source region of the instrument.⁶⁸⁻⁷¹ In a TOF/TOF configuration, the observed fragments have dissociated after the initial source region but prior to the second source region.^{72, 73} As fragmentation occurs in a field-free region of the instrument, fragments from PSD have the same velocities (but different kinetic energies) as the

intact parent ion, meaning they will arrive at the TIS gate at the same time and will be isolated as a common velocity family. The second source reacceleration then allows for separation of the parent and fragment ions in the second TOF region; this separation of metastable ions has also been historically achieved in TOF configurations using a reflectron.⁶⁸⁻⁷¹ PSD spectra are typically equivalent to more conventional low energy collisional activation processes.^{72, 73} In MS mode, the TIS, collision cell, and second source acceleration regions are not active. Following reacceleration, the ion beam then enters a two-stage ion mirror before reaching the detector (High Mass Bi-Polar TOF detector, Photonis, Sturbridge, MA). A specified number of spectra are hardware averaged on the acquisition card (model U1082A/AP 240, Acqiris USA, Monroe, NY) prior to writing the data to the hard disk. Instrument operation and data acquisition are controlled using the SimulTOF Controller, and data analysis and ion image visualization are performed using the SimulTOF Viewer (SimulTOF Systems, Sudbury, MA). External calibration was performed using matrix clusters of THAP for negative mode calibration.

This instrument is designed to use continuous laser raster sampling. Ion images were acquired at 100 μm spatial resolution in typewriter mode in order to eliminate differences in ion signal intensity dependent on the direction of sample stage motion.²³ The vertical spatial resolution is determined by the motor step size between the continuously rastered rows, and the horizontal spatial resolution is determined via Equation 2.1. Laser repetition rate, stage speed, and number of hardware averages were optimized for the fastest acquisition rate while not exceeding a spectral acquisition speed of 50 pixels/second to maintain a high digitizer efficiency and minimize data loss, not exceeding a laser shot overlap of 50 laser shots per unit

area to ensure severe oversampling does not diminish sensitivity,²³ and not exceeding the maximum current output of the laser.

The singly deprotonated RIF ion, $[M-H]^-$ (m/z 821.4), is observed in MS mode to localize primarily in the cortex of only the dosed kidney (Figure 2.2B). Conversely, a common kidney lipid, SM4s(d18:1/h24:0),⁷⁴ is localized to the medulla region in both the non-dosed control and dosed kidneys (Figure 2.2B) when compared to the stained serial section (Figure 2.2C). The identity of this lipid was confirmed using MS/MS analysis.¹ Using continuous laser raster sampling, the 100 μ m MS image consisted of 48,921 pixels and was acquired in 90 minutes.

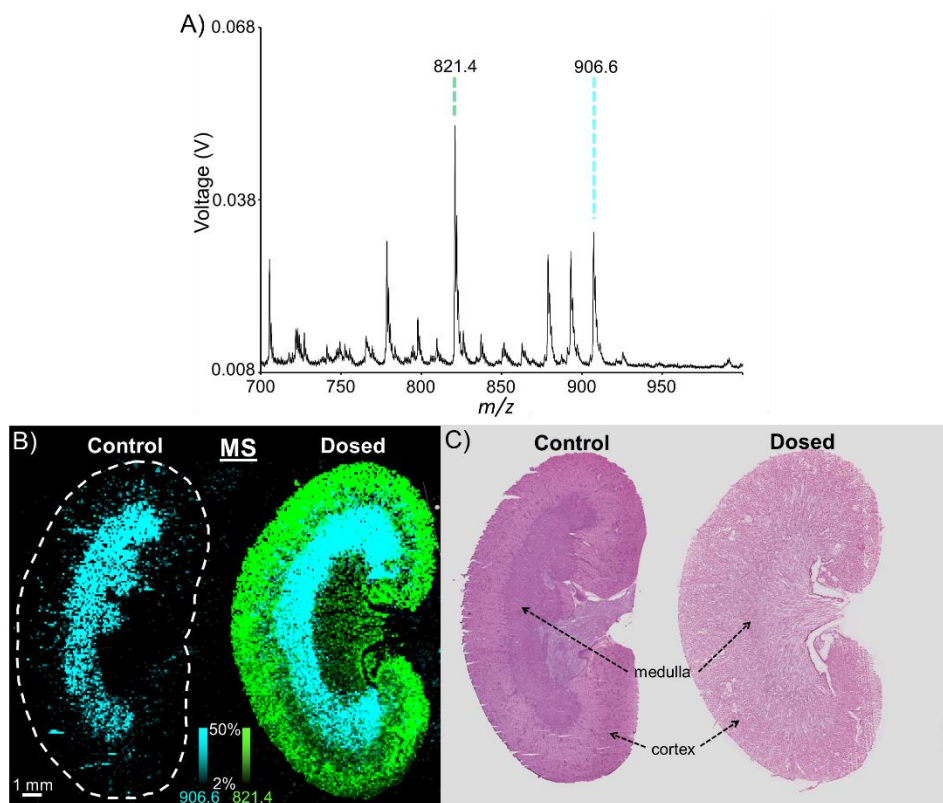


Figure 2.2. Average MALDI IMS full scan spectrum (A) of a kidney dosed *in vitro* with RIF. The full scan MALDI IMS images (B) of a lipid (m/z 906.6) in blue and RIF (m/z 821.4) in green showing localization within the medulla and cortex, respectively, of the kidneys based upon the H&E stained serial sections (C).

As the laser beam diameter is $\sim 50 \mu\text{m}$, a second image can then be acquired, with the continuously rastered rows interleaved within the first image. This is demonstrated on the serial section stained with H&E (Figure 2.3A). Selecting the $[\text{M-H}]^-$ RIF ion to perform a $100 \mu\text{m}$ MS/MS image allows for analysis of the distribution of the primary RIF transition of m/z 821.4 to 397.1, providing molecular confirmation of the drug distribution (Figure 2.3C). This MALDI MS/MS image (Figure 2.3B) contained 46,925 pixels and was acquired in 91 minutes. For both the MS and MS/MS images shown here, the stage velocity was 2 mm/s, the laser frequency was 1,000 Hz, and each pixel represents 50 laser shot hardware averages. Laser pulse energies of $36.0 \mu\text{J}$ and $63.7 \mu\text{J}$ were used for the MS and MS/MS images, respectively. The latter pulse energy is near the maximum pulse energy of the laser at a 1,000 Hz laser frequency, preventing the use of faster laser repetition rates. In this configuration, though the digitizer is acquiring pixels at a rate of 20 Hz, the overall effective acquisition rate is slightly lower. At the end of each line scan, the system is briefly paused to flush the acquired spectra from the acquisition card to the hard disk to minimize data loss. This brief flush period, combined with the delay time required to return the stage to the beginning of the next continuous raster line, resulted in an effective pixel acquisition rate of $\sim 9 \text{ Hz}$ (46,925 pixels/91 minutes).

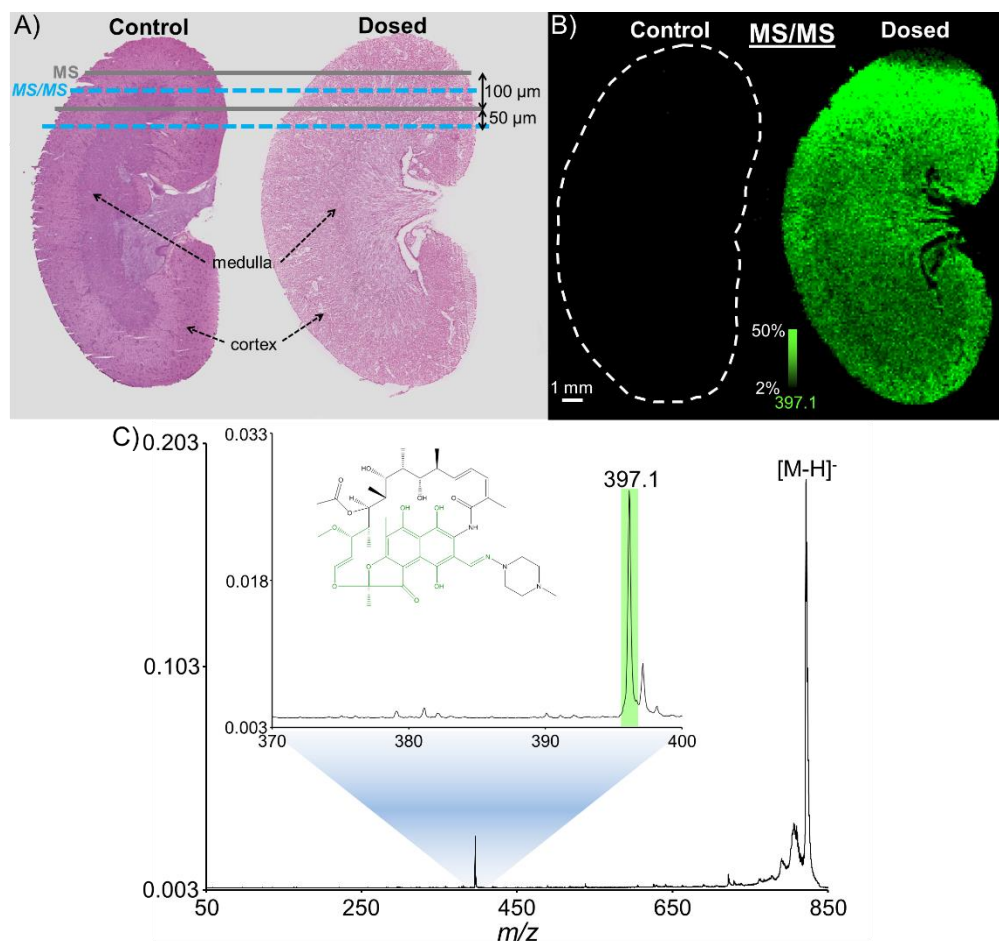


Figure 2.3. Method for analyzing both MALDI MS and MS/MS images of the same tissue section demonstrated on the serial section stained with H&E (A). The MS/MS image (B) of the primary RIF fragment at m/z 397 (C) confirms the localization of RIF in the kidney.

The control kidney and the kidney dosed *in vitro* with RIF were also analyzed on an autoflex TOF/TOF mass spectrometer (Bruker Daltonics, Bremen, Germany) and a linear ion trap mass spectrometer (LTQ XL, Thermo Scientific, San Jose, CA) equipped with a MALDI source for speed comparisons. The autoflex TOF/TOF provides a TOF/TOF platform for comparison which does not utilize continuous laser raster sampling. For the autoflex TOF/TOF experiments, MS/MS images were acquired in LIFT “fragment only” MS/MS mode using no collision gas. The precursor ion for RIF (m/z 821.4 ± 8) was isolated and fragmented. A 150% detector boost, 60%

laser power boost, and 1% (of the parent ion mass) precursor ion selector (PCIS) window were used. A total of 50 laser shots were averaged for each pixel. Data analysis and ion image visualization were performed using flexImaging (Bruker Daltonics, Bremen, Germany). For the ion trap experiments, the precursor ion for RIF (m/z 821.4 \pm 2) was isolated and fragmented using a normalized collision energy of 45%. Three microscans of five laser shots each were analyzed for each pixel. Data analysis and ion image visualization were performed using ImageQuest (Thermo Scientific, San Jose, CA).

Based upon the images acquired using these mass spectrometers, continuous laser raster sampling provides a 10-fold improvement in throughput over an analogous MS/MS image acquired on a TOF/TOF instrument without continuous laser raster scanning (46,226 pixels/861 minutes or an overall effective pixel acquisition speed of \sim 0.9 Hz) and an 8-fold improvement in throughput over an analogous MS/MS image acquired on an ion trap system (48,807 pixels/752 minutes, or an overall effective pixel acquisition speed of \sim 1 Hz). On occasions such as this where an image requires a large number of pixels to effectively sample an area, the use of continuous laser raster sampling, coupled with TOF/TOF analysis, provides an efficient and specific means by which to perform the analysis.

In addition to enhancing specificity and providing molecular confirmation, MALDI MS/MS imaging can also improve sensitivity by eliminating chemical noise due to biological contaminants and/or the MALDI matrix. This is demonstrated by imaging the distribution of RIF in negative ion mode within a rabbit liver dosed *in vivo* (Figure 2.4). Two rabbit liver sections, one dosed with RIF and one control, were cryosectioned into 12 μ m thick sections and prepared for analysis similar to the aforementioned kidneys with THAP. In MS mode, the singly

deprotonated RIF ion, $[M-H]^-$ (m/z 821.4), is not observed in the mass spectrum (Figure 2.4A). An ion image showing the distribution of m/z 821.4 ± 0.4 Da shows no detected RIF as the drug signal is overwhelmed by the chemical background of the tissue (Figure 2.4C). Using continuous laser raster sampling, this 100 μ m MS image consisted of 14,387 pixels and was acquired in 35 minutes. As with the kidney imaging experiment, a second ion image can be acquired by interleaving the acquisition rows within the first image (Figure 2.4D). Selecting the $[M-H]^-$ ion for RIF to perform a 100 μ m MS/MS image allows for the observation of the distribution of the primary RIF fragment (m/z 821.4 to 397.1). RIF is observed to localize to the hepatocytes in the liver, but not in the blood vessels (Figure 2.4E). This is consistent with the steady-state dosing regimen in which RIF would likely be bound to proteins within the blood, but it would be present within the hepatocytes.⁷⁵ The improvement in signal-to-noise afforded by the MS/MS mode image (13,822 pixels acquired in 49 minutes) is due to the elimination of chemical noise and provides an image of the drug distribution. For both the MS and MS/MS images shown here, the stage velocity was 1 mm/s, the laser frequency was 1,000 Hz, and each pixel represents 100 laser shot hardware averages. Laser pulse energies of 36.0 μ J and 63.7 μ J were used for the MS and MS/MS images, respectively.

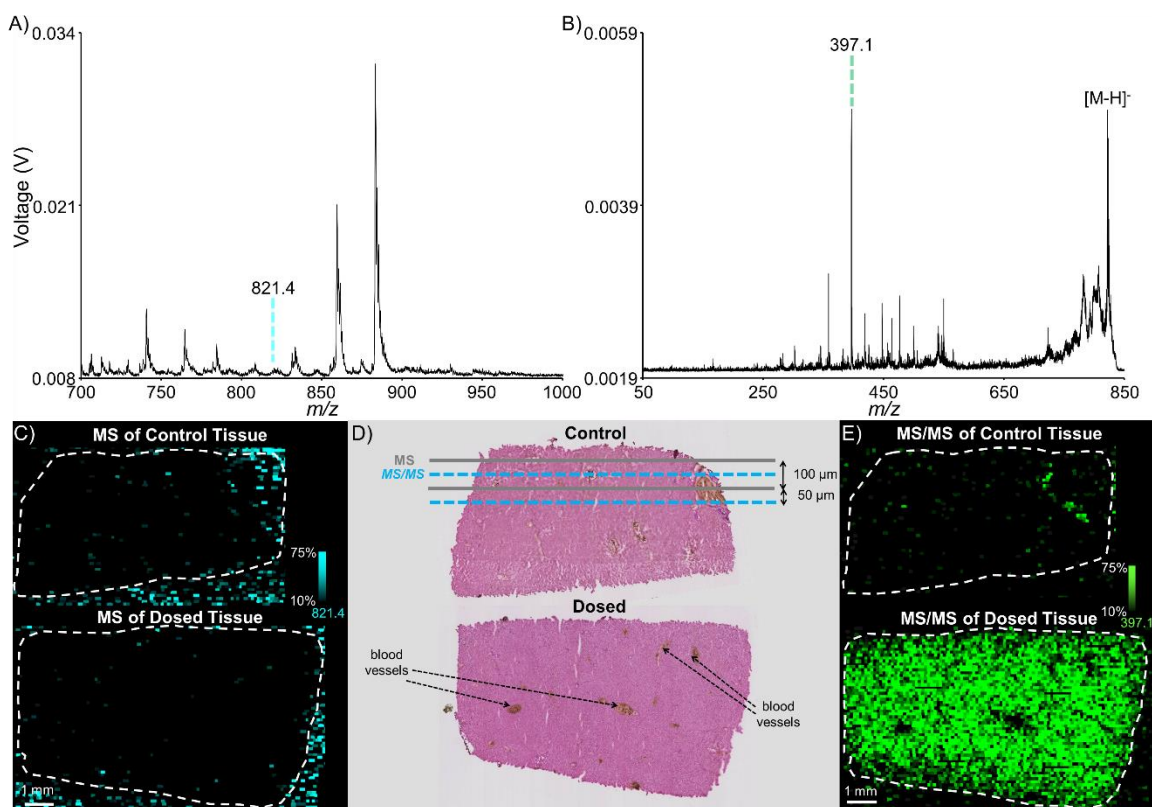


Figure 2.4. MALDI IMS of a tissue section from a liver dosed *in vivo* with RIF. The average spectra for MS analysis of RIF (A) and MS/MS analysis of RIF (B) are an average of 100 pixels in each respective image. The MALDI MS image (C) displays no localization of RIF. The serial sections stained with H&E (D) demonstrate the histology of blood vessels present within the tissues and show the pattern of analysis for the images. Finally, the improvement in signal-to-noise afforded by MS/MS allows RIF to be visualized in the MALDI MS/MS image (E).

The use of continuous laser raster sampling on a MALDI TOF/TOF system improves the throughput ~8-10-fold compared to an ion trap or a non-continuous sampling TOF/TOF system, resulting in overall effective pixel and spectral acquisition rates of up to 10 Hz and 1,000 Hz, respectively. This has been shown to facilitate drug imaging where other isobaric species may complicate spectral and image interpretation, improving the molecular specificity and sensitivity of the resulting MS/MS ion image and dramatically reducing the analysis time. As MALDI IMS analyses are extended to improved spatial resolutions and larger tissue areas,

throughput becomes an important analytical figure of merit. Coupled with the benefits of MS/MS methodology such as improved sensitivity and chemical specificity, continuous laser raster sampling offers a method to maintain high throughput for large imaging datasets.

Multiplexed MS/MS from a Single Laser Shot

The continuous laser raster sampling MALDI TOF/TOF mass spectrometer used in the previous experiments (300 Tandem, SimulTOF Systems) also has the capability of selecting multiple precursor ions in a single laser shot, thereby multiplexing MS/MS analyses. A schematic is shown in Figure 2.5 to explain the process of individually selecting and reaccelerating two distinct precursor ions (the blue and red ions in Figure 2.5) in a single laser shot. Initially, ions are extracted from the first source region of the instrument via pulsed extraction ($t=0 \mu\text{s}$) and then enter the first field-free drift (TOF 1) region of the instrument ($t=15 \mu\text{s}$). In MS/MS mode, a precision TIS (500 FWHM resolution, 6 ns transition speed) located at the velocity focal distance is used to isolate a precursor ion of interest ($t=30 \mu\text{s}$ and $t=38 \mu\text{s}$). The TIS can be 'opened' and 'closed' multiple times within the same laser shot, allowing for the individual isolation of multiple ions of increasing m/z ($t=25 \mu\text{s}$ through $t=45 \mu\text{s}$). Following TIS isolation, the ions enter an 8.6 cm long collision region ($t=30 \mu\text{s}$ and $t=38 \mu\text{s}$) and are then reaccelerated to 2 kV in the second source region ($t=37 \mu\text{s}$ and $t=45 \mu\text{s}$). Similar to TIS isolation, the second source region can be ramped multiple times within the same laser shot to reaccelerate ions from precursor ions of increasing m/z . The ability to individually isolate and reaccelerate ions of similar m/z is limited by ion transit time through the devices as well as the rise and fall times of the relevant power supplies and the length of the voltage pulses. Consequentially, precursor ions must differ by at least $\sim 6\text{-}7\%$ in m/z to be successfully isolated

and reaccelerated in this fashion. Fragmentation can be achieved using either PSD or high energy CID. For experiments herein, PSD was used for fragmentation. Following reacceleration, the ion beam then enters the TOF 2 region of the instrument including passage through a two-stage ion mirror (not shown in Figure 2.5) before reaching the detector.

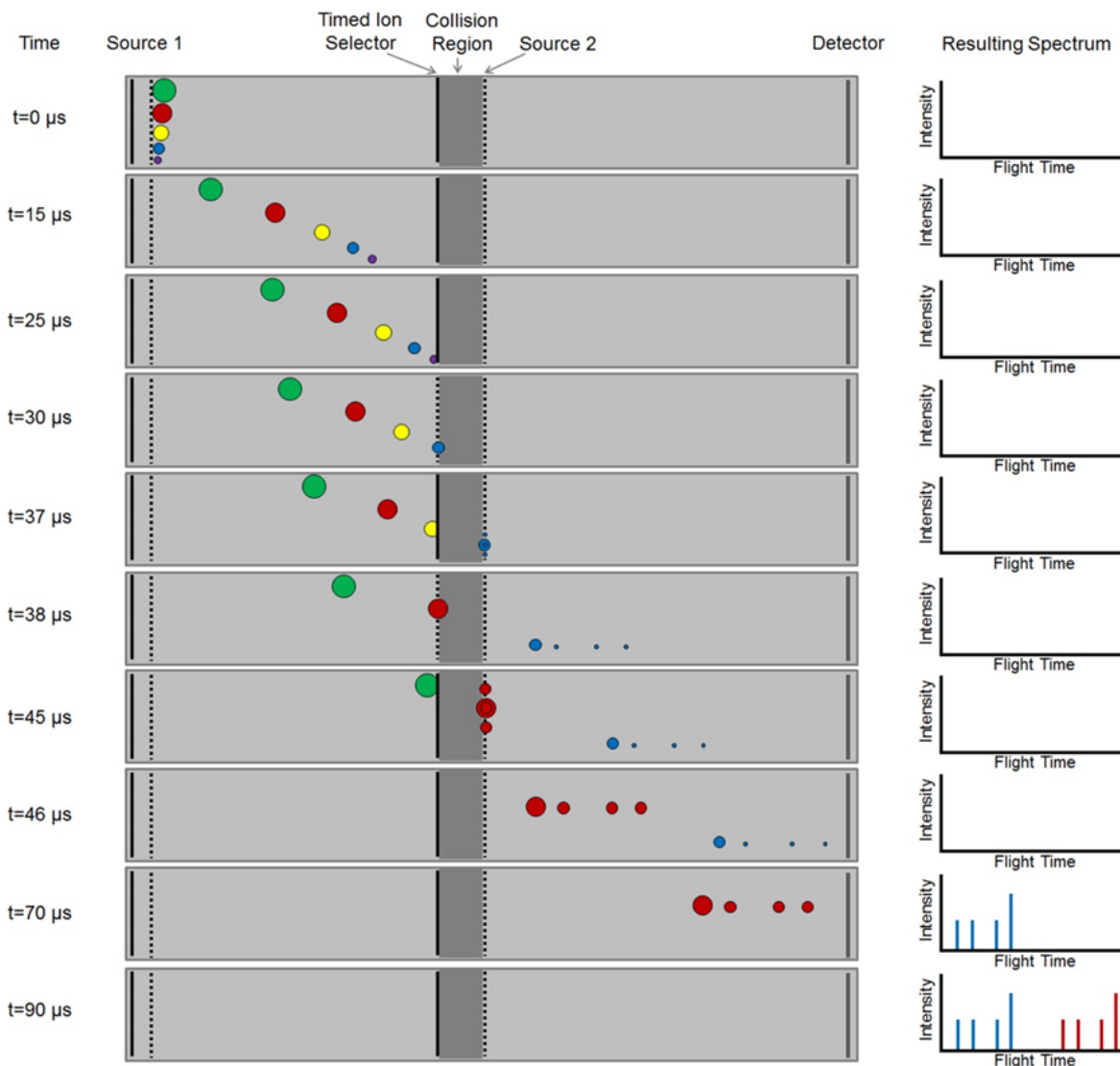


Figure 2.5. Scheme showing the individual selection and reacceleration of two distinct precursor ions in a single laser shot using a MALDI TOF/TOF mass spectrometer. The blue and red ions are isolated and fragmented in the same laser shot. Note: the fragment ions shown arise from CID whereas the actual experiments employ PSD.

The TOF/TOF instrument described here uniquely provides for the individual selection and reacceleration of multiple precursor ions in a single laser shot. An example of such an experiment is shown in Figure 2.6 using two peptides, angiotensin II and [glu1]-fibrinopeptide B (glu-fib). The timing of the isolation and reacceleration of these ions approximately correlates with the timing illustrated in Figure 2.6; the blue ion in Figure 2.6 corresponds to angiotensin II and the red ion corresponds to glu-fib. Initially, the mass spectrum is reported as a function of the ion arrival time at the detector in μs (Figure 2.6A). The mass spectrum can then be calibrated using either angiotensin II as the precursor ion (Figure 2.6B) or glu-fib as the precursor ion (Figure 2.6C). In this simple case, the fragment and precursor ions of the lower mass ion, angiotensin II, all arrive at the detector prior to the arrival of the lowest mass fragment ion of glu-fib; therefore, the two fragment ion spectra do not overlap with one another. Here, assigning fragment ion peaks to their proper precursor ion is relatively easy. Once the proper precursor for a given fragment ion has been identified, the correct mass can be assigned based on the proper mass calibration. As seen in Figures 2.6B and 2.6C, the fragment ions are mainly b- and y-type ions, fragmenting at the amide bonds of the peptides, which are common in the CID analysis of peptides.

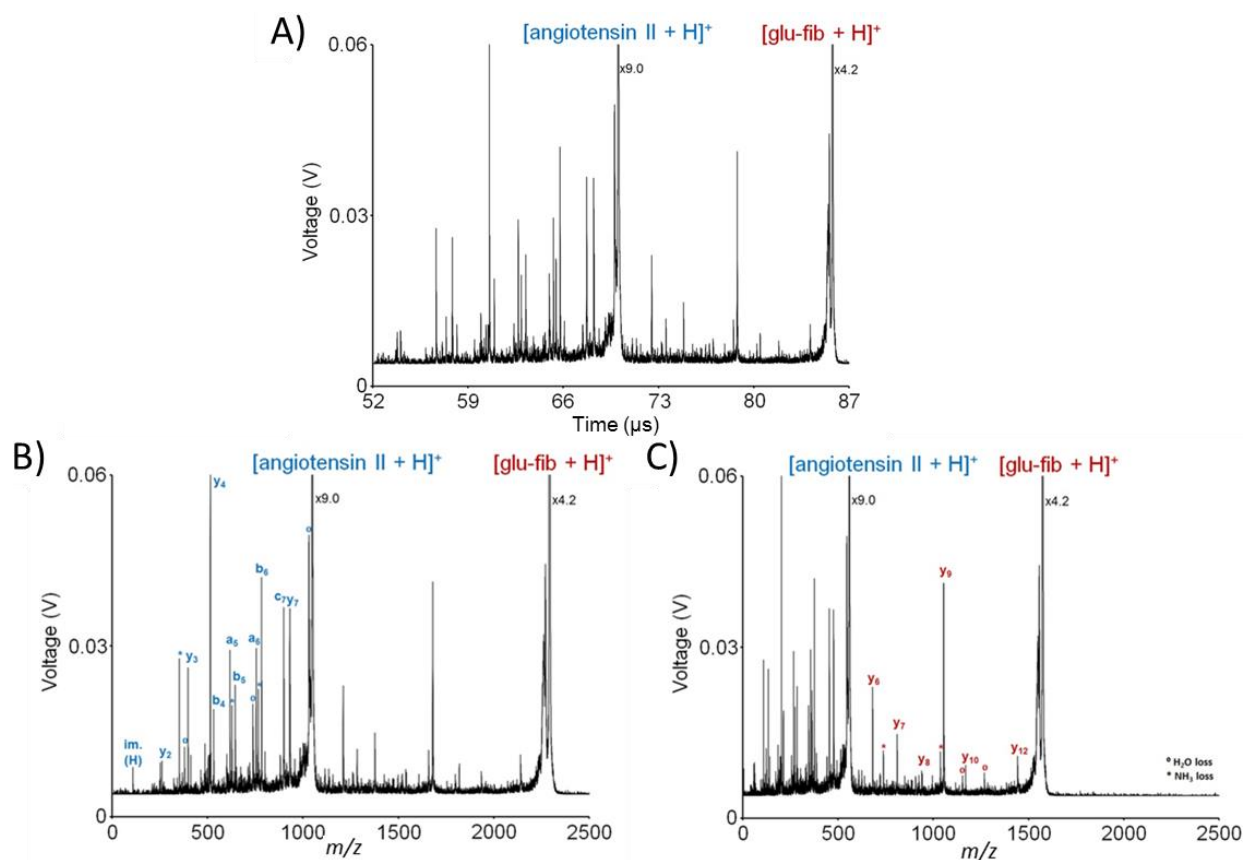


Figure 2.6. Two peptide ions, angiotensin II and glu-fib, are each individually fragmented in a single laser shot (A). Following acquisition, the mass spectrum can then be calibrated using either angiotensin II as the precursor ion (B) or glu-fib as the precursor ion (C). The spectrum represents an average of ~1,000 laser shots.

However, there are more complicated instances where the fragment ion spectra of two precursor ions do overlap. In these cases, prior knowledge of the fragmentation behaviors of the precursor ions of interest is required in order to ensure each fragment ion is accurately assigned to the appropriate precursor ion. An example of this type of experiment is shown using enalapril and ramipril (Figure 2.7), two pharmaceutical drugs used to treat hypertension. In this case, the lowest molecular weight fragment ion (purple, m/z 235) of the higher mass precursor ion (ramipril, m/z 417) arrives at the detector before the lower mass precursor ion

(enalapril, m/z 377) (Figure 2.7C). The enalapril precursor ion appears in the spectrum between the fragment and precursor ions of ramipril. Even with the relatively simple fragmentation patterns of these two drugs, interpretation of the spectrum in Figure 2.7C would be extremely difficult without prior knowledge of the fragmentation patterns. Without knowing which mass calibration to apply for each ion (the calibration using ramipril as the precursor ion or the calibration using enalapril as the precursor ion), it would be challenging to properly assign the fragment ions to the appropriate precursor ion given only the arrival times.

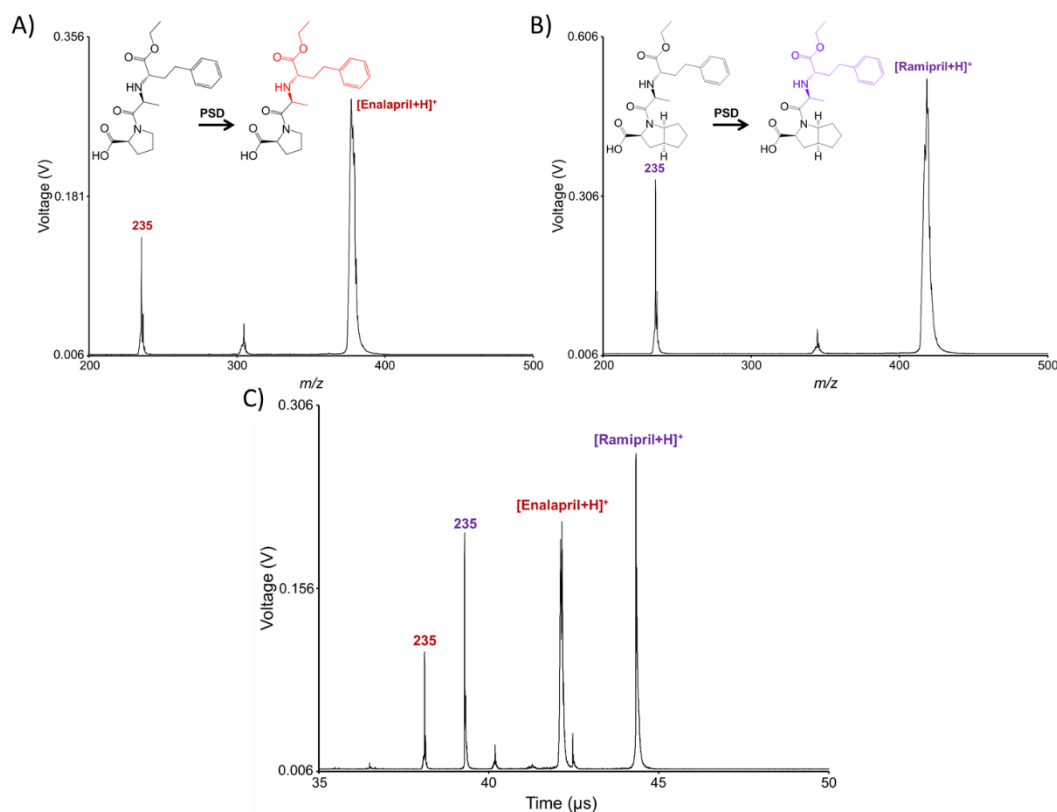


Figure 2.7. Fragmentation of enalapril (A) and ramipril (B) both produce the exact same m/z 235 fragment ion. Using the arrival time information obtained in (A) and (B), fragment ions can be accurately assigned to the proper precursor ion (C). The isomeric m/z 235 fragment ions of the two drugs are separated due to precursor ion separation in the TOF 1 region of the instrument. The colored portions of each structure inset correspond to the detected fragment ion of each species. Each spectrum represents an average of $\sim 1,000$ laser shots.

Because of the additional complexity caused by the fragmentation spectra overlapping, experiments should be conducted fragmenting one ion at a time in order to obtain a product ion spectrum for each precursor ion alone (Figure 2.7A and 2.7B). This fragmentation fingerprint can then be used to accurately assign fragment ions to precursor ions in experiments where multiple ions have been selected for fragmentation. This assignment is performed by comparing the arrival times between the different experiments. As the TIS and reacceleration timings and voltages are kept constant in each experiment, the arrival times of the ions observed in a single precursor experiment will exactly correlate with those observed in a multiple precursor experiment, allowing for proper peak assignment.

Figure 2.7 also highlights a unique aspect of this TOF/TOF methodology in its ability to resolve fragment ions of the exact same m/z that are derived from different precursor ions. Ramipril and enalapril are structural analogues of one another and differ only by a moiety of cyclopentapyrrole versus pyrrolidine, respectively. Not surprisingly, the two drugs fragment extremely similarly under these conditions, and the resulting structures of the dominant fragments do not contain the disparate portion of the molecules (structural insets in Figures 2.7A and 2.7B). As such, the main fragment ions of the two drugs are exact isomers of one another and would be indistinguishable on any high resolution/accurate mass, ion trap MS/MS, or ion mobility instruments in a single measurement. With the TOF/TOF platform, however, the separation in time of the precursor ions in the TOF 1 region of the instrument allows for the facile separation of the isomeric fragment ions. This is similar in principle to a triple quadrupole (QqQ) precursor ion scan, where the separation of precursor ions is performed by scanning of the first resolving quadrupole (Q1) while the third quadrupole (Q3) remains fixed on the

fragment ion of interest. However, in contrast to a triple quadrupole, an entire fragment ion spectrum is obtained for each precursor ion in every laser shot with this setup.

Quantitation of Enalapril in Plasma with Ramipril as the Internal Standard

In characterizing this methodology, we sought to explore the use of multiple TOF/TOF events in a single laser shot for improved quantitation. By using one TOF/TOF event for an analyte and a second TOF/TOF event for an internal standard, the intensity of the analyte can be referenced to that of an internal standard in each laser shot even in instances where the two ions are quite different in m/z , such as the case with enalapril and ramipril. In such instances, simply broadening the isolation window to allow the transmittance of both precursor ions is not practical; the required $m/z \sim 40$ isolation window would transmit an excess of chemical noise which would diminish sensitivity and mitigate the benefits of MS/MS specificity.

As enalapril and ramipril possess similar physical and chemical properties, this drug pair represents an ideal test for MALDI MS/MS quantitation. For these experiments, enalapril was chosen as the analyte and ramipril as the internal standard. Stock solutions of enalapril maleate (20.0 μM) and ramipril (10.0 μM) were made in 50% methanol/water and stored at -80°C. Working calibration solutions of enalapril (0.0300-10.0 μM) with 0.500 μM ramipril as the internal standard were prepared in 45% pooled human plasma containing K2EDTA as an anticoagulant. Quality control (QC) solutions of 5.00 μM and 0.500 μM of enalapril with 0.500 μM ramipril in 45% plasma were also included in the analysis. Following protein precipitation with acetonitrile, the samples were centrifuged, and the supernatants were removed and dried down. The samples were then reconstituted in 15 μL of 50 mg/mL 2,5-dihydroxybenzoic acid (DHB) in 50% methanol/water with 0.1% trifluoroacetic acid prior to manually spotting onto a

gold-coated stainless steel MALDI target. Five sets of enalapril/ramipril spots were prepared and analyzed on the MALDI TOF/TOF platform.

For each replicate analysis, data were acquired in imaging mode using an intensity filter to only record a spectrum when at least 2 peaks reached 0.06 volts in intensity. The TIS was set for a difference of 40 ns (TISB Delay Equation=1880, TISB Pulse End Equation=1920). This results in pulse lengths of ~500 and ~525 ns for the TIS isolation events for enalapril and ramipril, respectively. In practice, this corresponds to isolation windows of m/z ~4-5. The Source 2 Pulse End Slope was set to 1.03, resulting in ~690 and ~725 ns Source 2 pulse lengths for enalapril and ramipril, respectively. Following data acquisition, peak detection settings were optimized to detect both the ^{12}C and ^{13}C isotopes of both the enalapril and ramipril fragment ions (doublet preset, minimum signal-to-noise ratio: 1, max peak width: 3E-8 seconds, deisotope width: 0.0001). Regions of interest were manually selected in the SimulTOF Viewer for each MALDI spot to yield an average spectrum. The SimulTOF Viewer determines peak areas for a selected region of interest by computing a sum of all the individual spectra. A list of masses and corresponding peak areas from each average spectrum was exported to Excel, where the ^{12}C and ^{13}C isotopes of each drug fragment were summed and quantitative calculations performed.

As mentioned previously, quantitative MALDI MS without the use of an internal standard can be quite challenging. The relative standard deviations (RSDs) of enalapril without normalization to the internal standard were well above 20% at every concentration (“Raw Standard Deviation” in Table 2.1). However, upon normalization to ramipril as the internal standard, the RSDs of enalapril at every concentration dropped below 9% (“Ratio Standard Deviation” in

Table 2.1). This resulted in greater than a 4-fold improvement in RSD at most concentrations and provided for a dynamic range of over 2.5 orders of magnitude and a lower limit of quantitation (LLOQ) of 0.0300 μM . This LLOQ of ~ 11 ng/mL is well below the expected serum level following a single dose (275 ng/mL two hours post-dose) and compares favorably with values obtained via HPLC.⁷⁶⁻⁷⁸ In addition to an improvement in precision, improvements in linearity (Figure 2.8) and accuracy (Table 2.2) were also observed upon normalization to ramipril. As determined in the range of 0.0300 to 10.0 μM , a linear regression analysis showed an improvement in the correlation coefficient from 0.9966 to 0.9998 upon normalization (Figure 2.8).

Concentration (μM)	Average Raw (Abundance)	Average Ratio (Enalapril/Ramipril)	Raw Standard Deviation (%)	Ratio Standard Deviation (%)
0	974.94	0.0361	51.0	13.9
0.0300	8,733.56	0.0820	37.6	6.64
0.0700	9,949.36	0.0905	25.2	7.59
0.100	13,258.70	0.167	37.9	8.40
0.300	34,067.25	0.376	35.4	6.10
0.700	30,910.39	0.979	28.0	6.94
1.00	96,651.56	1.24	35.6	7.70
3.00	229,541.16	3.97	25.6	3.51
7.00	580,569.41	8.89	22.6	4.41
10.0	771,085.47	12.9	28.3	1.65
Low QC (0.500)	31,374.80	0.649	54.8	8.38
High QC (5.00)	120,606.44	6.85	67.6	6.10

Table 2.1. Average detected raw abundances of enalapril and abundance ratios of enalapril/ramipril for five different trials. Normalization to ramipril as the internal standard decreased the relative standard deviation of the measurements, thereby improving the precision for enalapril quantitation.

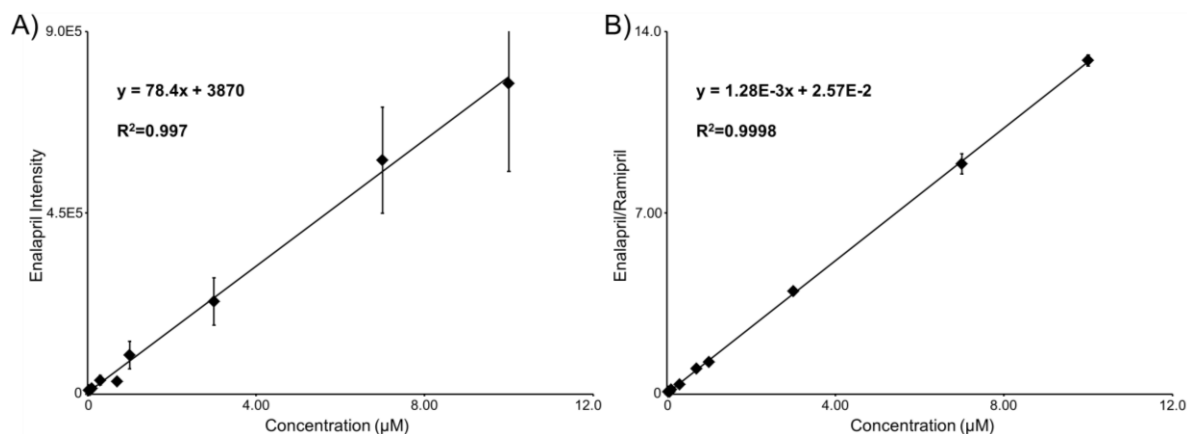


Figure 2.8. Calibration curves of enalapril in plasma before normalization (A) and after normalization to ramipril (B). Linearity is improved after normalization (n=5).

Trial	Quality Control Concentration (µM)	Raw Accuracy (%)	Ratio Accuracy (%)
1	0.500	75.4	89.7
1	5.00	18.7	99.7
2	0.500	50.2	97.2
2	5.00	17.4	88.8
3	0.500	81.9	96.7
3	5.00	48.5	85.4
4	0.500	97.6	94.9
4	5.00	45.9	99.4
5	0.500	28.7	86.0
5	5.00	10.2	93.8
Average	0.500	66.7	92.9
Average	5.00	28.2	93.4

Table 2.2. Quality control results for enalapril (raw) and normalized enalapril (ratio) in plasma. Accuracies are reported as the difference from 100% of the absolute value of the percent error.

Without normalization, the accuracies for the 0.500 and 5.00 µM QCs were 66.7% and 28.2%, respectively, and as poor as 10.2% in one instance (“Raw Accuracy” in Table 2.2).

However, upon normalization these accuracies improved dramatically to 92.9% and 93.4%, with accuracies for every trial greater than 85% and most above 93% (“Ratio Accuracy” in Table 2.2).

While not surprising that normalization to an internal standard improves accuracy, precision, and linearity in quantitation, the use of multiple TOF/TOF events in a single MALDI laser shot represents novel methodology. This example highlights the quantitative capabilities of this technique within clinically relevant therapeutic ranges.⁷⁶⁻⁷⁹

Quantitation Assay for Multiple Drugs in Plasma using Multiplexed MS/MS

Multiplexed MS/MS in a single laser shot can also be leveraged to increase the throughput of a quantitative assay. By using each event to analyze for a different pharmaceutical drug, the analysis can be multiplexed. This is demonstrated here using three drugs: promethazine (PMZ), enalapril (ENP), and verapamil (VPM). PMZ is a phenothiazine used to treat a variety of conditions, including allergy symptoms and nausea. VPM is a phenylalkylamine class L-type calcium channel blocker used to treat hypertension. For these analyses, isotopically labeled drug analogues, ²H₃-promethazine (²H₃-PMZ), ²H₅-enalapril (²H₅-ENP), and ²H₃-verapamil (²H₃-VPM), were used as internal standards.

Working calibration solutions of the drug panel (0.700-30.0 μM) and a QC solution (5.00 μM) containing 5.00 μM of the internal standards were prepared in a complex sample of pooled human plasma. Sample preparation was identical to that described for the enalapril/ramipril experiments described above. Five sets of the drug panel spots were prepared and analyzed on the TOF/TOF platform.

For each replicate analysis, data were acquired in imaging mode using an intensity filter to only record a spectrum when at least 3 peaks reached 0.06 volts in intensity. In order to

accommodate the isotopically labeled internal standards, the TIS isolation windows were broadened. The TIS was set for a difference of 75 (TISB Delay Equation=1870, TISB Pulse End Equation=1945). This results in pulse lengths of ~740, ~845, and ~920 ns for the TIS isolation events for PMZ and $^2\text{H}_3$ -PMZ, ENP and $^2\text{H}_5$ -ENP, and VPM and $^2\text{H}_3$ -VPM, respectively. In practice, this corresponds to isolation windows of $m/z \sim 8$. The Source 2 Pulse End Slope was decreased slightly to 1.022 to ensure the multiple pulses did not overlap. This resulted in Source 2 pulse lengths of ~450, ~510, and ~560 ns for PMZ and $^2\text{H}_3$ -PMZ, ENP and $^2\text{H}_5$ -ENP, and VPM and $^2\text{H}_3$ -VPM, respectively, which were all long enough to fully cover the range of $m/z \sim 8$ isolated by the TIS. Following data acquisition, peak detection settings were optimized to detect both the ^{12}C and ^{13}C isotopes of both the enalapril and ramipril fragment ions (wavelet preset, minimum SNR: 1, max peak width: 0 seconds, deisotope width: 0.0001). Regions of interest were manually selected in the SimulTOF Viewer for each MADLI spot to yield an average spectrum. A list of masses and corresponding peak areas from each average spectrum was exported to Excel, where the ^{12}C and ^{13}C isotopes of each drug fragment were summed and quantitative calculations performed.

The quantitative assay of these three drugs involves three separate TOF/TOF events in a single laser shot (Figure 2.9A), effectively tripling the throughput for this type of assay. Zoomed-in regions of the x-axis show the relevant time (mass) range for each drug transition (Figure 2.9B-D), with the figure insets showing the chemical structures of the three drugs. For PMZ (Figure 2.9B), ENP (Figure 2.9C), and VPM (Figure 2.9D), the isotopically labeled internal standard (denoted with an asterisk) and the analyte precursor and fragment ions are all clearly visible in their respective mass spectrum.

When performing multiple TOF/TOF events in a single laser shot, the complexity of the resulting mass spectrum is greatly increased. Especially in a quantitative assay, it is imperative peaks from one TOF/TOF event do not exactly overlap with peaks from another TOF/TOF event, as this would give inaccurate measures of ion intensity. That is, if two peaks from two different TOF/TOF events were not resolved from one another, the recorded intensity of the peak would not solely represent the contribution of a single m/z , but rather the sum of two ions of varying m/z . For example, the fragment ions of VPM/²H₃-VPM (m/z 304 and 307* in Figure 2.9D) nearly overlap with the precursor ions of ENP/²H₅-ENP (m/z 377 and 382* in Figure 2.9C). While in this instance these ions are all still clearly resolved from one another, this highlights the care that should be taken with this type of multiplexed MS/MS assay. With this assay, standards of each drug were individually spotted and analyzed in order to confirm the accurate assignment of each fragment ion to the proper precursor ion.

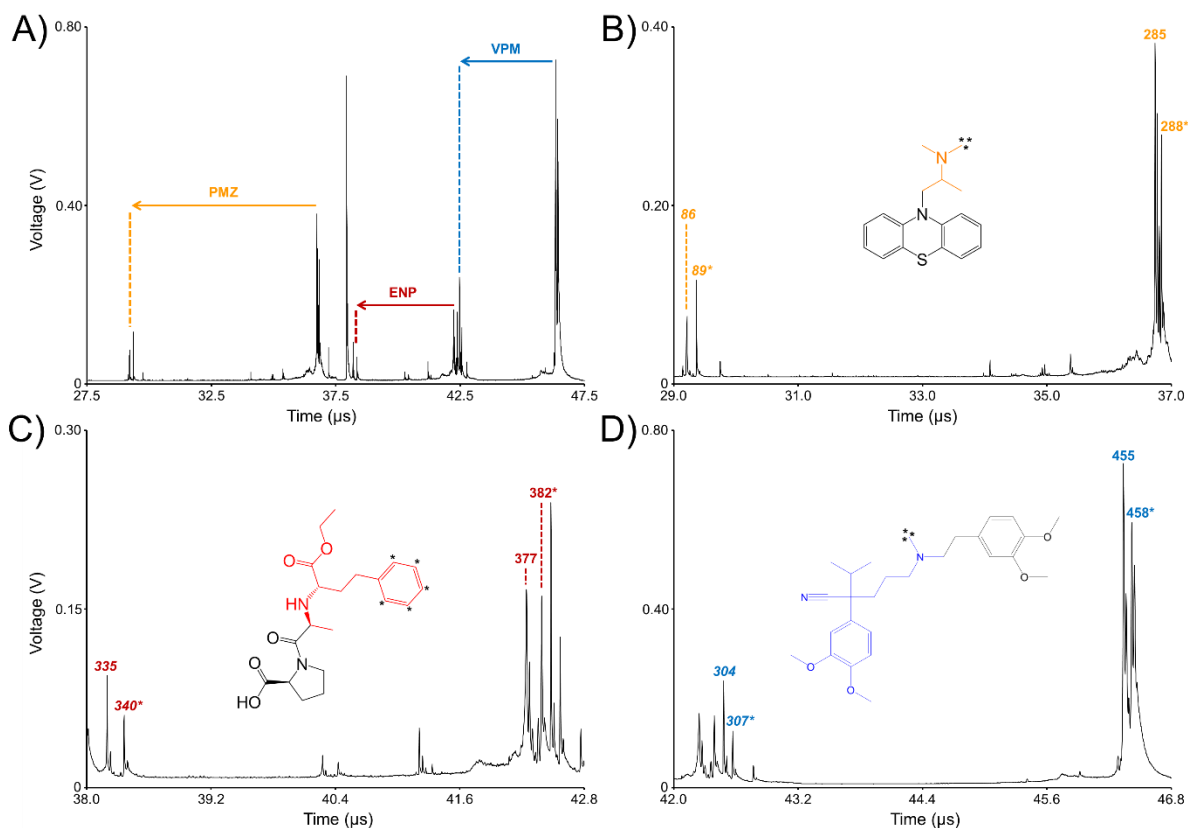


Figure 2.9. Multiplexed MS/MS spectrum (A) of PMZ (yellow), ENP (red), and VPM (blue) spiked into plasma with the deuterated internal standards. Individual spectra display the fragment ions detected from the analyte and the internal standard for PMZ (B), ENP (C), and VPM (D). The structures of the fragments are highlighted in the inset of each spectrum.

Similar to the enalapril/ramipril quantitation experiment described above, normalization of the three drug analytes to their appropriate isotopically labeled internal standard resulted in improved quantitation. The RSDs of PMZ, ENP, and VPM prior to normalization were almost all above 20% at every concentration, with most RSDs above 30% and as high as 52% (“Raw Standard Deviation” in Table 2.3). However, upon normalization to the isotopically labeled internal standards, the RSDs for all three drugs improved dramatically (“Ratio Standard Deviation” in Table 2.3). For PMZ, the standard deviations for the concentration range improved from an average of 27.6% to an average of 7.2% with no RSD higher than 13%. For

ENP, the standard deviations improved from an average of 45.6% to an average of 15.3% with only one RSD higher than 17%. For VPM, the standard deviations for the concentration range improved from an average of 34.9% to an average of 8.3% with no RSD higher than 13%. The reported LLOQ for ENP (0.700 μM) is higher than that reported in Table 2.1, likely due to increased chemical noise transmitted by the additional MS/MS isolation windows.

PMZ Concentration (μM)	Average Raw PMZ (Abundance)	Average Ratio (PMZ/ $^2\text{H}_3$ -PMZ)	Raw Standard Deviation (%)	Ratio Standard Deviation (%)
0.700	61.399	0.129	16.7	3.54
1.00	107.79	0.170	22.2	12.9
3.00	409.13	0.527	36.6	9.57
7.00	747.87	1.12	32.0	6.43
10.0	735.92	1.85	34.8	6.18
30.0	1,214.6	4.87	23.3	4.55
QC (5.00)	481.02	0.734	32.5	8.23
ENP Concentration (μM)	Average Raw ENP (Abundance)	Average Ratio (ENP/ $^2\text{H}_5$ -ENP)	Raw Standard Deviation (%)	Ratio Standard Deviation (%)
0.700	96.472	0.178	42.8	15.1
1.00	128.44	0.218	38.2	16.5
3.00	436.16	0.741	52.5	21.2
7.00	527.00	1.41	52.0	11.1
10.0	720.31	2.60	49.4	16.1
30.0	832.51	4.93	38.6	12.1
QC (5.00)	381.43	0.971	51.9	16.3
VPM Concentration (μM)	Average Raw VPM (Abundance)	Average Ratio (VPM/ $^2\text{H}_3$ -VPM)	Raw Standard Deviation (%)	Ratio Standard Deviation (%)
0.700	118.14	0.166	27.0	12.8
1.00	268.46	0.292	29.3	12.9
3.00	1,028.2	0.902	38.1	7.68
7.00	1,785.8	1.99	44.3	2.59
10.0	1,924.7	3.22	41.4	5.89
30.0	3,349.4	9.14	29.0	8.10
QC (5.00)	1,141.2	1.35	39.7	5.47

Table 2.3. Raw abundances and ratios for each drug demonstrating improvement in precision of the assay when normalizing to their respective isotopically labeled internal standard (n=5).

In addition to improvements in precision, improvements in PMZ, ENP, and VPM accuracy (Table 2.4) and linearity (Figure 2.10) were also observed. Without normalization, the average accuracies for the QCs were 50.2%, 23.5%, and 55.0% for PMZ, ENP, and VPM, respectively (“Raw Accuracy” in Table 2.4). However, upon normalization these accuracies improved dramatically to 84.7%, 84.9%, and 89.5%, respectively, with only one measurement less than 80% (“Ratio Accuracy” in Table 2.4).

PMZ Trial	Quality Control (μM)	Raw Accuracy (%)	Ratio Accuracy (%)
1	5.00	65.6	91.1
2	5.00	51.1	80.0
3	5.00	20.0	81.4
4	5.00	50.8	89.2
5	5.00	63.6	82.0
Average	5.00	50.2	84.7
ENP Trial	Quality Control (μM)	Raw Accuracy (%)	Ratio Accuracy (%)
1	5.00	91.1	88.6
2	5.00	26.5	82.0
3	5.00	48.9	74.8
4	5.00	78.7	93.0
5	5.00	-128	86.3
Average	5.00	23.5	84.9
VPM Trial	Quality Control (μM)	Raw Accuracy (%)	Ratio Accuracy (%)
1	5.00	83.4	91.9
2	5.00	44.7	86.0
3	5.00	43.2	87.0
4	5.00	74.2	91.7
5	5.00	29.5	90.9
Average	5.00	55.0	89.5

Table 2.4. Results from the quality controls for each drug demonstrating improved accuracy of the quantitative assay in plasma when normalizing to their respective internal standard.

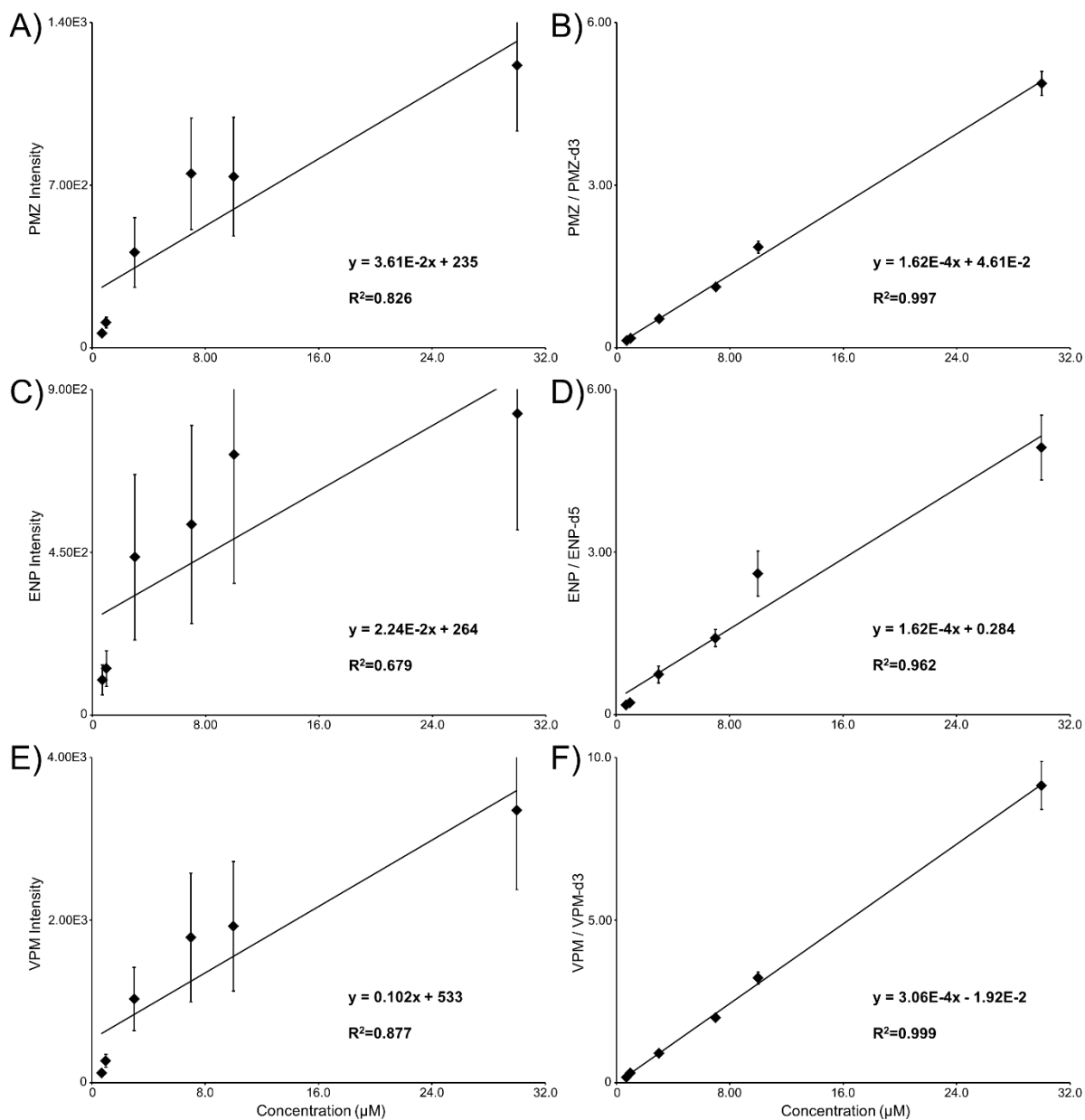


Figure 2.10. Calibration curves for PMZ (A) and normalized PMZ (B), ENP (C) and normalized ENP (D), and VPM (E) and normalized VPM (F). The linearity of the quantitative assay is improved upon normalization.

As determined in the concentration range of 0.700 to 30.0 μM, a linear regression analysis showed dramatic improvements in the correlation coefficients of each drug upon normalization; PMZ improved from 0.8262 to 0.9974 (Figure 2.10A and 2.10B), ENP improved

from 0.6793 to 0.9622 (Figure 2.10C and 2.10D), and VPM improved from 0.8772 to 0.9991 (Figure 2.10E and 2.10F). Each LLOQ is within the lethal dose ranges reported for VPM (500-800 ng/mL) and PMZ (10,000-40,000 ng/mL).⁸⁰⁻⁸⁴ The LLOQ for ENP is at the high end for the therapeutic range (200-700 ng/mL).⁷⁷⁻⁷⁹ A multi-drug assay such as the one presented here could be used to screen samples for toxic levels of the sampled drugs and serves as a proof of principle experiment for the quantitative MALDI TOF/TOF analysis of multiple drugs in a single laser shot.

Conclusions

A high-speed, continuous laser raster sampling MALDI TOF/TOF mass spectrometer was used to improve the throughput of MALDI MS/MS imaging experiments. The use of continuous laser raster sampling on a MALDI TOF/TOF system improves the throughput ~8-10-fold compared to an ion trap or a non-continuous laser raster sampling TOF/TOF system. Furthermore, MS/MS improved the molecular specificity and sensitivity of the resulting MS/MS ion image of RIF in a liver dosed *in vivo*, and continuous laser raster sampling dramatically reduced the analysis time.

The instrument has the capability of not only continuous laser raster sampling, but also isolating and fragmenting multiple precursor ions within the same laser shot, thereby multiplexing MS/MS analyses. Two quantitative assays for pharmaceutical drugs in plasma were developed with this methodology. The first assay analyzed for enalapril with a structural analogue, ramipril, as the internal standard. The precision of the analysis improved nearly 4-fold after normalizing to the internal standard. The linearity and the accuracy also improved upon normalization spanning a range of 2.5 orders of magnitude that included the therapeutic range. Finally, a multiplexed quantitative assay was developed for the analysis of

promethazine, enalapril, and verapamil in a single MALDI MS/MS analysis of human plasma. While the LLOQs for these drugs were higher than the individual enalapril analysis, toxic levels of the drugs fall within the range of this analysis, and these data provide a proof of principle for the quantitative MALDI TOF/TOF analysis of multiple drugs in a single laser shot.

References

1. B. M. Prentice, C. W. Chumbley and R. M. Caprioli, *Journal of Mass Spectrometry*, 2015, **50**, 703-710.
2. P. Chaurand, J. L. Norris, D. S. Cornett, J. A. Mobley and R. M. Caprioli, *Journal of Proteome Research*, 2006, **5**, 2889-2900.
3. A. Zavalin, E. M. Todd, P. D. Rawhouser, J. Yang, J. L. Norris and R. M. Caprioli, *Journal of Mass Spectrometry*, 2012, **47**, 1473-1481.
4. J. L. Norris and R. M. Caprioli, *Proteomics Clinical Applications*, 2013, **7**, 733-738.
5. J. L. Norris and R. M. Caprioli, *Chemical Reviews*, 2013, **113**, 2309-2342.
6. A. Thomas, J. L. Charbonneau, E. Fournaise and P. Chaurand, *Analytical Chemistry*, 2012, **84**, 2048-2054.
7. G. A. Harris, J. J. Nicklay and R. M. Caprioli, *Analytical Chemistry*, 2013, **85**, 2717-2723.
8. E. R. A. van Hove, D. F. Smith and R. M. A. Heeren, *Journal of Chromatography A*, 2010, **1217**, 3946-3954.
9. A. Svatos, *Trends in Biotechnology*, 2010, **28**, 425-434.
10. L. A. McDonnell and R. M. A. Heeren, *Mass Spectrometry Reviews*, 2007, **26**, 606-643.
11. R. M. Caprioli, T. B. Farmer and J. Gile, *Analytical Chemistry*, 1997, **69**, 4751-4760.
12. M. Stoeckli, D. Staab, A. Schweitzer, J. Gardiner and D. Seebach, *Journal of the American Society for Mass Spectrometry*, 2007, **18**, 1921-1924.
13. P. J. Trim, C. M. Henson, J. L. Avery, A. McEwen, M. F. Snel, E. Claude, P. S. Marshall, A. West, A. P. Princivalle and M. R. Clench, *Analytical Chemistry*, 2008, **80**, 8628-8634.
14. E. G. Solon, A. Schweitzer, M. Stoeckli and B. Prideaux, *AAPS Journal*, 2010, **12**, 11-26.
15. M. L. Reyzer, P. Chaurand, P. M. Angel and R. M. Caprioli, *Mass Spectrometry Imaging: Principles and Protocols*, 2010, **656**, 285-301.
16. P. Chaurand, K. E. Schriver and R. M. Caprioli, *Journal of Mass Spectrometry*, 2007, **42**, 476-489.
17. J. H. Jun, Z. Song, Z. Liu, B. J. Nikolau, E. S. Yeung and Y. J. Lee, *Analytical Chemistry*, 2010, **82**, 3255-3265.
18. S. Guenther, M. Koestler, O. Schulz and B. Spengler, *International Journal of Mass Spectrometry*, 2010, **294**, 7-15.
19. G. Thiery-Lavenant, A. I. Zavalin and R. M. Caprioli, *Journal of the American Society for Mass Spectrometry*, 2013, **24**, 609-614.
20. A. Holle, A. Haase, M. Kayser and J. Hoehndorf, *Journal of Mass Spectrometry*, 2006, **41**, 705-716.

21. P. J. Trim, M. Djidja, S. J. Atkinson, K. Oakes, L. M. Cole, D. M. G. Anderson, P. J. Hart, S. Francese and M. R. Clench, *Analytical and Bioanalytical Chemistry*, 2010, **397**, 3409-3419.
22. D. A. Simmons, *Applied Biosystems Technical Note*, 2008, 1-5.
23. J. M. Spraggins and R. M. Caprioli, *Journal of the American Society for Mass Spectrometry*, 2011, **22**, 1022-1031.
24. D. S. Cornett, S. L. Frappier and R. M. Caprioli, *Analytical Chemistry*, 2008, **80**, 5648-5653.
25. S. Castellino, M. R. Groseclose and D. Wagner, *Bioanalysis*, 2011, **3**, 2427-2441.
26. J. A. McLean, W. B. Ridenour and R. M. Caprioli, *Journal of Mass Spectrometry*, 2007, **42**, 1099-1105.
27. R. R. Landgraf, M. C. P. Conaway, T. J. Garrett, P. W. Stacpoole and R. A. Yost, *Analytical Chemistry*, 2009, **81**, 8488-8495.
28. I. Lanekoff, K. Burnum-Johnson, M. Thomas, J. Short, J. P. Carson, J. Cha, S. K. Dey, P. Yang, M. C. P. Conaway and J. Laskin, *Analytical Chemistry*, 2013, **85**, 9596-9603.
29. D. C. Perdian and Y. J. Lee, *Analytical Chemistry*, 2010, **82**, 9393-9400.
30. G. Hopfgartner, E. Varesio and M. Stoeckli, *Rapid Communications in Mass Spectrometry*, 2009, **23**, 733-736.
31. D. Debois, V. Bertrand, L. Quinton, M. De Pauw-Gillet and E. De Pauw, *Analytical Chemistry*, 2010, **82**, 4036-4045.
32. A. Nilsson, T. E. Fehniger, L. Gustavsson, M. Andersson, K. Kenne, G. Marko-Varga and P. E. Andren, *Plos One*, 2010, **5**, e11411.
33. D. N. Nguyen, G. W. Becker and R. M. Riggin, *Journal of Chromatography A*, 1995, **705**, 21-45.
34. E. J. Zaluzec, D. A. Gage and J. T. Watson, *Protein Expression and Purification*, 1995, **6**, 109-123.
35. K. Faulstich, K. Worner, H. Brill and J. W. Engels, *Analytical Chemistry*, 1997, **69**, 4349-4353.
36. P. Roepstorff, *EXS (Basel); Proteomics in functional genomics: Protein structure analysis*, 2000, **88**, 81-97.
37. M. Bucknall, K. Y. C. Fung and M. W. Duncan, *Journal of the American Society for Mass Spectrometry*, 2002, **13**, 1015-1027.
38. M. W. Duncan, H. Roder and S. W. Hunsucker, *Briefings in Functional Genomics & Proteomics*, 2008, **7**, 355-370.
39. K. Tang, S. L. Allman, R. B. Jones and C. H. Chen, *Analytical Chemistry*, 1993, **65**, 2164-2166.
40. D. C. Muddiman, A. I. Gusev, A. Proctor, D. M. Hercules, R. Venkataramanan and W. Diven, *Analytical Chemistry*, 1994, **66**, 2362-2368.
41. D. C. Muddiman, A. I. Gusev, L. B. Martin and D. M. Hercules, *Fresenius Journal of Analytical Chemistry*, 1996, **354**, 103-110.
42. Y. C. Ling, L. N. Lin and Y. T. Chen, *Rapid Communications in Mass Spectrometry*, 1998, **12**, 317-327.
43. B. A. Bruenner, T. T. Yip and T. W. Hutchens, *Rapid Communications in Mass Spectrometry*, 1996, **10**, 1797-1801.

44. T. Kazmaier, S. Roth, J. Zapp, M. Harding and R. Kuhn, *Fresenius Journal of Analytical Chemistry*, 1998, **361**, 473-478.
45. A. I. Gusev, W. R. Wilkinson, A. Proctor and D. M. Hercules, *Fresenius Journal of Analytical Chemistry*, 1996, **354**, 455-463.
46. R. W. Nelson, M. A. McLean and T. W. Hutchens, *Analytical Chemistry*, 1994, **66**, 1408-1415.
47. B. A. Garcia, P. J. Heaney and K. Tang, *Analytical Chemistry*, 2002, **74**, 2083-2091.
48. L. K. Zhang and M. L. Gross, *Journal of the American Society for Mass Spectrometry*, 2000, **11**, 854-865.
49. Y. L. Li and M. L. Gross, *Journal of the American Society for Mass Spectrometry*, 2004, **15**, 1833-1837.
50. R. R. Hensel, R. C. King and K. G. Owens, *Rapid Communications in Mass Spectrometry*, 1997, **11**, 1785-1793.
51. H. R. Aerni, D. S. Cornett and R. M. Caprioli, *Analytical Chemistry*, 2006, **78**, 827-834.
52. F. Xiang and R. C. Beavis, *Rapid Communications in Mass Spectrometry*, 1994, **8**, 199-204.
53. F. M. L. Amado, P. Domingues, M. G. SantanaMarques, A. J. FerrerCorreia and K. B. Tomer, *Rapid Communications in Mass Spectrometry*, 1997, **11**, 1347-1352.
54. P. Onnerfjord, S. Ekstrom, J. Bergquist, J. Nilsson, T. Laurell and G. Marko-Varga, *Rapid Communications in Mass Spectrometry*, 1999, **13**, 315-322.
55. O. A. Mirgorodskaya, Y. P. Kozmin, M. I. Titov, R. Korner, C. P. Sonksen and P. Roepstorff, *Rapid Communications in Mass Spectrometry*, 2000, **14**, 1226-1232.
56. M. W. R. Duncan, Heinrich; Hunsucker, Stephen W., *Briefings in Functional Genomics and Proteomics*, 2008, **7**, 355-370.
57. R. B. Rubin and M. Merchant, *American Biotechnology Laboratory*, 2000, **18**, 20-18, 20.
58. H. H. Zhou, S. Roy, H. Schulman and M. J. Natan, *Trends in Biotechnology*, 2001, **19**, S34-S39.
59. E. F. Petricoin, A. M. Ardekani, B. A. Hitt, P. J. Levine, V. A. Fusaro, S. M. Steinberg, G. B. Mills, C. Simone, D. A. Fishman, E. C. Kohn and L. A. Liotta, *Lancet*, 2002, **359**, 572-577.
60. M. W. Duncan, G. Matanovic and A. Cerpapoljak, *Rapid Communications in Mass Spectrometry*, 1993, **7**, 1090-1094.
61. H. Wei, K. Nolkrantz, M. C. Parkin, C. N. Chisolm, J. P. O'Callaghan and R. T. Kennedy, *Analytical Chemistry*, 2006, **78**, 4342-4351.
62. S. Pan, J. Rush, E. R. Peskind, D. Galasko, K. Chung, J. Quinn, J. Jankovic, J. B. Leverenz, C. Zabetian, C. Pan, Y. Wang, J. H. Oh, J. Gao, J. Zhang, T. Montine and J. Zhang, *Journal of Proteome Research*, 2008, **7**, 720-730.
63. C. W. Chumbley, M. L. Reyzer, J. L. Allen, G. A. Marriner, L. E. Via, C. E. Barry III and R. M. Caprioli, *Analytical Chemistry*, 2016, **88**, 2292-2398.
64. S. A. Schwartz, M. L. Reyzer and R. M. Caprioli, *Journal of Mass Spectrometry*, 2003, **38**, 699-708.
65. M. Vestal and K. Hayden, *International Journal of Mass Spectrometry*, 2007, **268**, 83-92.
66. M. L. Vestal, *Journal of Mass Spectrometry*, 2009, **44**, 303-317.
67. M. L. Vestal, Patent 7,838,824 B2, 2010.

68. X. J. Tang, W. Ens, K. G. Standing and J. B. Westmore, *Analytical Chemistry*, 1988, **60**, 1791-1799.
69. U. Boesl, R. Weinkauff and E. W. Schlag, *International Journal of Mass Spectrometry and Ion Processes*, 1992, **112**, 121-166.
70. R. Kaufmann, D. Kirsch and B. Spengler, *International Journal of Mass Spectrometry and Ion Processes*, 1994, **131**, 355-385.
71. R. Kaufmann, P. Chaurand, D. Kirsch and B. Spengler, *Rapid Communications in Mass Spectrometry*, 1996, **10**, 1199-1208.
72. D. Suckau, A. Resemann, M. Schuereberg, P. Hufnagel, J. Franzen and A. Holle, *Analytical and Bioanalytical Chemistry*, 2003, **376**, 952-965.
73. W. V. Bienvenut, C. Deon, C. Pasquarello, J. M. Campbell, J. C. Sanchez, M. L. Vestal and D. F. Hochstrasser, *Proteomics*, 2002, **2**, 868-876.
74. K. J. Grove, P. A. Voziyan, J. M. Spraggins, S. Wang, P. Paueksakon, R. C. Harris, B. G. Hudson and R. M. Caprioli, *Journal of Lipid Research*, 2014, **55**, 1375-1385.
75. J. Woo, W. Cheung, R. Chan, H. S. Chan, A. Cheng and K. Chan, *Clinical Biochemistry*, 1996, **29**, 175-177.
76. R. J. Macfadyen, P. A. Meredith and H. L. Elliott, *Clinical Pharmacokinetics*, 1993, **25**, 274-282.
77. T. Arafat, R. Awad, M. Hamad, R. Azzam, A. Al-Nasan, A. Jehanli and K. Matalka, *Journal of Clinical Pharmacy and Therapeutics*, 2005, **30**, 319-328.
78. S. Lu, K. Jiang, F. Qin, X. Lu and F. Li, *Journal of Pharmaceutical and Biomedical Analysis*, 2009, **49**, 163-167.
79. J. Biollaz, J. L. Schelling, B. J. D. Combes, D. B. Brunner, G. Desponds, H. R. Brunner, E. H. Ulm, M. Hichens and H. J. Gomez, *British Journal of Clinical Pharmacology*, 1982, **14**, 363-368.
80. H. P. Gelbke, H. J. Schlicht and G. Schmidt, *Archives of Toxicology*, 1977, **37**, 89-94.
81. J. F. Koepke and A. J. McBay, *Journal of Forensic Sciences*, 1987, **32**, 1431-1434.
82. W. J. Allender and A. W. Archer, *Journal of Forensic Sciences*, 1984, **29**, 515-526.
83. D. Macdonald and P. C. Alguire, *American Journal of the Medical Sciences*, 1992, **303**, 115-117.
84. R. Skowronek, R. Celinski, M. Krzystanek, M. Korczynska, J. Kulikowska, J. Nowicka and C. Chowaniec, *European Neuropsychopharmacology*, 2011, **21**, S498-S499.

CHAPTER III

METHOD DEVELOPMENT AND VALIDATION OF QUANTITATIVE MATRIX-ASSISTED LASER DESORPTION/IONIZATION IMAGING MASS SPECTROMETRY OF RIFAMPICIN DIRECTLY FROM TISSUE SECTIONS

Large portions of this chapter were adapted with permission from C. W. Chumbley et al.,
Analytical Chemistry, Copyright 2016 American Chemical Society.¹

Introduction

Since the detection of peptides, proteins, and pharmaceutical drugs directly from tissue sections using matrix-assisted laser desorption/ionization (MALDI) mass spectrometry (MS) was first demonstrated,^{2, 3} MALDI imaging mass spectrometry (IMS) has become an increasingly effective tool used to measure the distribution of compounds within tissue sections. The technology finds a high level of utility in the pharmaceutical industry for the determination of the distributions of potential therapeutic agents and their metabolite(s). The quantitative capability of MALDI IMS from tissue sections has typically been reported through the correlation of the signal response to that from classical analytical techniques, including high-performance liquid chromatography-mass spectrometry (HPLC-MS),⁴⁻⁷ quantitative whole body autoradiography (QWBA),⁷ and gas chromatography with electron capture detection.⁸ Although HPLC-MS has been successful in achieving absolute quantitation, information on the localization of the drug within tissue substructures is lost during the tissue homogenization process required before analysis. While QWBA provides quantitative localization, it requires

synthesis of a radioactive label and produces images of molecules containing the label that do not distinguish the drug from its metabolites.

MALDI IMS provides both spatial and molecular specificity by directly detecting a unique m/z for the compound of interest at specific coordinates in the tissue section. This technology also has the advantage of requiring small amounts of tissue compared to HPLC-MS (12 μm section of ~ 0.5 mg for MALDI IMS vs. ~ 50 mg for HPLC-MS). Absolute quantitation by MALDI IMS has remained challenging because of matrix and tissue heterogeneity, inefficient analyte extraction, and ionization suppression effects. Furthermore, validating pixel-to-pixel quantitative MALDI IMS is difficult, because few other analytical technologies have the ability to quantitatively analyze pharmaceutical drugs in specific regions in an imaging experiment (~ 10 - $1,000$ μm diameter spot on a 3 - 20 μm thick tissue section).

One approach to quantitative MALDI IMS is the creation of surrogate tissue models in which a tissue homogenate dosed with varying concentrations of the analyte is prepared and then compared to an entire tissue section from a tissue dosed *in vivo*.⁹⁻¹¹ This requires preparing a tissue homogenate spiked with different concentrations of the drug for each microenvironment in a tissue. For example, both the medulla and cortex of the kidney or the white and grey matter of the brain would have to be prepared. Others have used a tissue extinction coefficient that must be evaluated for each analyte in every microenvironment of the tissue.¹² A standard addition method in which calibration standards are applied to the dosed tissue section has also been utilized to determine the concentration of small molecules in tissue sections by MALDI IMS.¹³⁻¹⁵ Though data utilizing these published methods correspond well with HPLC-MS results, they remove the spatial advantage of MALDI IMS by reducing the analysis to a bulk quantitative

measurement of the analyte within the entire tissue section, thereby largely ignoring the microenvironments.¹⁶

The utilization of an isotopically labeled internal standard has been reported in MALDI IMS experiments to correct for sample heterogeneity, extraction, and ionization suppression.¹⁷ However, the application and analysis of the internal and calibration standards have also only been validated for the entire tissue section in bulk and not for the microenvironments within a tissue section.¹⁸⁻²¹ Current methods for internal standard application for MALDI IMS reported in the literature include: deposition directly onto the tissue followed sequentially by matrix application,^{13, 22-25} deposition onto the target prior to tissue application,^{14, 15, 26-28} and deposition of the standards pre-mixed with the matrix onto the tissue^{12, 29-33} (Figure 3.1).

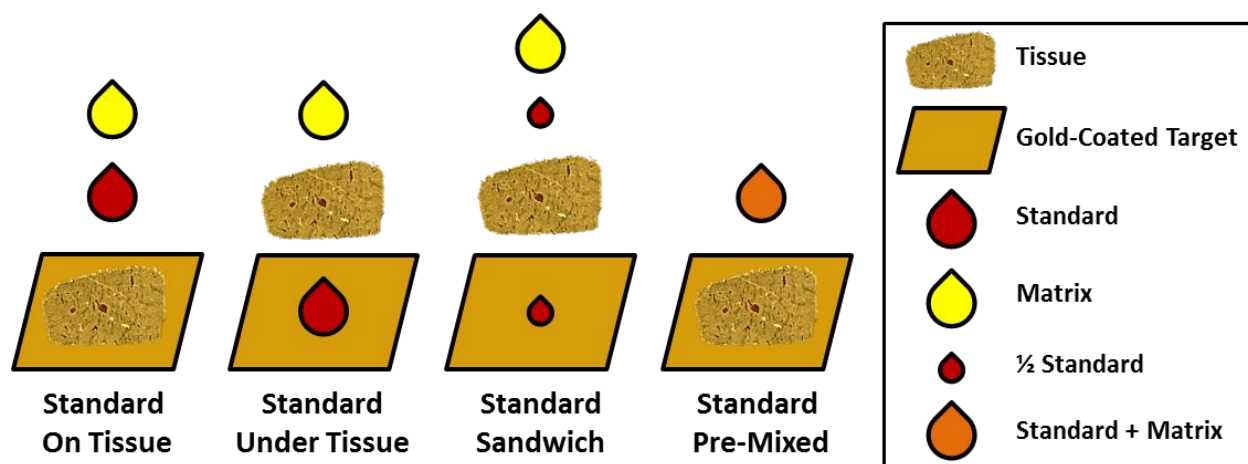


Figure 3.1. Illustration of the four methods of applying internal and calibration standards for MALDI IMS. Depositing the standards on tissue requires thaw-mounting the tissue followed by application of the standards and matrix. Deposition under the tissue requires spotting the standards first, thaw-mounting the tissue on top of them, and then applying matrix. A sandwich method combines depositing the standards under and on the tissue followed by matrix. Pre-mixing the standard involves thaw-mounting the tissue followed by depositing the standards and the matrix in a single solution.

Using these methods of standard application for MALDI IMS, calibration standards are applied to an adjacent, non-dosed tissue section. In order to provide accurate quantitation, the applied standard must mimic the interaction, ionization, and desorption of the analyte in tissue sections of tissues from dosed animals. The internal standard must also be homogeneous throughout the area analyzed. While these methods have demonstrated quantitative imaging capabilities, no validation of the quantitation on the microenvironments within the tissue section has been performed; therefore, they have provided limited spatial information.

A multistep approach was developed to systematically evaluate quantitative MALDI IMS using an isotopically labeled internal standard on the scale of a single microspot. First, a method to homogeneously dose tissues *in vitro* with rifampicin (RIF) was developed in order to evaluate the accuracy and precision of several different methods of microspotted standard application. RIF is a bactericidal and bacteriostatic antibiotic, depending on the concentration, used to treat tuberculosis.³⁴ In addition, another method was evaluated where the standard is applied both before and after thaw-mounting the tissue section onto the target (Figure 3.1). In these experiments, a robotic spotter was used to reproducibly and accurately deposit small volumes of solutions in discrete microspots across a surface.³⁵ These microspots on the tissue sections had a diameter of $203.6 \pm 8.2 \mu\text{m}$ and were used to define the pixels in the subsequent MALDI IMS experiment. Since the calibration microspots and those on the dosed tissue were equal in size, microspots of a quality control (QC) solution were analyzed to ensure the accuracy and precision of the quantitative method for each experiment. This approach was used to apply an array of internal standard and matrix microspots onto a section of liver tissue from a dosed rabbit for quantitative MALDI IMS, thereby demonstrating the localization of RIF

throughout the tissue section in the first quantitative MALDI images validated on the same size scale as the calibration curve. The average of the entire tissue section compared favorably to HPLC-MS/MS results from the bulk tissue homogenate, confirming the accuracy of this approach. This procedure allows for the quantitation of the drug in the microenvironments within the tissue section and for the measurement of local drug concentrations.

Development of a Standard Tissue Homogeneously Dosed *in vitro*

In order to accurately determine the optimal method of internal standard application by comparing the methods with HPLC-MS, a methodology to homogeneously dose tissues *in vitro* was developed. The variations across a tissue section detected by MALDI IMS were mitigated by performing analyses on a homogeneously dosed standard tissue. Therefore, quantitative MALDI IMS measurements of the homogeneous tissue were validated for accuracy and precision with HPLC-tandem mass spectrometry (MS/MS), since the homogenization step required for HPLC-MS/MS necessitates a loss in spatial specificity.

Liver is considered to be a mostly homogeneous tissue composed of hepatocytes.³⁶ Though hepatocytes have differing roles within the liver, the cell types are indistinguishable by pathology. Tissues dosed *in vitro* were prepared by immersing two rat liver pieces (Pel-Freez Biologicals, Rogers, AR) in a solution of RIF (50 μ M in water). After 24 hours of immersion with agitation, the liver pieces were removed from the solution, rinsed with distilled water, flash-frozen, and stored at -80°C until further analysis.

To analyze the homogeneity of the dosing throughout the tissue, a liver dosed *in vitro* was cryosectioned (12 μ m thick) and thaw-mounted onto a gold-coated stainless steel target. Two different 12 μ m thick sections with five 100 μ m thick sections discarded in between them were

thaw-mounted onto the target. Matrix [20 mg/mL 2,4,6-trihydroxyacetophenone (THAP) in 50% ethanol/water] was manually applied using a thin-layer chromatography reagent sprayer (Kontes Glass Company, Vinland, NJ). Serial sections were stained with hematoxylin and eosin (H&E) for histology.

The sections were then analyzed at a spatial resolution of 200 μm using a linear ion trap mass spectrometer equipped with a MALDI source (LTQ XL MS, Thermo Scientific, Waltham, MA). The precursor ion for RIF (m/z 821.4 \pm 0.5) was selected in negative ion mode and fragmented using a normalized collision energy of 45%. The primary MS/MS transition for RIF was m/z 821 to 397 (Figure 3.2C). Images of the fragment ion m/z 397 were generated (ImageQuest, Thermo Scientific) and compared for homogeneity (Figure 3.2A).

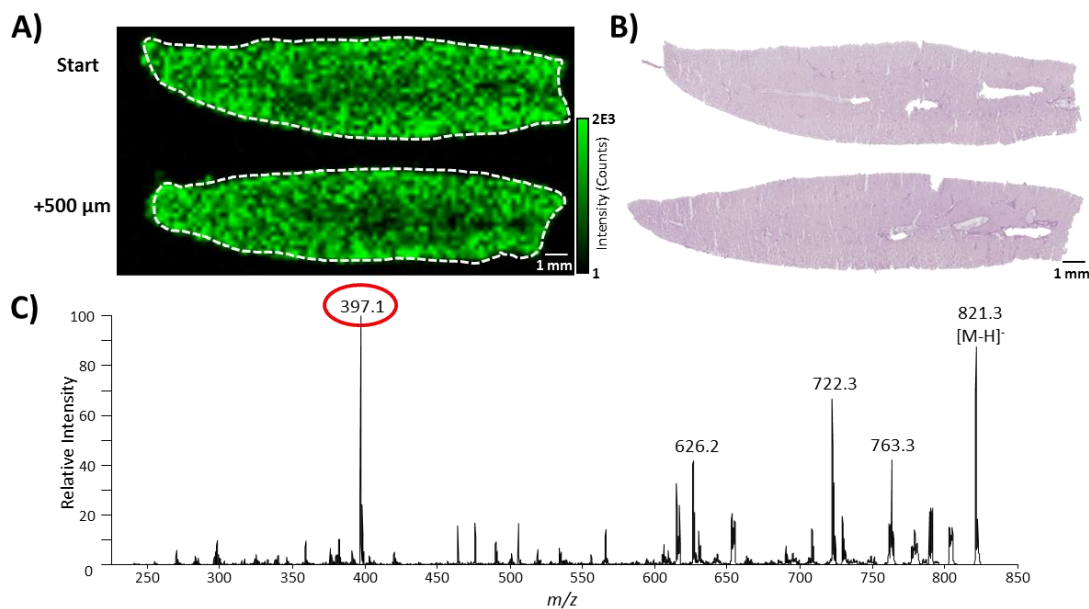


Figure 3.2. The MALDI MS/MS image of RIF (A) analyzed at a spatial resolution of 200 μm with serial sections stained with H&E (B) of two sections of a standard tissue dosed *in vitro* with 500 μm of tissue discarded between them. The image of RIF depicts the homogeneity of the dosing. The average MS/MS spectrum (C) shows the primary fragment ion m/z 397 circled in red.

Imaging experiments of the tissues dosed *in vitro*, collected at a lateral resolution of 200 μm , reveal the homogeneity of the dosing. The ion intensity image of the two 12 μm thick tissue sections with 500 μm of tissue discarded between them is shown in Figure 3.2A with the H&E stained serial sections in Figure 3.2B. An average MS/MS spectrum from the tissue is shown in Figure 3.2C displaying the precursor ion at m/z 821 and the primary fragment ion of RIF at m/z 397. The ion intensity images of m/z 397 are scaled equivalently with a maximum intensity of 2.00E3 counts. The ion intensity localization is consistent between the two sections indicating the tissue was homogeneously dosed. Furthermore, the intensities from 1 mm x 1 mm regions throughout each tissue section covering the entire area were averaged together and were similar. The overall average intensities of these regions for the two sections were 1.25E3 (n=38) and 1.21E3 (n=32) counts, respectively. The relative standard deviations (RSDs) of the measurements from each tissue section were 14.9% and 13.9%, respectively. These data indicate there was not a statistically significant difference between the intensities detected from the two sections of the same liver tissue. Thus, the liver tissues dosed *in vitro* were utilized to test the different methods of calibration and internal standard application for MALDI IMS experiments.

Measuring the Droplet Size of the Acoustic Robotic Spotter

Prior to performing any quantitative MALDI IMS experiments depositing calibration standards using the acoustic robotic spotter (Portrait 630, Labcyte, Sunnyvale, CA), the volume deposited by the instrument was measured. The droplet volume of the robotic spotter was measured using a fluorescence assay to confirm the deposited amount of calibration and internal standards when performing quantitative MALDI IMS. To perform these assays, 50

passes of 100 droplets (5,000 total droplets) of 0.100 mg/mL fluorescein in 50% ethanol/water were deposited into six different wells of a 96-well plate. The droplets were allowed to dry and reconstituted in 100 μ L of 10 μ M tris-buffered saline (pH=9). Calibration standards (100 μ L of 0.100-1.50 μ g/mL) were pipetted into separate wells for comparison. The fluorescence was measured at a wavelength of 514 nm after excitation at 490 nm using a plate reader (SpectraMax M2[®], Molecular Devices, Sunnyvale, CA). The fluorescence responses from the different wells were compared to the manually pipetted calibration curve to determine the droplet size. This experiment was repeated twice, and the average droplet size was determined to be 171.3 ± 10.1 pL/droplet from these measurements.

Determining the Optimal Internal Standard Application Method for MALDI IMS

An isotopically labeled standard for RIF was required before performing any quantitative MALDI IMS experiments using a linear ion trap mass spectrometer. One was not commercially available, but $^{13}\text{C}, ^2\text{H}$ -RIF was synthesized Gwendolyn A. Marriner, a collaborator at the National Institutes of Health, by adapting previously published methods.^{1, 37-40}

The different methods (Figure 3.1) of internal standard application were compared to determine which was the most accurate. The internal standard (10.0 μ M $^{13}\text{C}, ^2\text{H}$ -RIF in 50% ethanol/water) was deposited using the acoustic robotic spotter onto 12 μ m thick serial sections of two different standard tissues dosed *in vitro*. A total of 24 microspots were applied to the liver sections using each method: under, on, sandwich, and pre-mixed (Figure 3.1). The calibration standards (1.00-10.0 μ M RIF with 10.0 μ M $^{13}\text{C}, ^2\text{H}$ -RIF in 50% ethanol/water) were applied using each method to 12 μ m thick sections of a non-dosed liver tissue. A QC solution (5.00 μ M RIF with 10.0 μ M $^{13}\text{C}, ^2\text{H}$ -RIF) was also deposited using each method to ensure

accuracy in the application of the standards. Eight different microspots were averaged for each concentration to construct the calibration curve for each method. A diagram of how the microspots were applied to the sections is displayed in Figure 3.3. Matrix (20 mg/mL THAP in 50% ethanol/water) was applied after the internal and calibration standards for all methods except for pre-mixing. When pre-mixing the standards with the matrix, 20 mg/mL THAP was included in each solution. For the standards and matrix applications, 20 passes of 2 droplets (171.3 ± 10.1 pL/droplet) were deposited using the robotic spotter with 60 seconds between each pass to allow for drying.

A total of 13 analytical scans with 6 microscans of 5 laser shots each was collected using the LTQ XL MS for each spot to average the signal throughout the entire area (200 μ m diameter circle). The precursor ions for RIF and $^{13}\text{C}, ^2\text{H}$ -RIF were selected in a large isolation window (m/z 822.4 ± 1.5) and fragmented using a normalized collision energy of 45%. Spectra for RIF and $^{13}\text{C}, ^2\text{H}$ -RIF with THAP as the matrix and for THAP alone spotted onto a control liver tissue section demonstrate no biological or matrix interferences in the analysis (Figure 3.4). Calibration curves were generated by plotting the average intensity area ratio of the major fragment ion of RIF to the manually corrected (for the isotopic contribution from unlabeled RIF) intensity area of the major fragment ion of $^{13}\text{C}, ^2\text{H}$ -RIF [m/z 397/ m/z 399] versus the concentration of RIF applied to the tissue section (8 microspots for each concentration). The intensity area ratios were generated using MALDIQuan software (Thermo Scientific). The correction for the internal standard intensity is required to account for the contribution of unlabeled RIF (4.16%) to the $[\text{M}-\text{H}+2]^-$ ion from the naturally occurring isotopes of the atoms in the molecule (^{13}C , ^2H , ^{17}O , ^{18}O , and ^{15}N).

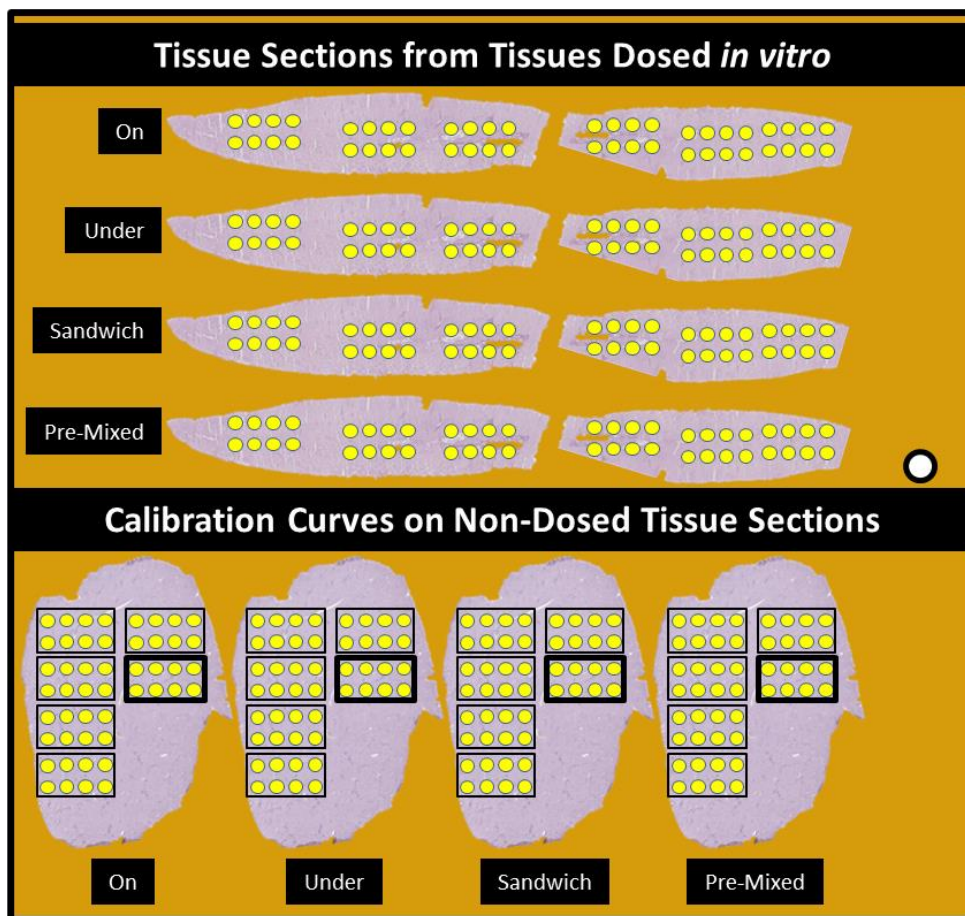


Figure 3.3. Diagram of a MALDI target with the applied microspots for analyzing the different methods of standard application. Eight spots were applied in three different regions of serial sections from the tissue dosed *in vitro* using each of the four methods. Calibration solutions were applied using each of the four methods onto serial sections from a non-dosed liver tissue. Each box represents the eight spots applied for a single concentration of RIF. The bold boxes of spots represent the QC solution spotted using each of the methods.

The total amount of RIF deposited onto the tissue sections is known, since the robotic spotter delivers 171.3 ± 10.1 pL/droplet as previously measured. The density of liver tissue is assumed to be equal to that of water (1.05 g/mL),^{14, 17} and the diameter of the microspots was measured to be 203.6 ± 8.2 μ m ($n=8$) using a microscope (BX-50, Olympus Corporation, Center Valley, PA). A cylinder of tissue (12 μ m tall with a diameter of 200 μ m) was used to calculate

the tissue's mass for each spot to compare to HPLC-MS/MS. Therefore, the amount of tissue for each microspot is 0.396 μg . With these measurements, the amount of RIF detected from each microspot on the dosed tissue sections was calculated by comparing the detected intensity area ratios to those detected from the calibration microspots.

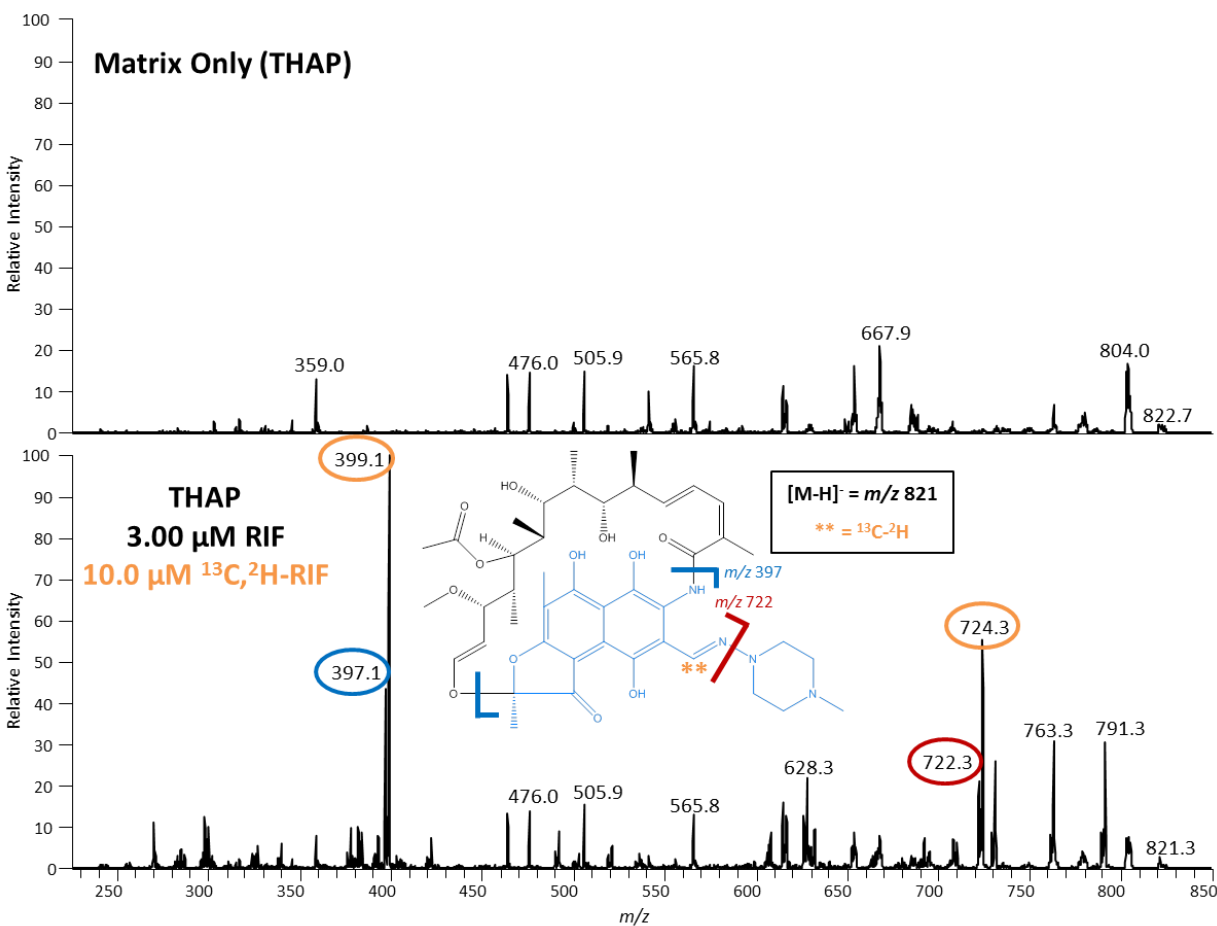


Figure 3.4. Product ion spectra scaled equivalently isolating and fragmenting $m/z 822.4 \pm 1.5$ of the matrix and a calibration standard deposited onto a non-dosed liver tissue section. No interfering background ions were detected from either the tissue or the matrix when the matrix was spotted alone onto the tissue section. The major fragments for RIF are circled in blue ($m/z 397$) and red ($m/z 722$). The corresponding major fragments for $^{13}\text{C}, ^2\text{H}$ -RIF are circled in orange. The likely fragmentation structures are indicated on the structure of RIF with the location of the isotopically labeled ^{13}C and ^2H marked by an orange double asterisk (**).

Variations in analyte sensitivity caused by the method of internal standard application were expected due to the differential extraction of RIF from the tissue section. The addition of an internal standard should compensate for this effect and produce similar calibration curves. The calibration curves for each method of applying the standards generated by plotting the average intensity area ratio of RIF to the corrected $^{13}\text{C}, ^2\text{H}$ -RIF intensity area [m/z 397/ m/z 399 (MALDIQuan Software, Thermo Scientific)] versus the concentration of RIF applied to the tissue section are shown in Figure 3.5A. The error bars in the graph represent the standard deviation of eight microspots for each of the calibration solutions. The 95% confidence intervals for the slopes and y-intercepts overlap, indicating the internal standard accounts for any differences caused by the application method. The accuracies for the QC microspots also averaged greater than 85% for each of the four methods of application. The average concentrations detected using each method for both tissues dosed *in vitro* are shown graphically in Figure 3.5B.

To analyze the livers by HPLC-MS/MS, the dosed liver tissues and a control liver tissue were cut (~80 mg), homogenized in 10% methanol/water (~30 mg/mL), and analyzed similar to a previously published method.⁴¹ Stock solutions of RIF (0.466 mg/mL) and $^{13}\text{C}, ^2\text{H}$ -RIF (0.376 mg/mL) were used to spike calibration standards (2.58E-3 to 5.16E-1 μg RIF with 1.88E-1 μg $^{13}\text{C}, ^2\text{H}$ -RIF) into 150 μL of the control liver homogenate. Only the internal standard was spiked into 150 μL of the dosed tissue homogenates. All samples were diluted with methanol to a final volume of 800 μL and were centrifuged at 10,000 RPM for ten minutes. The supernatants of the tissue homogenates were separated by reversed phase liquid chromatography using a C18 column (30 \times 2 mm, Luna 3 μm , 100 \AA ; Phenomenex, Torrance, CA) and analyzed on a triple quadrupole mass spectrometer (Thermo TSQ Quantum or Agilent 6430). The solvents used for

the HPLC separation were 0.1% formic acid in water (A) and methanol (B). The gradient was as follows: linearly decrease from 90% to 10% solvent A over 5 minutes, hold for 1 minute, linearly increase to 90% solvent A in one minute, and hold for three more minutes. The transitions of m/z 821 to 397 (RIF) and m/z 823 to 399 ($^{13}\text{C},^2\text{H}$ -RIF) were monitored, and the retention times were approximately 5.1 minutes. The dosed tissue homogenates were compared to the spiked calibration standards to determine the amount of RIF present in the dosed tissues (Figure 3.5B).

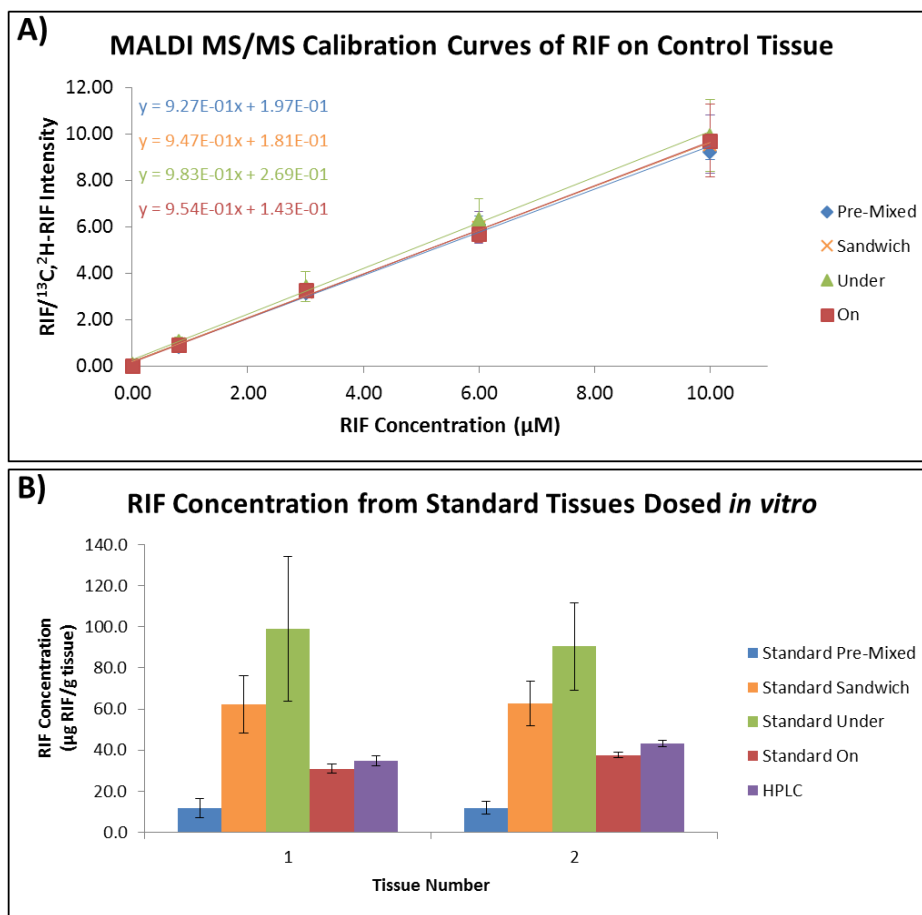


Figure 3.5. A single trial's calibration curves (A) generated using each of the four methods of application with the error bars representing the standard deviation of eight microspots for each calibration solution. A graph (B) displaying the results from the tissues dosed *in vitro* with the error bars representing the standard deviation of at least three trials for MALDI MS/MS and at least five trials for HPLC-MS/MS.

The RIF concentrations (Figure 3.5B and Table 3.1) represent the average of at least three MALDI MS/MS trials and at least five trials for HPLC-MS/MS using the same tissue homogenates with the error bars showing the standard deviations. Pre-mixing the internal standard with the matrix yielded measured concentrations lower than those from HPLC-MS/MS, while depositing the standard prior to thaw-mounting the tissue provided measured concentrations higher than those from HPLC-MS/MS. Comparisons to the HPLC-MS/MS data indicated depositing the standards on the tissue followed by the matrix was the most accurate.

RIF Concentrations of Tissues Dosed <i>in vitro</i> ($\mu\text{g RIF/g Tissue}$)		
	Tissue 1	Tissue 2
Pre-Mixed	11.8 \pm 4.7	11.9 \pm 3.1
Sandwich	62.3 \pm 13.9	62.8 \pm 10.9
Under	99.0 \pm 35.3	90.5 \pm 21.3
On	30.9 \pm 2.2	37.6 \pm 1.5
HPLC-MS/MS	34.6 \pm 2.4	43.1 \pm 1.3

Table 3.1. Average RIF concentrations detected in the tissues dosed *in vitro* using the different internal standard application methods for MALDI MS/MS and HPLC-MS/MS. Depositing the internal standard on the tissue followed sequentially by matrix deposition resulted in values closer to HPLC-MS/MS than the other MALDI MS/MS standard application methods.

An analysis of variance (ANOVA) was performed on the data from both tissues dosed *in vitro* to determine if there were statistical differences among the various methods of MALDI MS/MS quantitation and HPLC-MS/MS quantitation (Tables 3.2 and 3.3 for Tissues 1 and 2, respectively). The computed F statistics were 107 (p-value = 1.20E-58) and 94.3 (p-value =

9.81E-54) for Tissues 1 and 2, respectively, indicating there was a statistical difference among the methods of standard application at the 0.05 significance level.

ANOVA for Methods of Application on Tissue 1					
	Sum of Squares	df	Mean Square	F	p-value
Between Groups	3.52E+11	4	8.79E+10	107	1.20E-58
Within Groups	2.75E+11	335	8.21E+08		
Total	6.27E+11	339			

Table 3.2. Analysis of variance (ANOVA) confirming a statistically significant difference among the different methods for Tissue 1.

ANOVA for Methods of Application on Tissue 2					
	Sum of Squares	df	Mean Square	F	p-value
Between Groups	2.84E+11	4	7.11E+10	94.3	9.81E-54
Within Groups	2.54E+11	337	7.54E+08		
Total	5.38E+11	341			

Table 3.3. Analysis of variance (ANOVA) confirming a statistically significant difference among the different methods for Tissue 2.

A post hoc Tukey test for differences was performed on the results from each tissue (Tables 3.4 and 3.5 for Standard Tissues 1 and 2, respectively) to determine which methods were different from each other. When the test was performed on the data for Standard Tissue 1, there were statistically significant differences from HPLC-MS/MS when the standards were deposited as a sandwich (p-value = 0.033) and under the tissue (p-value = 1.16E-9). When the post hoc analysis was performed for Standard Tissue 2, there were statistically significant differences from HPLC-MS/MS when the standards were pre-mixed with the matrix (p-value = 3.11E-4) and deposited under the tissue (p-value = 1.28E-8). Since depositing the standards onto the tissue section followed by matrix application was not statistically different from HPLC-

MS/MS for either standard tissue, this method was determined to be the best for quantitative MALDI IMS of tissues dosed *in vivo*.

Multiple Comparisons - Tissue 1						
Tukey Test for Differences in ng RIF/g tissue						
(I) Group	(J) Group	Mean Difference (I-J)	Std. Error	p-value	95% Confidence Interval	
					Lower Bound	Upper Bound
Under	On*	6.79E+04	4.84E+03	4.32E-13	5.46E+04	8.12E+04
	Pre-Mixed*	8.71E+04	4.48E+03	4.32E-13	7.49E+04	9.94E+04
	Sandwich*	3.68E+04	4.48E+03	4.78E-13	2.45E+04	4.91E+04
	HPLC*	6.43E+04	9.67E+03	1.16E-09	3.78E+04	9.09E+04
On	Under*	-6.79E+04	4.84E+03	4.32E-13	-8.12E+04	-5.46E+04
	Pre-Mixed*	1.92E+04	4.55E+03	2.98E-04	6.74E+03	3.17E+04
	Sandwich*	-3.11E+04	4.55E+03	3.78E-10	-4.36E+04	-1.86E+04
	HPLC	-3.57E+03	9.70E+03	9.96E-01	-3.02E+04	2.30E+04
Pre-Mixed	Under*	-8.71E+04	4.48E+03	4.32E-13	-9.94E+04	-7.49E+04
	On*	-1.92E+04	4.55E+03	2.98E-04	-3.17E+04	-6.74E+03
	Sandwich*	-5.04E+04	4.16E+03	4.32E-13	-6.18E+04	-3.90E+04
	HPLC	-2.28E+04	9.53E+03	1.20E-01	-4.89E+04	3.33E+03
Sandwich	Under*	-3.68E+04	4.48E+03	4.78E-13	-4.91E+04	-2.45E+04
	On*	3.11E+04	4.55E+03	3.78E-10	1.86E+04	4.36E+04
	Pre-Mixed*	5.04E+04	4.16E+03	4.32E-13	3.90E+04	6.18E+04
	HPLC*	2.76E+04	9.53E+03	3.29E-02	1.43E+03	5.37E+04
HPLC	Under*	-6.43E+04	9.67E+03	1.16E-09	-9.09E+04	-3.78E+04
	On	3.57E+03	9.70E+03	9.96E-01	-2.30E+04	3.02E+04
	Pre-Mixed	2.28E+04	9.53E+03	1.20E-01	-3.33E+03	4.89E+04
	Sandwich*	-2.76E+04	9.53E+03	3.29E-02	-5.37E+04	-1.43E+03

* on the (J) group indicates the mean difference is significant at the 0.05 level.

Table 3.4. Post hoc Tukey test for differences performed for each method on Standard Tissue 1 yielding statistically significant differences from HPLC-MS/MS for MALDI under and MALDI sandwich standard application methods at the 0.05 significance level.

Multiple Comparisons - Tissue 2						
Tukey Test for Differences in ng RIF/g tissue						
(I) Group	(J) Group	Mean Difference (I-J)	Std. Error	p-value	95% Confidence Interval	
					Lower Bound	Upper Bound
Under	On*	5.29E+04	4.61E+03	4.30E-13	4.02E+04	6.55E+04
	Pre-Mixed*	7.86E+04	4.28E+03	4.30E-13	6.69E+04	9.03E+04
	Sandwich*	2.70E+04	4.36E+03	1.85E-08	1.50E+04	3.89E+04
	HPLC*	4.74E+04	7.59E+03	1.28E-08	2.66E+04	6.82E+04
On	Under*	-5.29E+04	4.61E+03	4.30E-13	-6.55E+04	-4.02E+04
	Pre-Mixed*	2.57E+04	4.31E+03	6.12E-08	1.39E+04	3.76E+04
	Sandwich*	-2.59E+04	4.40E+03	9.24E-08	-3.80E+04	-1.38E+04
	HPLC	-5.49E+03	7.61E+03	9.51E-01	-2.64E+04	1.54E+04
Pre-Mixed	Under*	-7.86E+04	4.28E+03	4.30E-13	-9.03E+04	-6.69E+04
	On*	-2.57E+04	4.31E+03	6.12E-08	-3.76E+04	-1.39E+04
	Sandwich*	-5.16E+04	4.05E+03	4.30E-13	-6.28E+04	-4.05E+04
	HPLC*	-3.12E+04	7.41E+03	3.11E-04	-5.16E+04	-1.09E+04
Sandwich	Under*	-2.70E+04	4.36E+03	1.85E-08	-3.89E+04	-1.50E+04
	On*	2.59E+04	4.40E+03	9.24E-08	1.38E+04	3.80E+04
	Pre-Mixed*	5.16E+04	4.05E+03	4.30E-13	4.05E+04	6.28E+04
	HPLC	2.04E+04	7.46E+03	5.09E-02	-4.81E+01	4.09E+04
HPLC	Under*	-4.74E+04	7.59E+03	1.28E-08	-6.82E+04	-2.66E+04
	On	5.49E+03	7.61E+03	9.51E-01	-1.54E+04	2.64E+04
	Pre-Mixed*	3.12E+04	7.41E+03	3.11E-04	1.09E+04	5.16E+04
	Sandwich	-2.04E+04	7.46E+03	5.09E-02	-4.09E+04	4.81E+01

* on the (J) group indicates the mean difference is significant at the 0.05 level.

Table 3.5. Post hoc Tukey test for differences performed for each method on Standard Tissue 2 yielding statistically significant differences from HPLC-MS/MS for MALDI pre-mixed and MALDI under standard application methods at the 0.05 significance level.

The optimal method of applying standards should mimic the response of the analyte from tissues dosed *in vivo*. The methods provided no statistically significant differences in the detected RIF intensities from the dosed tissues (Figure 3.6A), indicating the amount of RIF extracted from the tissues using each method was similar. However, there were differences in the detected intensities for the internal standard depending upon the method of application (Figure 3.6B).

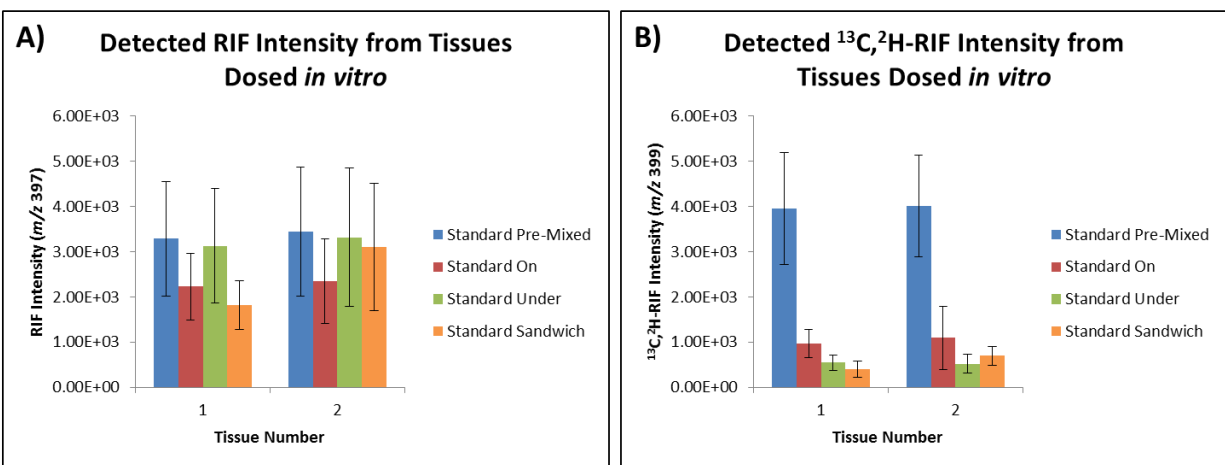


Figure 3.6. Average detected intensities for RIF (A) and ¹³C,²H-RIF (B) from sections of the two tissues dosed *in vitro*. There were no statistically significant differences in the detected RIF intensities when employing the different standard application methods. However, the detected internal standard intensities demonstrated a trend. Pre-mixing the internal standard detected a larger intensity for the internal standard than the other three methods. The other three methods yielded intensities more similar to each other with depositing the internal standard on the tissue having slightly higher average intensities detected from both tissues than others.

Pre-mixing the internal standard with the matrix allows them to co-crystallize with one another prior to reaching the tissue, leading to a larger detected intensity for ¹³C,²H-RIF. A previous study also concluded pre-mixing the standard with the matrix did not suffice as an internal standard for quantitative measurements of analytes in tissue sections.²⁷ Depositing the standards under the tissue provided the highest amount of variability in the concentrations measured from the dosed tissues. Additionally, the internal standard response was the lowest for depositing it before tissue application and for depositing it as a sandwich when compared to the other methods. This is likely caused by the incomplete penetration of the internal standard through the tissue section when it is thaw-mounted yielding less extraction into the matrix for analysis. Because the robotic spotter deposits multiple droplets onto the tissue section, this provides better penetration and mixing of the internal standard into the thin tissue section as if

it were dosed *in vivo*. Based upon these data, depositing standards on the section followed by the matrix using the robotic spotter best mimics the analyte dosed *in vivo* and yields the most accurate concentrations for quantitative MALDI IMS.

Quantitative MALDI IMS of Liver Tissue Sections Dosed *in vivo*

Once the method of internal standard application was validated on a 200 μm microspot size scale, it was applied to tissue sections from a liver dosed *in vivo* to determine the quantitative distribution of RIF. The optimal method for applying the internal standard and calibration standards was determined to be the deposition of the standard and the matrix sequentially onto the tissue sections (Figure 3.5). All *in vivo* animal studies were conducted at the National Institutes of Health laboratories under guidelines of the institutional animal care and use committee of the National Institute of Allergy and Infectious Disease (PHS Assurance #A4149-01). A New Zealand white rabbit infected with *Mycobacterium tuberculosis* was orally administered a cocktail of rifampicin, isoniazid, pyrazinamide, and moxifloxacin (30/50/125/25 mg/kg) once daily for one week and was sacrificed 4 hours and 21 minutes after the final dose according to previously published methods.⁴² The liver tissue was flash-frozen, gamma-irradiated to sterilize the infection, and stored at -80°C until analysis.

The internal standard (10.0 μM $^{13}\text{C},^{2}\text{H}$ -RIF in 50% ethanol/water) was deposited onto a 12 μm section of the dosed tissue in a microspotted array with a spatial resolution of 350 μm using the robotic spotter. Calibration standards (1.00-10.0 μM RIF with 10.0 μM $^{13}\text{C},^{2}\text{H}$ -RIF in 50% ethanol/water including a QC solution of 5.00 μM RIF) were deposited onto a non-dosed tissue section followed by matrix (20 mg/mL THAP in 50% ethanol/water) deposition. This allows for the calibration microspots (including the QC) and the analyzed microspots on the dosed tissue

section to be equal in size and analyzed equivalently. The QC solution was used to determine the accuracy and precision of the method. A total of eight microspots were deposited for each concentration on the calibration curve. Each individual microspot was analyzed on an LTQ XL MS as previously described, and the quantitative MALDI MS/MS image was generated with in-house software developed using MATLAB.

The metabolic mechanisms of RIF in rabbit liver are not fully understood. The primary metabolic pathway is the deacetylation of the acetate at the C-25 position, but the esterase enzyme responsible for this action *in vivo* remains unknown.⁴³ The microspotted quantitative MALDI MS/MS image of RIF in the liver section (Figure 3.7A) shows a gradient of RIF concentration from the middle of the tissue section toward the bottom right. The concentration of the drug around the portal tracts is lower, which is consistent with the metabolic heterogeneity of hepatocytes throughout a liver tissue and is indicative of the microphysiology and zonation of the cytochrome P450 enzymes.⁴⁴⁻⁴⁷ Furthermore, less RIF was detected in the blood vessels, which are outlined in a black dotted line in the quantitative MALDI image (Figure 3.7A) and the microscope scan of the H&E stained serial section (Figure 3.7B), likely because the drug is bound to a blood protein such as albumin or α -1-acid glycoprotein as demonstrated previously where 70-80% of RIF was bound to each of these individually *in vitro*.⁴⁸

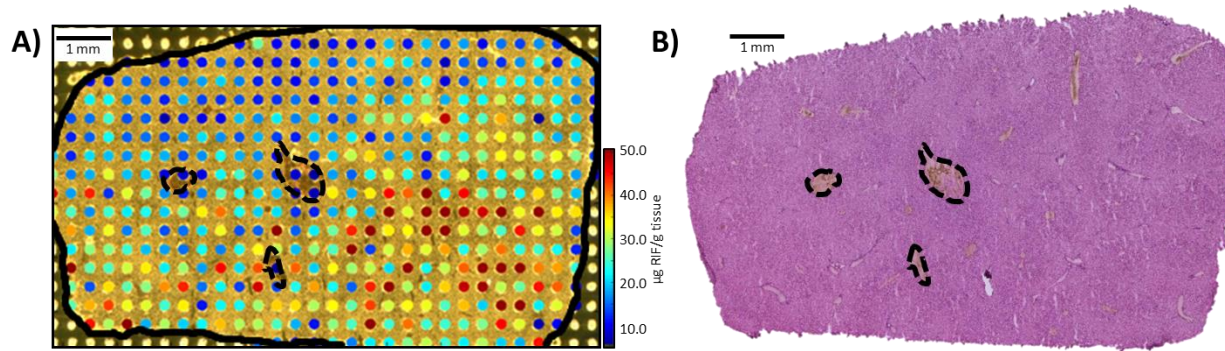


Figure 3.7. Quantitative MALDI MS/MS image of RIF (A) at a spatial resolution of 350 μm showing little RIF detected in the blood vessels outlined with a black dotted line. A gradient of RIF was also detected around the portal tracts revealing the microphysiology of the drug in the liver. A serial section was stained with hematoxylin and eosin (B) for histological comparisons.

Each microspot in the quantitative MALDI MS/MS image represents the amount of RIF in μg RIF/g tissue detected from the tissue section. No RIF was detected in the microspots surrounding the tissue section, and these were not included in the average concentration for MALDI IMS. Each microspot of the QC solution deposited onto the non-dosed tissue section for each trial was greater than 90% accurate with most greater than 95%. The RSDs for the eight microspots of quality control were less than 10% for each of the four trials as well (Table 3.6). Another experiment analyzing eight replicates of calibration standards (50.0-100,000 nM RIF with 10,000 nM $^2\text{H},^{13}\text{C}$ -RIF) was performed to determine the lower and upper limits of quantitation for these measurements. These limits are defined by the United States Food and Drug Administration as the lowest and highest concentrations with less than 20% precision around the mean.^{49, 50} The lowest and highest concentrations of RIF with RSDs less than 20% were 200 nM RIF (11.9%) and 20,000 nM RIF (9.83%), respectively. Therefore, the quantitation range for these measurements spanned two orders of magnitude.

Trial 1			
Concentration (μM)	Average Intensity Ratio	Standard Deviation	RSD (%)
0.00	0.01	0.00	18.5
1.00	0.17	0.03	18.2
3.00	0.46	0.02	3.46
6.00	0.94	0.05	5.48
7.50	1.10	0.10	8.79
10.0	1.54	0.05	2.95
5.00 QC	0.76	0.02	3.14
QC % Error	2.66		
Trial 2			
Concentration (μM)	Average Intensity Ratio	Standard Deviation	RSD (%)
0.00	0.01	0.00	26.5
1.00	0.16	0.01	3.50
3.00	0.47	0.01	3.09
6.00	0.92	0.02	1.87
7.50	1.15	0.04	3.37
10.0	1.50	0.03	1.89
5.00 QC	0.77	0.02	3.03
QC % Error	2.51		
Trial 3			
Concentration (μM)	Average Intensity Ratio	Standard Deviation	RSD (%)
0.00	0.01	0.00	23.4
1.00	0.18	0.01	6.62
3.00	0.53	0.03	5.41
6.00	1.03	0.06	5.46
7.50	1.26	0.09	7.23
10.0	1.70	0.09	5.24
5.00 QC	0.84	0.04	4.40
QC % Error	3.89		
Trial 4			
Concentration (μM)	Average Intensity Ratio	Standard Deviation	RSD (%)
0.00	0.01	0.00	42.2
1.00	0.16	0.01	9.31
3.00	0.51	0.04	7.63
6.00	0.97	0.07	7.63
7.50	1.19	0.06	5.22
10.0	1.57	0.09	5.62
5.00 QC	0.79	0.07	8.84
QC % Error	6.50		

Table 3.6. Relative standard deviations for each calibration standard and the quality control errors for each of four trials of quantitative MALDI IMS of the liver tissue sections from the tissue dosed *in vivo*. The relative standard deviations for all concentrations were less than 20% for all trials with the quality control samples averaging greater than 93% accurate.

An extract of the tissue dosed *in vivo* was also analyzed by HPLC-MS/MS using the homogenization and preparation procedures described previously for those dosed *in vitro*.

When the amounts of RIF detected from each of the microspots in the image shown in Figure 3.7A were averaged together and compared to results from a tissue homogenate extract of the same liver analyzed by HPLC-MS/MS, the results were 90.4% similar (four trials for each analytical technology). The amount detected by quantitative MALDI IMS was $22.9 \pm 2.6 \mu\text{g}$ RIF/g tissue, and the amount detected by HPLC-MS/MS was $25.4 \pm 4.9 \mu\text{g}$ RIF/g tissue (Table 3.7).

Liver Tissue Concentration (μg RIF/g Tissue)	
HPLC-MS/MS	MALDI IMS
25.4 ± 4.9	22.9 ± 2.6

Table 3.7. RIF concentrations detected using HPLC-MS/MS and MALDI IMS from the mouse liver tissue dosed *in vivo*. The similarity between the two values was 90.4%.

No statistically significant difference was found between these two sets of data. Though the overall localization of the drug differed among four different tissue sections from the same tissue (Figure 3.8), the localization within the microenvironments of each section remained the same, and the total RIF concentration measured from each section was consistent with a relative standard deviation of 11.4%.

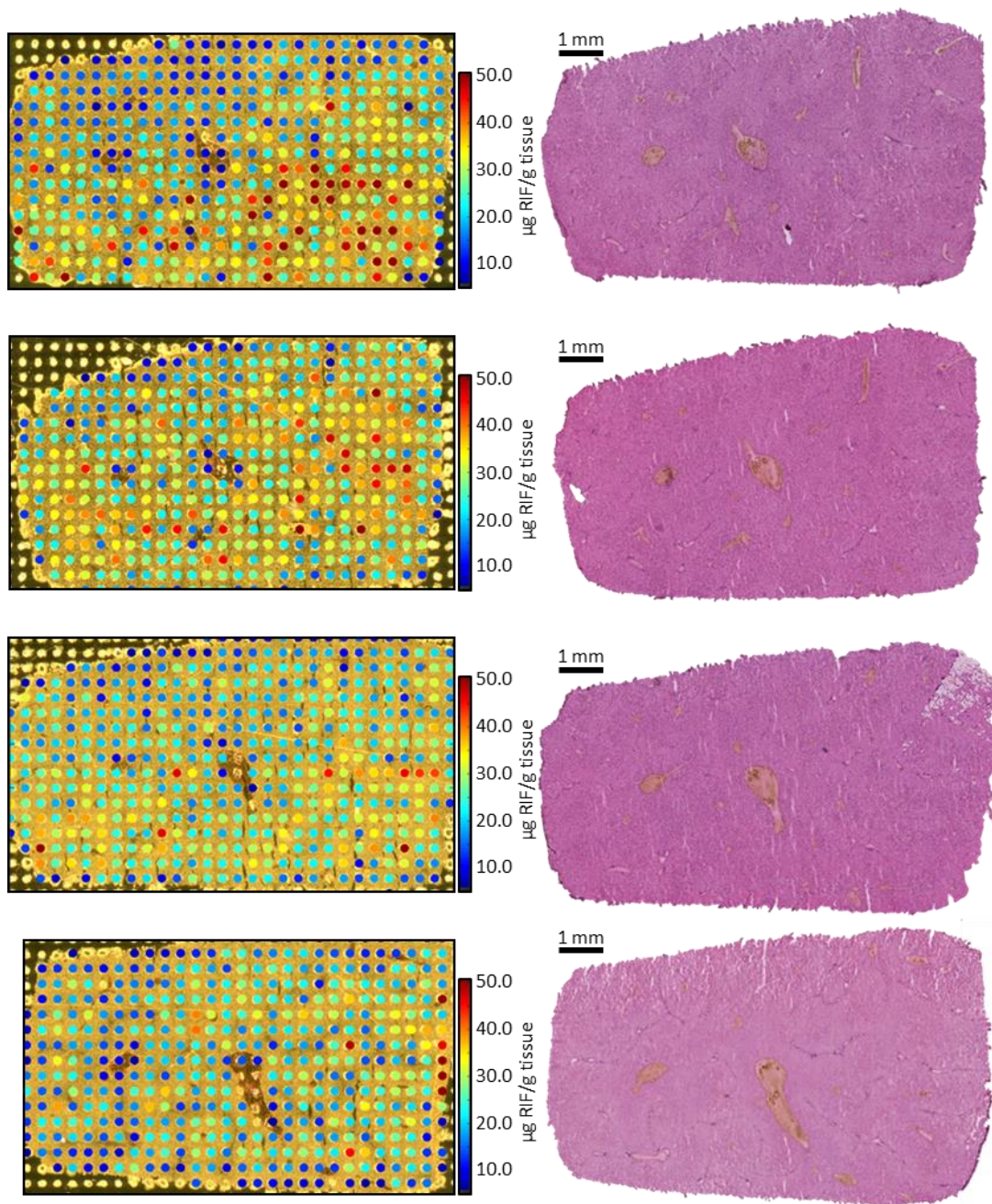


Figure 3.8. Four replicate quantitative MALDI IMS images of RIF (left) and serial sections stained with H&E (right) of a liver dosed *in vivo*. As with the previous image (duplicated here at the top), very little RIF is detected in the blood vessels in the replicate images.

These data support previous observations of a three-dimensional liver acinus in which pharmaceutical drug concentrations vary as well as observations of the overall homogeneity of

drug concentrations within livers.⁴⁵ All of the tissue microenvironments contribute to this average from HPLC-MS/MS, but the quantitative MALDI IMS data elucidates the localization of RIF within the microenvironments.

Quantitative MALDI IMS of Liver Using Multiplexed MALDI TOF/TOF

The quantitative capabilities of MALDI IMS were demonstrated on a linear ion trap mass spectrometer, but that platform is much slower in comparison to a MALDI time-of-flight/time-of-flight (TOF/TOF) mass spectrometer capable of continuous laser raster sampling.^{51, 52} In the quantitative imaging experiments analyzed using linear ion trap mass spectrometer, each microspot was analyzed individually to reduce analysis time. With the MALDI TOF/TOF mass spectrometer, the entire area of the tissue including those without any standards or matrix, were interrogated with the laser, and the resulting image was examined for the calibration standards and dosed tissue microspots. The MALDI TOF/TOF mass spectrometer utilized in these experiments (300 Tandem, SimulTOF Systems, Sudbury, MA) also has the capability of multiplexed MS/MS analysis as described in Chapter II. Multiple precursor ions may be selected by the timed ion selector (TIS) and analyzed for their fragments as long as there is greater than 6-7% difference in their m/z .

A different region of the liver from the New Zealand white rabbit infected with *Mycobacterium tuberculosis* and orally administered a cocktail of rifampicin, isoniazid, pyrazinamide, and moxifloxacin (30/50/125/25 mg/kg) and sacrificed 4 hours and 21 minutes after the final dose was utilized for these analyses.⁴² A 12 μm thick section dosed rabbit liver was thaw-mounted onto a gold-coated stainless steel target and analyzed using quantitative MALDI IMS with a MALDI TOF/TOF mass spectrometer (300 Tandem). A serial section was

stained with H&E for histological comparisons. A 12 μm thick section of a control liver was also thaw-mounted onto the target for the calibration curve microspots. Because of the ability to perform multiplexed MS/MS analysis from a single laser shot, rifapentine was used as the internal standard. Rifapentine is structurally similar to RIF with the addition of a pentane group. Additionally, RIF has previously been used as an internal standard for quantitative HPLC-MS/MS analysis of rifapentine.⁵³ Calibration solutions of RIF (4.00-24.0 μM RIF with 20.0 μM rifapentine) were deposited onto the non-dosed liver tissue section using 40 passes of 2 droplets each with the robotic spotter. A QC solution (14.0 μM RIF with 20.0 μM rifapentine) was also deposited onto the non-dosed section. The internal standard was deposited in a microspotted array with a spatial resolution of 1 mm across the tissue dosed *in vivo*. The matrix (20 mg/mL THAP in 50% ethanol/water) was deposited onto the calibration standard and dosed tissue microspots using 4 passes of 100 droplets each. Altering the number of passes and the number of droplets deposited for each pass with the robotic spotter increased to diameter of the spots to $508.8 \pm 13.0 \mu\text{m}$ and improved the sensitivity of the method. The larger microspots allowed for more of the analyte to be extracted into the matrix from the dosed tissue sections but led to poorer spatial resolution. Lower sensitivity for small molecules is common with TOF/TOF instruments utilizing post-source decay for fragmentation, because it is not tunable for a particular ion.

The calibration microspots and the microspots on the dosed tissue section were analyzed using a 300 Tandem TOF/TOF mass spectrometer and a laser energy of 66 $\mu\text{J}/\text{pulse}$ as measured prior to attenuation. The instrument was operated in negative ion MS/MS mode at 4 kV with continuous laser raster sampling. The data were acquired in typewriter imaging mode using a 1

kHz laser repetition rate, 1 mm/s stage velocity, 50 hardware averages, and 50 μm vertical step size, resulting in 50 μm by 50 μm pixel sizes.

Following the acquisition, spectral averages were manually exported using a region of interest selection tool from each microspot. The spectral intensities for the RIF and rifapentine fragments (m/z 397 and 452, respectively, as shown in Figure 3.9A) from the calibration standard microspots were used to generate a calibration curve (Figure 3.9B) by plotting the average intensity ratio of the major fragment ion of RIF to the intensity of the major fragment ion of rifapentine [m/z 397/ m/z 452] versus the concentration of RIF applied to the tissue section (8 microspots for each concentration).

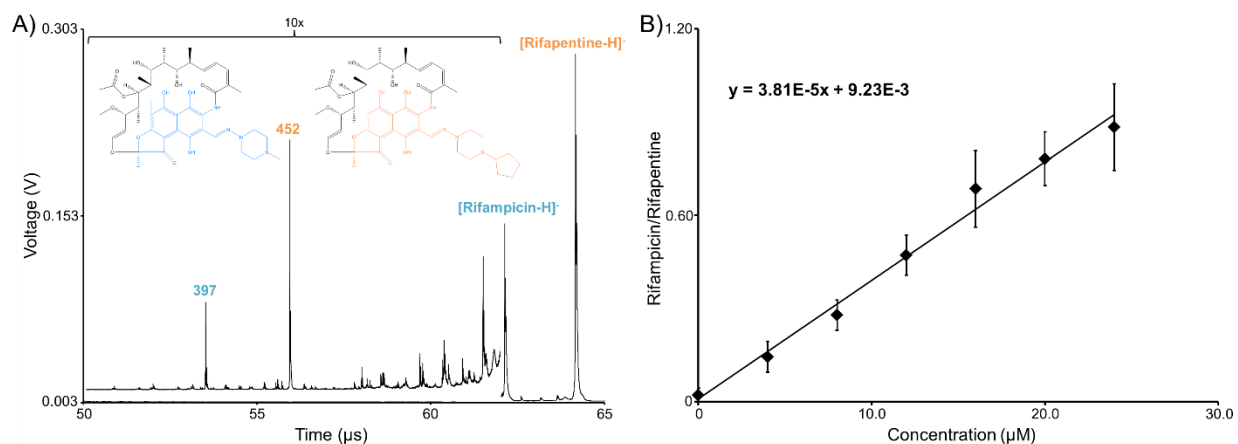


Figure 3.9. Multiplexed MALDI MS/MS spectrum and fragmentation of RIF and rifapentine (A) and the generated calibration curve (B) from the calibrations standards on a non-dosed tissue section.

The quantitative MALDI MS/MS image (Figure 3.10) was generated with in-house software developed using MATLAB. As with the liver sections analyzed using the linear ion trap mass spectrometer, less RIF was detected in the blood vessels than the tissue. Because of the worse

spatial resolution, however, less information may be inferred about the microphysiology of the drug. However, this methodology allowed for the analysis of a structural analogue as the internal standard and did not require the synthesis of an isotopically labeled standard, which can be complex and expensive. When the concentrations of RIF detected from each microspot were averaged together, the amount of RIF detected in the liver was 25.0 μg RIF/g tissue.

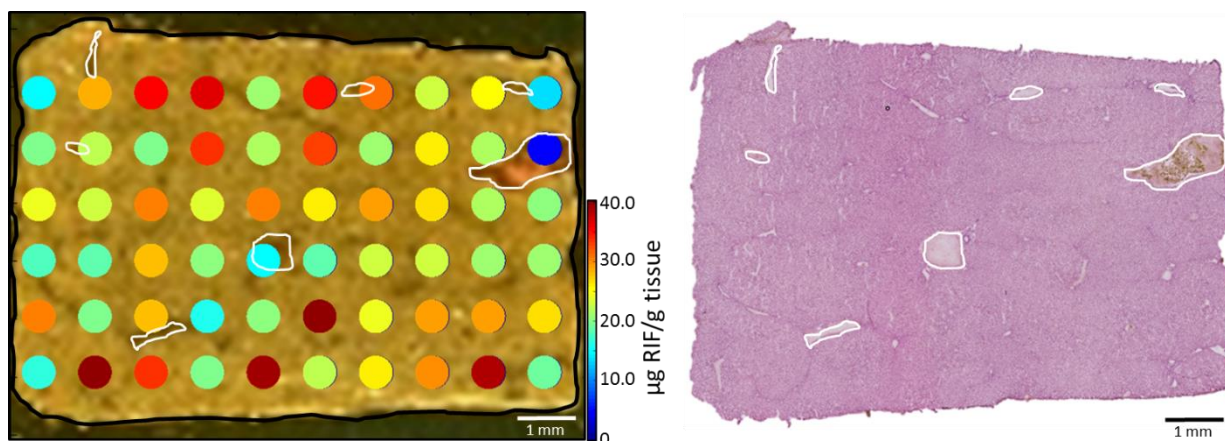


Figure 3.10. Quantitative MALDI IMS image (left) and H&E stained serial section (right) of a liver dosed *in vivo* with RIF and analyzed using a high-speed MALDI TOF/TOF mass spectrometer with multiplexing. As with the previous images of the liver, less RIF was detected in the blood vessels, which are outlined in white in the image and the H&E stained section.

To further validate the quantitative measurements using the high-speed MALDI TOF/TOF with multiplexed MS/MS capabilities, this tissue was also analyzed by HPLC-MS/MS using the methods for analyzing the tissues dosed *in vitro*. Briefly, the dosed liver and a control liver were cut (~80 mg) and homogenized in 10% methanol/water (~30 mg/mL). Stock solutions of RIF (0.466 mg/mL) and $^{13}\text{C},^2\text{H}$ -RIF (0.376 mg/mL) were used to spike calibration standards (2.58E-3 to 5.16E-1 μg RIF with 1.88E-1 μg $^{13}\text{C},^2\text{H}$ -RIF) into 150 μL of the control liver

homogenate. Only the internal standard was spiked into 150 μL of the dosed tissue homogenates. Using the previously published methods, they were analyzed using HPLC-MS/MS (Agilent 6430) with a C18 column. As with the previously analyzed tissue, the average amounts of RIF detected in the quantitative MALDI MS/MS image (25.0 μg RIF/g tissue) and from the HPLC-MS/MS (23.2 μg RIF/g tissue) of the extract were in agreement (92%). Furthermore, the same quantitative information and localization were achieved using the two different instruments. The amounts detected from this portion of the liver using a MALDI TOF/TOF mass spectrometer (25.0 μg RIF/g tissue) and from the same liver using the MALDI LTQ mass spectrometer (22.9 μg RIF/g tissue) were in agreement. These data indicate accurate quantitative IMS can be performed and compared using different mass analyzers.

Conclusions

Utilizing a tissue dosed *in vitro*, different methods of applying internal and calibration standards to tissue sections for quantitative MALDI IMS using an acoustic robotic spotter were examined, and depositing the standards onto the section followed by the matrix was optimal and produced no statistically significant difference from HPLC-MS/MS results.

Once the method of standard application was validated, quantitative MALDI MS/MS images were generated using a linear ion trap mass spectrometer and a high-speed MALDI TOF/TOF mass spectrometer with each microspot representing a measured concentration of RIF from a 12 μm thick section of a tissue dosed *in vivo*. It is important to note that both of these instruments have MS/MS capabilities to improve the sensitivity and selectivity of the method. Without MS/MS, the quantitative analysis of pharmaceutical drugs can be complicated by

spectral interferences. These two platforms allow for the confirmation of the structure to ensure the correct analyte of interest is measured.

The microspots in the quantitative MALDI MS/MS images were equal in size to those reproducibly analyzed for the calibration curve (RSDs less than 10%) and for the QC solution allowing the method to be assessed on the scale of a single microspot. When the average concentration from the quantitative MALDI IMS data were compared to the concentration from HPLC-MS/MS data, the data were 90.4% similar. Quantitative MALDI IMS, however, provided additional information about the absolute concentration detected from the microenvironments within the tissue. Less RIF was detected from the blood vessels, and a gradient of RIF was also detected radiating from the portal tracts indicating the microphysiology of metabolism within the liver.

References

1. C. W. Chumbley, M. L. Reyzer, J. L. Allen, G. A. Marriner, L. E. Via, C. E. Barry III and R. M. Caprioli, *Analytical Chemistry*, 2016, **88**, 2292-2398.
2. R. M. Caprioli, T. B. Farmer and J. Gile, *Analytical Chemistry*, 1997, **69**, 4751-4760.
3. F. J. Troendle, C. D. Reddick and R. A. Yost, *Journal of the American Society for Mass Spectrometry*, 1999, **10**, 1315-1321.
4. M. L. Reyzer, Y. S. Hsieh, K. Ng, W. A. Korfmacher and R. M. Caprioli, *Journal of Mass Spectrometry*, 2003, **38**, 1081-1092.
5. J. A. Hankin and R. C. Murphy, *Analytical Chemistry*, 2010, **82**, 8476-8484.
6. S. L. Koeniger, N. Talaty, Y. P. Luo, D. Ready, M. Voorbach, T. Seifert, S. Cepa, J. A. Fagerland, J. Bouska, W. Buck, R. W. Johnson and S. Spanton, *Rapid Communications in Mass Spectrometry*, 2011, **25**, 503-510.
7. N. Takai, Y. Tanaka, K. Inazawa and H. Saji, *Rapid Communications in Mass Spectrometry*, 2012, **26**, 1549-1556.
8. M. Lagarrigue, R. Lavigne, E. Tabet, V. Genet, J. Thome, K. Rondel, B. Guevel, L. Multigner, M. Samson and C. Pineau, *Analytical Chemistry*, 2014, **86**, 5775-5783.
9. M. R. Groseclose and S. Castellino, *Analytical Chemistry*, 2013, **85**, 10099-10106.
10. N. Takai, Y. Tanaka and H. Saji, *Mass Spectrometry*, 2014, **3**.
11. L. Jadoul, R. Longuespee, A. Noel and E. De Pauw, *Anal Bioanal Chem*, 2014.
12. G. Hamm, D. Bonnel, R. Legouffe, F. Pamelard, J. Delbos, F. Bouzom and J. Stauber, *Journal of Proteomics*, 2012, **75**, 4952-4961.

13. R. J. A. Goodwin, C. L. Mackay, A. Nilsson, D. J. Harrison, L. Farde, P. E. Andren and S. L. Iverson, *Analytical Chemistry*, 2011, **83**, 9694-9701.
14. D. A. Pirman and R. A. Yost, *Analytical Chemistry*, 2011, **83**, 8575-8581.
15. D. A. Pirman, R. F. Reich, A. Kiss, R. M. A. Heeren and R. A. Yost, *Analytical Chemistry*, 2013, **85**, 1081-1089.
16. S. R. Ellis, A. L. Bruinen and R. M. A. Heeren, *Analytical and Bioanalytical Chemistry*, 2014, **406**, 1275-1289.
17. R. F. Reich, K. Cudzilo, J. A. Levisky and R. A. Yost, *Journal of the American Society for Mass Spectrometry*, 2010, **21**, 564-571.
18. J. Stauber, *Bioanalysis*, 2012, **4**, 2095-2098.
19. B. Prideaux and M. Stoeckli, *Journal of Proteomics*, 2012, **75**, 4999-5013.
20. A. Kubo, M. Kajimura and M. Suematsu, *Mass Spectrom (Tokyo)*, 2012, **1**.
21. T. Porta, A. Lesur, E. Varesio and G. Hopfgartner, *Analytical and Bioanalytical Chemistry*, 2015, **407**, 2177-2187.
22. Y. Hsieh, R. Casale, E. Fukuda, J. W. Chen, I. Knemeyer, J. Wingate, R. Morrison and W. Korfmacher, *Rapid Communications in Mass Spectrometry*, 2006, **20**, 965-972.
23. A. Nilsson, T. E. Fehniger, L. Gustavsson, M. Andersson, K. Kenne, G. Marko-Varga and P. E. Andren, *Plos One*, 2010, **5**, e11411.
24. T. E. Fehniger, A. Vegvari, M. Rezeli, K. Prikk, P. Ross, M. Dahlback, G. Edula, R. Sepper and G. Marko-Varga, *Analytical Chemistry*, 2011, **83**, 8329-8336.
25. E. J. Clemis, D. S. Smith, A. G. Camenzind, R. M. Danell, C. E. Parker and C. H. Borchers, *Analytical Chemistry*, 2012, **84**, 3514-3522.
26. R. R. Landgraf, T. J. Garrett, M. C. P. Conaway, N. A. Calcutt, P. W. Stacpoole and R. A. Yost, *Rapid Communications in Mass Spectrometry*, 2011, **25**, 3178-3184.
27. D. A. Pirman, A. Kiss, R. M. A. Heeren and R. A. Yost, *Analytical Chemistry*, 2013, **85**, 1090-1096.
28. A. Buck, S. Halbritter, C. Spath, A. Feuchtinger, M. Aichler, H. Zitzelsberger, K. P. Janssen and A. Walch, *Anal Bioanal Chem*, 2014.
29. J. Bunch, M. R. Clench and D. S. Richards, *Rapid Communications in Mass Spectrometry*, 2004, **18**, 3051-3060.
30. B. Prideaux, V. Dartois, D. Staab, D. M. Weiner, A. Goh, L. E. Via, C. E. Barry and M. Stoeckli, *Analytical Chemistry*, 2011, **83**, 2112-2118.
31. P. Kallback, M. Shariatgorji, A. Nilsson and P. E. Andren, *Journal of Proteomics*, 2012, **75**, 4941-4951.
32. T. Nakanishi, S. Takai, D. Jin and T. Takubo, *Mass Spectrometry*, 2013, **2**.
33. S. Schulz, D. Gerhardt, B. Meyer, M. Seegel, B. Schubach, C. Hopf and K. Matheis, *Analytical and Bioanalytical Chemistry*, 2013, **405**, 9467-9476.
34. S. Yamori, S. Ichiyama, K. Shimokata and M. Tsukamura, *Microbiology and Immunology*, 1992, **36**, 361-368.
35. H. R. Aerni, D. S. Cornett and R. M. Caprioli, *Analytical Chemistry*, 2006, **78**, 827-834.
36. K. Shrivastava, T. Hayasaka, N. Goto-Inoue, Y. Sugiura, N. Zaima and M. Setou, *Analytical Chemistry*, 2010, **82**, 8800-8806.
37. R. J. Vijn, H. J. Arts, R. Green and A. M. Castelijns, *Synthesis*, 1994, 573-578.

38. C. Bartolucci, L. Cellai, P. Difilippo, A. Segre, M. Brufani, L. Filocamo, A. D. Bianco, M. Guiso, V. Brizzi, A. Benedetto, A. Dicaro and G. Elia, *Farmaco*, 1992, **47**, 1367-1383.
39. M. Brufani, L. Cellai, B. Bartolini, I. Medici, B. M. Lagrasta, Patent WO200901055 A1, 2009.
40. M. Taguchi, Y. Yamane, N. Aikawa and G. Tsukamoto, *Chemical & Pharmaceutical Bulletin*, 1988, **36**, 4157-4161.
41. P. F. Fang, H. L. Cai, H. D. Li, R. H. Zhu, Q. Y. Tan, W. Gao, P. Xu, Y. P. Liu, W. Y. Zhang, Y. C. Chen and F. Zhang, *Journal of Chromatography B-Analytical Technologies in the Biomedical and Life Sciences*, 2010, **878**, 2286-2291.
42. M. C. Kjellsson, L. E. Via, A. Goh, D. Weiner, K. M. Low, S. Kern, G. Pillai, C. E. Barry, III and V. Dartois, *Antimicrobial Agents and Chemotherapy*, 2012, **56**, 446-457.
43. A. Nakajima, T. Fukami, Y. Kobayashi, A. Watanabe, M. Nakajima and T. Yokoi, *Biochemical Pharmacology*, 2011, **82**, 1747-1756.
44. K. Jungermann and N. Katz, *Physiological Reviews*, 1989, **69**, 708-764.
45. N. R. Katz, *Journal of Nutrition*, 1992, **122**, 843-849.
46. K. O. Lindros, *General Pharmacology*, 1997, **28**, 191-196.
47. T. Oinonen and K. O. Lindros, *Biochemical Journal*, 1998, **329**, 17-35.
48. J. Woo, W. Cheung, R. Chan, H. S. Chan, A. Cheng and K. Chan, *Clinical Biochemistry*, 1996, **29**, 175-177.
49. United States Food and Drug Administration, *Guidance for Industry: Bioanalytical Validation*, 2001.
50. T. A. Little, *Biopharm International*, 2015, **28**, 48-51.
51. J. M. Spraggins and R. M. Caprioli, *Journal of the American Society for Mass Spectrometry*, 2011, **22**, 1022-1031.
52. B. M. Prentice, C. W. Chumbley and R. M. Caprioli, *Journal of Mass Spectrometry*, 2015, **50**, 703-710.
53. T. L. Parson, M. A. Marzinke, T. Hoang, E. Bliven-Sizemore, M. Weiner, W. R. Mac Kenzie, S. E. Dorman and K. E. Dooley, *Antimicrobial Agents and Chemotherapy*, 2014, **58**, 6747-6757.

CHAPTER IV

QUANTITATIVE MATRIX-ASSISTED LASER DESORPTION/IONIZATION IMAGING MASS SPECTROMETRY OF PROMETHAZINE DIRECTLY FROM LIVER AND KIDNEY TISSUE SECTIONS

Introduction

The validation of quantitative matrix-assisted laser desorption/ionization (MALDI) imaging mass spectrometry (IMS) of drug-dosed tissues on a microspotted pixel size regime was initially performed analyzing for rifampicin (RIF) in liver tissues (Chapter III).¹ While liver tissue is mostly homogenous consisting of hepatocytes and blood vessels, MALDI IMS has the capability of elucidating the distribution of compounds throughout an entire tissue section, including those from tissues containing heterogeneous microenvironments, such as the kidney or brain.²⁻⁶ Different tissue types, however, can cause extraction and ionization efficiency differences for the pharmaceutical drug of interest.⁷ When appropriately applied to dosed tissue sections, isotopically labeled internal standards account for this effect in bulk tissue quantitative measurements, but the methods have not been applied to different tissue types within a single tissue section.⁸⁻¹³

The methods developed to analyze the quantitative distribution of RIF in liver tissues were also applied to liver and kidney tissues dosed with promethazine (PMZ). PMZ is less polar than RIF with a partition coefficient of 4.8 compared to 2.7 in 50% octanol/water.¹⁴ It is a neuroleptic drug commonly prescribed as an antihistamine to treat allergic reactions or rhinitis. As demonstrated herein, PMZ is retained in mouse brains containing amyloid beta (A β) plaques

and is a potential positron emission tomography (PET) scan contrast agent for Alzheimer's disease progression.¹⁵ The liver and kidney tissues from wildtype and diseased animals were further analyzed using quantitative MALDI IMS to demonstrate the capability of the technology to analyze a different pharmaceutical drug in tissues with different microenvironments.

Detection of Promethazine as a Potential Probe for Amyloid Beta in the Brain

Large portions of this section were adapted with permission from R. A. McClure et al.,

NeuroImage: Clinical, Copyright 2013.¹⁵

At present, the diagnosis of Alzheimer's disease is assigned clinically by assessing a patient's late-stage cognitive abilities in the context of age, family history, and other risk factors.¹⁶⁻¹⁸ However, due to the phenotypic similarities of neurological disorders included in the differential diagnosis of cognitive impairment, it is difficult to accurately differentiate Alzheimer's disease from causes of dementia unrelated to A β . This remains a bottleneck to both clinical therapeutics and basic research.¹⁹⁻²⁵

Previous studies have demonstrated Alzheimer's disease pathogenesis follows a temporally rapid and predictable course with respect to the regional distribution of A β plaque deposition in the brain.²⁶ Thus, diagnostic strategies targeting A β plaques gain a key advantage over other Alzheimer's disease biomarkers in their ability to detect subtle changes in A β deposition early in the course of Alzheimer's disease pathogenesis. Unfortunately, once considerable plaque deposition has occurred, treatments aimed at abolishing these protein aggregations have limited efficacy in restoring cognitive function because of the irreversible nature of neuronal damage. Therefore, early Alzheimer's disease diagnosis and prevention are of paramount importance in Alzheimer's disease research and represent the best option for curtailing the

disease burden. Despite the discovery of potentially effective therapeutic approaches, the clinical impact of Alzheimer's disease treatments remains underwhelming due in part to a lack of reliable methodologies to screen for Alzheimer's disease pathology.²⁷⁻³¹

Of the early diagnostic modalities for Alzheimer's disease, A β imaging has emerged as the most promising approach for developing a noninvasive yet clinically impactful diagnostic methodology.³²⁻³⁶ The most common modalities for amyloid imaging include optical imaging, magnetic resonance imaging (MRI), and PET approaches. For example, optical imaging has been used to monitor the development of a single A β plaque and to reveal subtle neurite geometry changes occurring in and around diffused plaques.³⁷ Structural MRI boasts the greatest number of potential contrast agents and provides exquisite anatomical contrast due to its high spatial resolution. Additionally, functional MRI and volumetric MRI have been utilized to predict Alzheimer's disease onset with nearly 80% accuracy.³⁸⁻⁴² Nevertheless, despite the potential advantages offered by MRI and other optical-based methodologies, PET imaging is still considered the most practical approach because of its sensitivity, detection depth, and the ability of PET probes to retain binding affinity for neuroimaging of A β plaques.^{43, 44} Despite the real-world availability of PET, amyloid imaging by PET is currently limited by the scarcity of specific molecular probes capable of binding to A β . Today, the few probes available for PET-based human amyloid imaging include ¹⁸F-BAY94-9172 (¹⁸FAV-1),⁴⁵ ¹⁸F-Florbetapir (¹⁸FAV-45),⁴⁶ ¹⁸F-Florbetaben,⁴⁷ and ¹¹C-PIB.⁴⁸⁻⁵¹

A combinatorial approach integrating a novel high-throughput A β -thioflavin competitive binding optical (HATCO) assay with MALDI IMS was developed to facilitate the screening of diverse compound libraries for molecules with the ability to bind to A β . The HATCO assay was

developed in Wellington Pham's laboratory with the methodology described herein. MALDI IMS provided complimentary data unobtainable with the HATCO assay alone by facilitating the direct analysis of intact tissue sections and preserving the spatial distribution of molecules. Thus, MALDI IMS analyses of HATCO-discovered hits enabled the assessment of the molecule's retention pattern in the brain with a comparison to known and measured regions of A β distribution.⁵²

Thioflavin is a topologically activated dye that binds specifically to A β .^{25, 53} This compound possesses substantial conformational freedom in free solution and exhibits a relatively low fluorescence signal. However, upon binding to A β , thioflavin's conformational freedom is dramatically reduced. This increase in structural rigidity decreases the vibrational-rotational processes available to the thioflavin molecule, contributing to an observed increase in fluorescence when thioflavin is bound to A β compared to the unbound molecule.⁵⁴ Although increased thioflavin fluorescence alone is highly indicative of the thioflavin molecule existing in an A β -bound state, further validation includes a characteristic spectral shift in fluorescence signal observed when it is bound to A β . When not complexed with A β , thioflavin emits a weak fluorescent signal at a λ_{max} of 440-445 nm. However, binding to A β results in a strong fluorescent signal with a λ_{max} shifted to approximately 480 nm.^{55, 56} These unique characteristics of thioflavin were employed to develop the HATCO assay screening compounds for their ability to bind to A β in the brain using a high-throughput approach.

In an effort to utilize the most clinically relevant A β plaques possible, fresh brain lysates were obtained from a transgenic mouse model (5XFAD) overexpressed with human amyloid precursor protein and presenilin 1. They were analyzed using a Bradford assay to ensure an

equal amount of protein was present in each assay. Before performing a specific displacement study, a series of control experiments were conducted to assess whether the candidate compounds (naltrexone, Haldol, astemizole, minocycline, and promethazine) emitted or absorbed at wavelengths overlapping with thioflavin's excitation or emission spectra and to demonstrate the specificity of thioflavin toward A β . When the compounds were mixed (250 μ M) with thioflavin in the absence of A β , no modulation of thioflavin fluorescence was observed (Figure 4.1A). The candidate compounds did not bind to thioflavin directly and were incapable of interfering with the fluorescence spectra. Furthermore, mixing thioflavin (10 μ M) with the 5XFAD brain lysate (35 mg/mL) resulted in a nearly nineteen-fold enhancement in thioflavin fluorescence signal compared to the PBS sample ($p < 0.0001$). The fluorescence signal of thioflavin in the presence of the 5XFAD lysate also exhibited a λ_{max} of 480 nm, a characteristic of thioflavin bound to A β . By comparison, the thioflavin mixed with PBS emitted most strongly at 440 nm, the λ_{max} associated with unbound thioflavin.

In a more rigorous demonstration of thioflavin's specificity for 5XFAD-derived A β plaques, the same thioflavin concentration (10 μ M) was spiked into the brain lysate isolated from a wildtype mouse lacking A β plaques. Despite some degree of non-specific binding, a difference in fluorescence signal enhancement was observed between the A β -containing 5XFAD lysate and the A β -deficient wildtype lysate (Figure 4.1B), which confirmed thioflavin fluorescence could be used as a reliable reporter to identify A β -binding compounds. Furthermore, spectral analysis of thioflavin's fluorescence in the presence of the wildtype lysate yielded a λ_{max} of 440 nm compared to the λ_{max} of 480 nm observed in the 5XFAD trials. This spectral shift confirmed thioflavin fluorescence signal could be reliably used in HATCO assays to reflect the proportion

of thioflavin bound to A β . Thus, any observed modulation in thioflavin fluorescence when the compounds were added would not represent the dissociation of thioflavin from non-A β proteins, as these complexes do not contribute to the measured thioflavin signal at 480 nm.

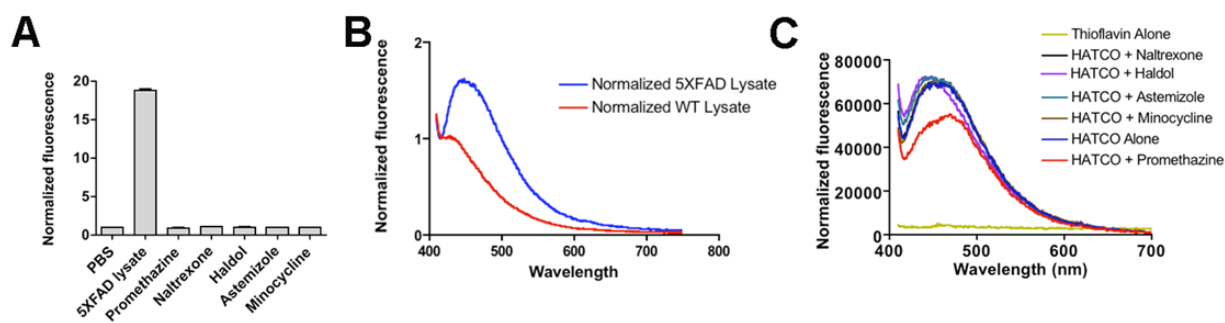


Figure 4.1. HATCO assay screening compound libraries for A β -binding capacity. Fluorescence signal of thioflavin in the presence of freshly isolated 5XFAD brain lysate, PBS, or candidate compounds (A) demonstrating a nineteen-fold increase in thioflavin fluorescence in the presence of 5XFAD lysate compared to PBS and compound library trials (n=3; p-value < 0.0001). The spectral shift in λ_{max} to 480 nm in the presence of 5XFAD lysate (B) arises as a consequence of thioflavin-A β complexes. Increased fluorescence secondary to the presence of A β -containing 5XFAD lysate is attenuated by the addition of PMZ but not by other candidate compounds (C). PMZ reduces the fluorescence at 480 nm by 15.6% with respect to PBS (n=3; p-value < 0.0001).

The ability of the candidate compounds to competitively displace thioflavin binding to A β plaques was then examined. If thioflavin was dissociated from A β plaques by a compound competitively binding, the fluorescence signal of thioflavin would be reduced. 5XFAD brain lysates with normalized protein concentrations were treated with thioflavin (10 μ M) in quartz cuvettes and allowed to equilibrate for 30 minutes before the addition of the compounds (250 μ M). After equilibration, the proportion of thioflavin molecules bound to A β plaques in solution was measured using fluorescence spectroscopy (Photon Technology International, Edison, NJ). Among the analyzed compounds, only PMZ yielded a notable reduction (19%; p-

value < 0.0001) in fluorescence signal of thioflavin (Figure 4.1C). This indicated it had potential to bind to A β within the brains of 5XFAD mice.

After the successful lysate studies, PMZ was administered to mice for *in vivo* analyses. The localizations of PMZ and A β in the brains of 5XFAD and wildtype mice were analyzed in a single coronal section of each brain using MALDI IMS (Figure 4.2). A total of three different animals were examined for each of the following groups: non-dosed 8-month-old 5XFAD mice, dosed 2-month-old and 8-month-old 5XFAD mice, and dosed 8-month-old wildtype mice. Dosed animals were administered 25 mg/kg PMZ five times via tail vein injections with the non-dosed animal receiving phosphate-buffered saline as a control. They were sacrificed 4 hours after the final dose. The brains were resected, flash-frozen, and stored at -80°C until analysis.

Mouse brain coronal sections (12 μ m thick) were thaw-mounted onto gold-coated, stainless steel target plates and stored at room temperature in a vacuum desiccator until analysis. A serial section was obtained on a glass slide and stained using hematoxylin and eosin (H&E). The tissue sections were manually coated with matrix [30 mg/mL 2,5-dihydroxybenzoic acid (DHB) in 50% methanol/water with 0.1% trifluoroacetic acid] using a glass thin-layer chromatography reagent sprayer (Kontes Glass Company, Vinland, NJ). The matrix was applied by passing the sprayer across the tissue section several times and allowing it to dry. This process was repeated approximately 20 times to ensure a homogeneous coating of matrix crystals formed on the tissue section while minimizing analyte delocalization.

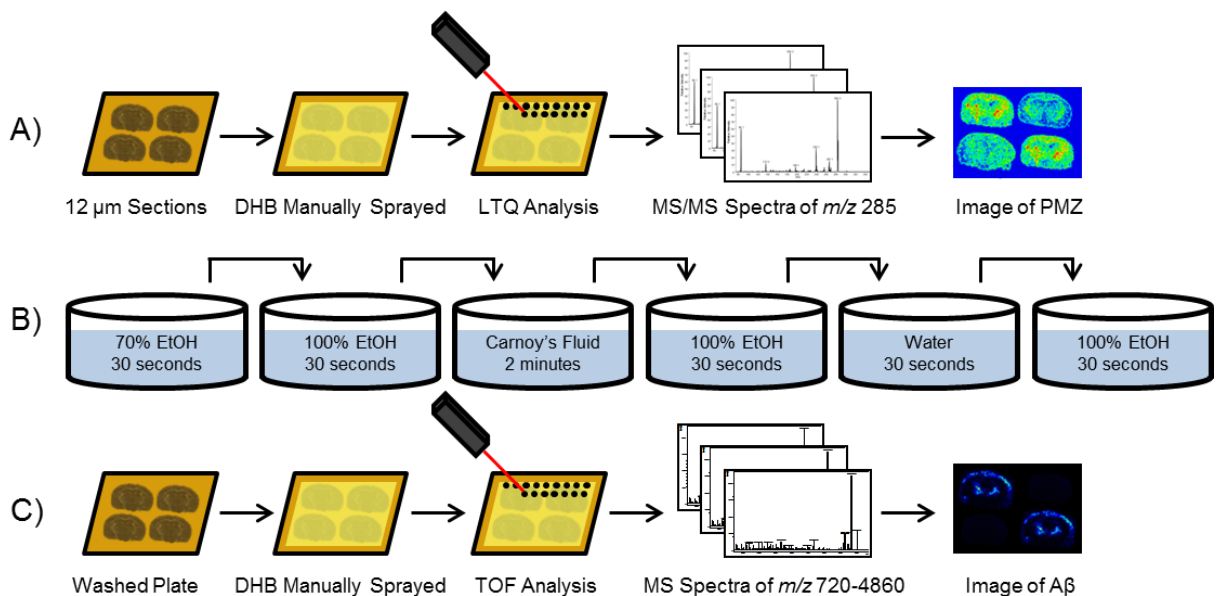


Figure 4.2. Methods for analyzing the same tissue sections for PMZ and A β using IMS. The sections were analyzed for PMZ on an LTQ MS after manually coating the sections with DHB (A). The sections were then washed (B) and analyzed for A β using a TOF MS.

The samples were first analyzed for PMZ using a linear ion trap mass spectrometer equipped with a MALDI source (LTQ XL, Thermo Scientific, Waltham, MA). MS/MS spectra for PMZ were acquired over the entire tissue section at a spatial resolution of 100 μm . The precursor ion for PMZ (m/z 285.1 \pm 0.5) was isolated and fragmented using a normalized collision energy of 27%. Main fragment ions were formed at m/z 86 and 198, likely corresponding to fragmentation at the phenothiazine-*N*, as well as at m/z 240, likely corresponding to the loss of the dimethylamine moiety.⁵⁷ Images representative of the distribution of PMZ across the tissue section were generated by plotting the summed intensity of the main fragment ions at m/z 86 and 240 at each pixel using ImageQuest software (Thermo Scientific, Waltham, MA).

The samples on the target previously analyzed for PMZ were then washed in sequential steps of 70% ethanol, 100% ethanol, Carnoy's solution (60% ethanol, 30% chloroform, 10% acetic

acid), and deionized water to remove the matrix and potential ion suppressants such as lipids and salts. After reapplying the same matrix using the previously described method, the brain sections were analyzed for A β peptides using a MALDI time-of-flight/time-of-flight (TOF/TOF) mass spectrometer (ultrafleXtreme, Bruker Daltonics, Billerica, MA) in reflectron mode. They were analyzed in positive ion mode at a spatial resolution of 150 μ m for the mass range m/z 2,500-7,000. Ion images for the peptide at m/z 4,329 containing the first 40 amino acid residues of amyloid beta (A β_{40}) were constructed in flexImaging software (Bruker Daltonics, Billerica, MA).

As demonstrated by the MALDI images (Figure 4.3), PMZ and A β_{40} were detected in the same regions of the dosed 5XFAD brain. The PMZ signal was nearly tripled in the dosed 8-month-old 5XFAD brain than in the dosed wildtype or dosed 2-month-old 5XFAD brain. No PMZ was detected in the non-dosed brain, indicating no biological interferences were detected for these m/z values (m/z 86 and 240). Additionally, no A β_{40} was detected in the wildtype brain, indicating there were no biological interferences detected for m/z 4,329. A lack of A β_{40} signal in the 2-month-old mice is consistent with the slow speed of Alzheimer's disease progression. The imaging data support the lysate studies with respect to the specificity of PMZ for A β plaques after crossing the blood-brain barrier and its potential for assessing Alzheimer's disease pathology.

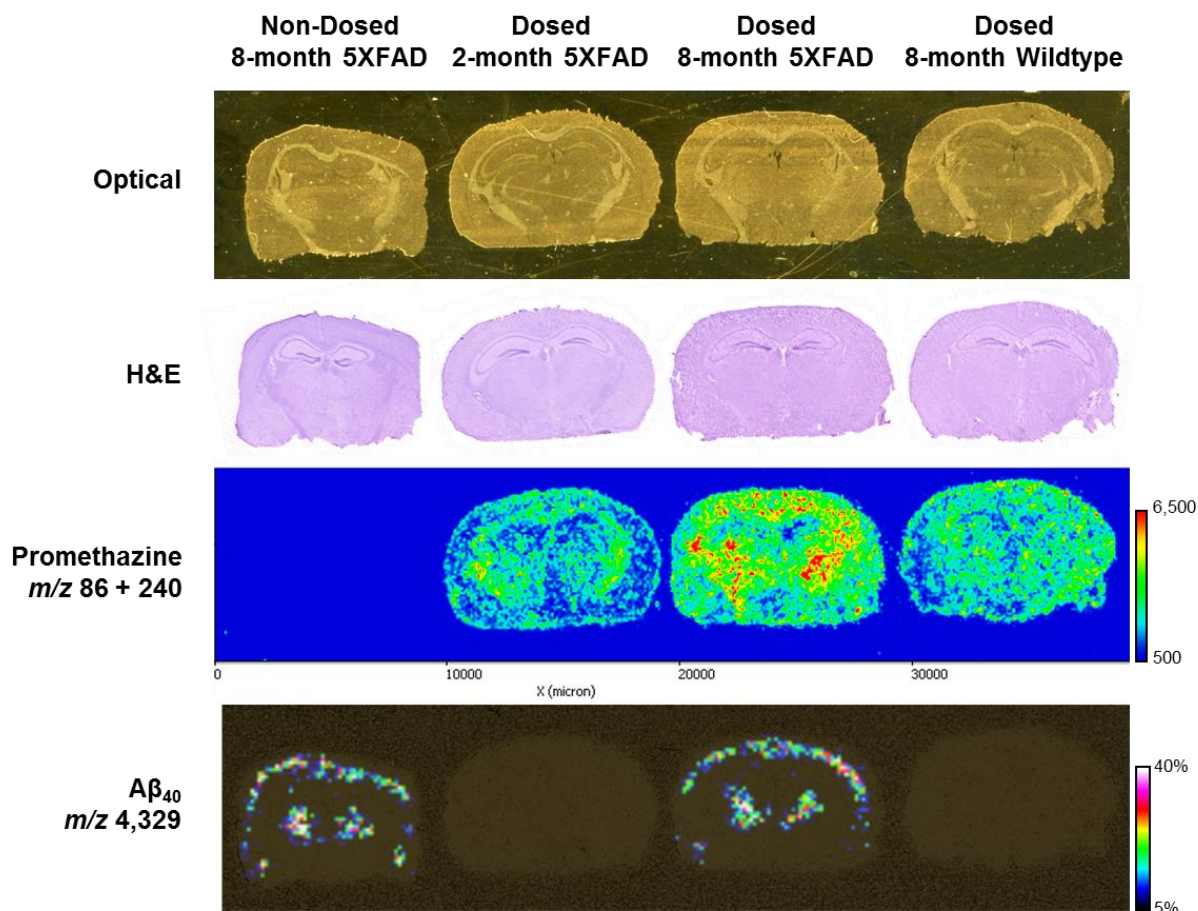


Figure 4.3. Optical image, H&E serial section microscope scans, PMZ image, and $A\beta_{40}$ image for sections of a non-dosed 8-month-old 5XFAD brain, a dosed 2-month-old 5XFAD brain, a dosed 8-month-old 5XFAD brain, and a dosed 8-month-old wildtype brain. PMZ and $A\beta_{40}$ were detected within the 8-month-old 5XFAD brain and localized to the same regions.

To confirm the peptide identification, matrix (30 mg/mL DHB in 50% methanol/water with 0.1% trifluoroacetic acid) was hand-spotted onto a 5XFAD brain section and analyzed in LIFT mode on a MALDI TOF/TOF mass spectrometer (ultrafleXtreme).³ The precursor ion for $A\beta_{40}$ (m/z 4,329 \pm 5) was isolated and fragmented for identification.^{58, 59} A total of 35,000 laser shots were summed to enhance the signal-to-noise ratio. Database searching was performed using

BioTools (Bruker Daltonics, Billerica, MA) and the Mascot database. The MS/MS spectrum (Figure 4.4) includes the labels for the fragment ions in the sequence detected for A β ₄₀.

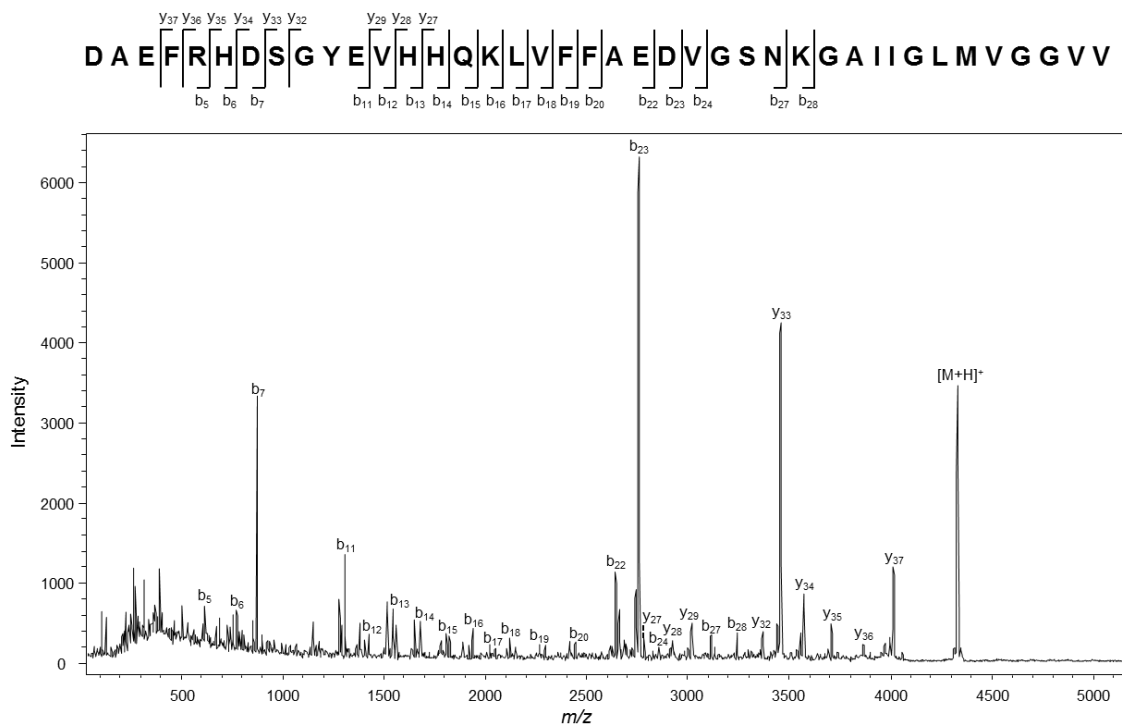


Figure 4.4. MS/MS spectrum obtained for m/z 4,329 with the peptides identified in the spectrum. The entire peptide sequence for A β ₄₀ is shown above the spectrum. These data confirmed the presence of A β ₄₀ within the 5XFAD brains.

The sequence identified using MS/MS and BioTools was searched in the Mascot database. The full protein identified from this sequence was human A β A4 protein. The peptide score for A β ₄₀ was 232 with an expectation value of 1.3E-18 confirming the identity of the peptide in the 5XFAD brain sections.

These data indicate PMZ was retained within the brains of 5XFAD mice and not in brains of wildtype mice. The amount of PMZ detected in the 5XFAD mouse brains was nearly three-fold

higher than that detected in the wildtype. Furthermore, PMZ was detected within the brain in similar regions as A β ₄₀. Along with the lysate studies, these data indicate PMZ could potentially be utilized as PET scanning probe for A β to detect the progression of Alzheimer's disease in patients.

Quantitative MALDI IMS of Promethazine in Liver Tissue Sections

Methods for microspotted quantitative MALDI IMS of liver tissue sections were established in Chapter III.¹ These methods were further validated using liver tissues from mice dosed with PMZ. As previously described, an established mouse model (5XFAD) was utilized to demonstrate the A β -binding ability of PMZ as a potential PET scan contrast agent.^{15, 60} PMZ was detected in the brains of 5XFAD transgenic mice, and nearly three-fold less was detected in the brains of wildtype mice; PMZ was retained in the 5XFAD mice brains and eliminated quickly from the wildtype mice brains.

Prior to performing any quantitative IMS experiments depositing calibration standards with the acoustic robotic spotter (Portrait 630, Labcyte, Sunnyvale, CA), the volume deposited by the instrument was measured for 50% methanol/water as was performed with 50% ethanol/water for the RIF measurements.¹ The droplet volume of the robotic spotter was measured using a fluorescence assay. To perform these assays, 50 passes of 100 droplets (5,000 total droplets) of 0.100 mg/mL fluorescein in 50% methanol/water were deposited into six different wells of a 96-well plate. The droplets were allowed to dry and reconstituted in 100 μ L of 10 μ M tris-buffered saline (pH=9). Calibration standards (100 μ L of 0.100-1.50 μ g/mL) were pipetted into separate wells for comparison. The fluorescence was measured at a wavelength of 514 nm after excitation at 490 nm using a plate reader (SpectraMax M2^e, Molecular Devices, Sunnyvale,

CA). The fluorescence responses from the different wells were compared to the manually pipetted calibration curve to determine the droplet size. This experiment was repeated twice, and the average droplet size was determined to be 169.7 ± 5.1 pL/droplet from these measurements.

One 5XFAD transgenic mouse and one wildtype mouse were administered 25 mg/kg PMZ five times via tail vein injections. Another wildtype mouse was administered phosphate-buffered saline as a control. The livers and kidneys were resected four hours post-injection, flash-frozen, and stored at -80°C until analysis. The control and two dosed livers were cryosectioned ($12\ \mu\text{m}$ thick), and the sections were thaw-mounted onto a gold-coated stainless steel MALDI target. Calibration standards of PMZ ($1.00\text{-}20.0\ \mu\text{M}$ PMZ with $15.0\ \mu\text{M}$ $^2\text{H}_3\text{-PMZ}$) were deposited onto the non-dosed tissue section using the acoustic robotic spotter. A quality control (QC) solution ($7.50\ \mu\text{M}$ PMZ with $15.0\ \mu\text{M}$ $^2\text{H}_3\text{-PMZ}$) was also deposited onto the non-dosed tissue section. The two dosed tissue sections were prepared by applying $15\ \mu\text{M}$ $^2\text{H}_3\text{-PMZ}$ in a $350 \times 350\ \mu\text{m}$ array across each section. After applying the calibration and internal standards, matrix ($30\ \text{mg/mL}$ DHB in 50% methanol/water with 0.1% trifluoroacetic acid) was applied using the robotic spotter. The matrix and the standards were applied using 20 passes of 2 droplets (169.7 ± 5.1 pL/droplet) with 60 seconds between each pass to allow for drying.

Using a MALDI LTQ XL, a total of 13 analytical scans with 3 microscans of 5 laser shots each were collected for each microspot to average the signal throughout the entire area ($200\ \mu\text{m}$ diameter circle). The precursor ions for PMZ and $^2\text{H}_3\text{-PMZ}$ were selected in a large isolation window ($m/z\ 286.6 \pm 3.0$) and fragmented using a normalized collision energy of 27%. The total amount of PMZ deposited is known, since the robotic spotter delivers 169.7 ± 5.1 pL/droplet.

The density of liver tissue is assumed to be equal to that of water (1.05 g/mL),^{10, 61} and the diameter of the microspots was measured to be $204.8 \pm 7.7 \mu\text{m}$ (n=8). A cylinder of tissue (12 μm tall with a diameter of 200 μm) was used to calculate the tissue's mass for each microspot to compare to HPLC-MS/MS.

Calibration curves were generated by plotting the average intensity area ratio of the major fragment ion of PMZ to the intensity area of the major fragment ion of $^2\text{H}_3\text{-PMZ}$ [m/z 86/ m/z 89] versus the concentration of PMZ applied to the tissue section (8 microspots for each concentration). The intensity area ratios were generated using MALDIQuan software (Thermo Scientific). The quantitative MALDI MS/MS images were generated with in-house software developed in MATLAB. The software generates a color map with an array of circles 200 μm in diameter representing the concentration in $\mu\text{g PMZ/g}$ tissue detected from each microspot. This color map is overlaid onto the optical image taken of the target after matrix application. The minimum concentration displayed in the quantitative images represents the lowest point on the calibration curve for the experiments. This experiment was performed in triplicate on different sections from the same liver tissues.

The spectra for PMZ and $^2\text{H}_3\text{-PMZ}$ with DHB as the matrix and for DHB alone spotted onto a control liver tissue section yielded no biological or matrix interferences in the analysis (Figure 4.5). The primary fragment ions for PMZ are m/z 86, 198, and 240. The only fragment ion of $^2\text{H}_3\text{-PMZ}$ containing the deuterated isotopic label is m/z 89, corresponding to fragmentation at the phenothiazine nitrogen-carbon bond (Figure 4.5). The spectrum for the matrix alone indicates no biological or matrix ions interfering with the analysis of PMZ or the internal standard in liver tissue.

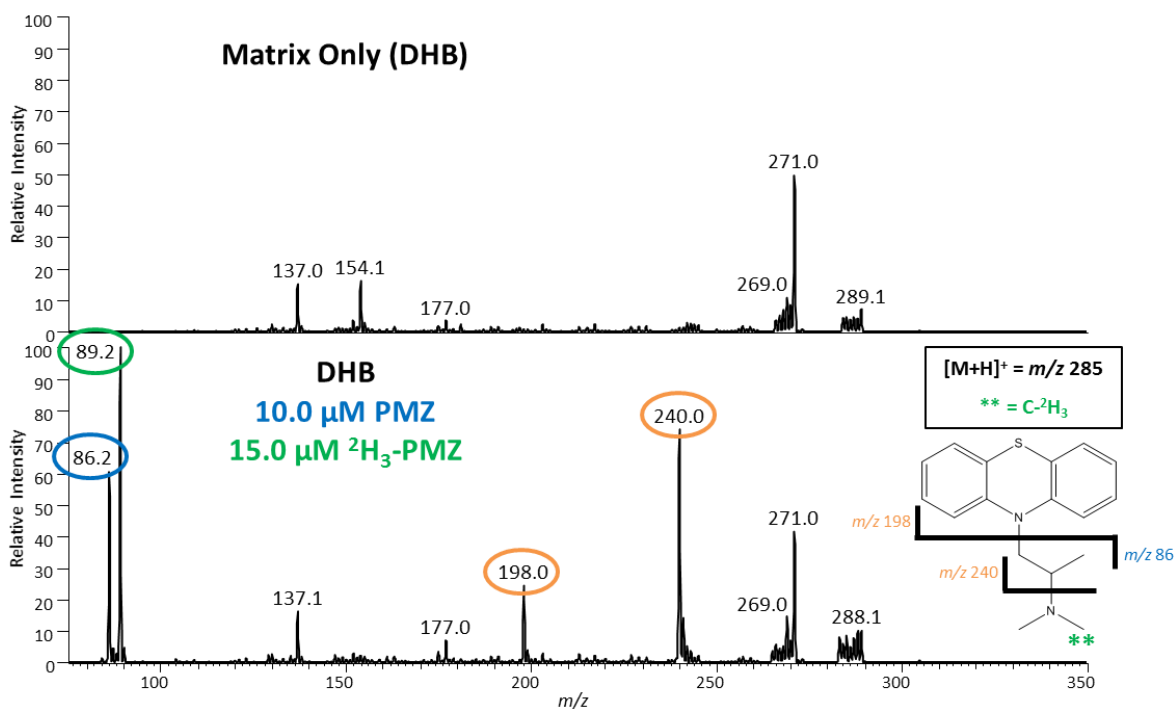


Figure 4.5. Product ion spectra isolating and fragmenting m/z 286.6 \pm 3.0 of DHB alone and a calibration standard of PMZ deposited onto a non-dosed liver tissue section. The major fragments for PMZ (m/z 86) and $^2\text{H}_3$ -PMZ (m/z 89) are circled in blue and green, respectively, and represent the fragmentation at the phenothiazine nitrogen-carbon bond. The other two fragments circled in orange (m/z 198 and 240) are shared for both analytes.

The generated calibration curves (Figure 4.6A) were nearly identical for three different trials within a three week span. All quality control microspots were greater than 85% accurate with most greater than 95%. The quantitative MALDI MS/MS images for PMZ analyzed at a spatial resolution of 350 μm of the two dosed livers (Figure 4.6B) reveal the absolute quantitative distribution of PMZ. Each microspot within the images represents the concentration of PMZ detected in μg PMZ/g tissue. Little to no PMZ was detected in the blood vessels of either liver section (outlined in black), likely because it is bound to proteins within the blood such as albumin.⁶² Furthermore, after averaging the amounts detected in each liver, 65.1 \pm 9.6 μg

PMZ/g tissue were detected in the 5XFAD mouse liver, and $26.8 \pm 1.4 \mu\text{g PMZ/g tissue}$ were detected in the wildtype liver (Table 4.1).

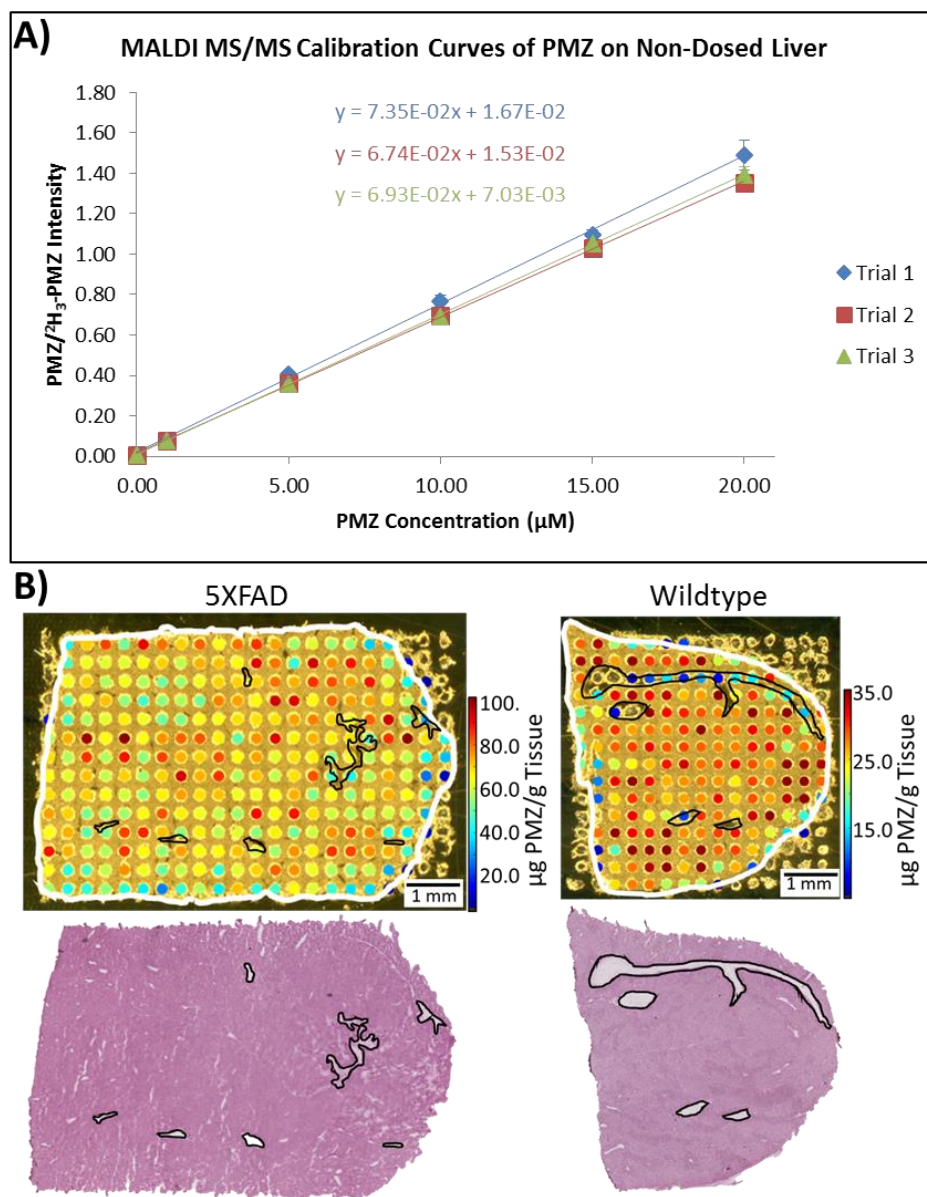


Figure 4.6. The calibration curves (A) for three trials of quantitative MALDI IMS from a non-dosed liver section and the quantitative MALDI images with their respective H&E stained serial sections (B) demonstrating the distribution of PMZ throughout liver sections of a 5XFAD mouse (left) and a wildtype mouse (right). The error bars represent the standard deviation of 8 microspots for each concentration. The microspots in the MALDI image represent the detected amount of PMZ. Blood vessels are outlined in black on the image and the H&E stains.

These data were further verified after homogenizing the same tissue sections and analyzing for PMZ concentration using HPLC-MS/MS. The dosed liver tissues and a control liver tissue were cut (~65 mg), homogenized in 10% methanol/water (~25 mg/mL), and analyzed similar to a previously published method.^{1, 63, 64} Stock solutions of PMZ (0.449 mg/mL) and ²H₃-PMZ (0.397 mg/mL) were used to spike calibration standards (1.12E-2 to 2.25 µg PMZ with 1.98E-1 µg ²H₃-PMZ) into 150 µL of the control liver homogenate. Only the internal standard was spiked into 150 µL of the dosed tissue homogenates. All samples were diluted with methanol to a final volume of 800 µL and were centrifuged at 10,000 RPM for ten minutes. The supernatants of the tissue homogenates were separated by reversed phase liquid chromatography using a C18 column (30 × 2 mm, Luna 3 µm, 100 Å; Phenomenex, Torrance, CA) and analyzed on a triple quadrupole MS/MS instrument (Agilent 6430, Santa Clara, CA). The solvents used for the HPLC separation were 0.1% formic acid in water (A) and methanol (B). The gradient linearly decreased from 90% to 10% solvent A over 5 minutes, held for 1 minute, linearly increased to 90% solvent A in one minute, and held for three more minutes. The transitions of *m/z* 285 to 86 (PMZ) and *m/z* 288 to 89 (²H₃-PMZ) were monitored with the retention times at approximately 3.9 minutes. The calibration curves for three trials of HPLC-MS/MS analysis (Figure 4.3) were nearly identical.

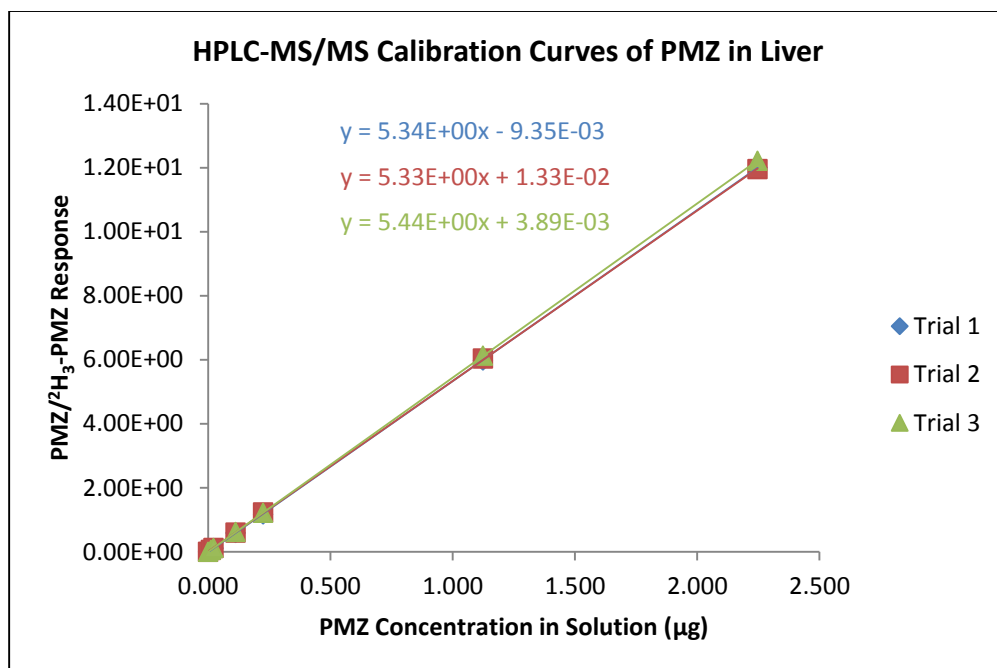


Figure 4.7. The calibration curves of PMZ spiked into control liver homogenates and analyzed by HPLC-MS/MS were nearly identical for three trials.

The responses from the dosed tissue extracts were compared to the calibration curve to determine the amount of PMZ detected from the dosed liver tissues. The amounts detected by HPLC-MS/MS were $65.4 \pm 5.3 \mu\text{g PMZ/g tissue}$ in the 5XFAD mouse liver and $25.0 \pm 1.6 \mu\text{g PMZ/g tissue}$ in the wildtype liver (Table 4.1). When comparing the average concentrations detected using MALDI IMS and HPLC-MS/MS, they were 99.6% and 92.9% similar for the 5XFAD and the wildtype livers, respectively. These concentration values obtained from three trials of each methodology were not statistically significantly different when performing a t-test with 95% confidence (p-value = 0.99 and 0.22, respectively).

Liver Tissue Concentration ($\mu\text{g PMZ/g Tissue}$)		
	HPLC-MS/MS	MALDI IMS
5XFAD	65.4 \pm 5.3	65.1 \pm 9.6
Wildtype	25.0 \pm 1.6	26.8 \pm 1.4

Table 4.1. Concentrations of PMZ detected in the 5XFAD and wildtype livers by HPLC-MS/MS and MALDI IMS. More PMZ was detected in the 5XFAD liver than in the wildtype liver. The similarity between HPLC-MS/MS and MALDI IMS quantitation of the 5XFAD liver and the wildtype liver were 99.6 and 92.9 percent, respectively.

Based upon previous studies examining the pharmacokinetics of PMZ, the pharmaceutical drug undergoes first-pass liver metabolism by the cytochrome P450 enzyme CYP2D6 when injected with over half of the initial blood concentration metabolized within four hours.^{65, 66} The higher concentration detected in the 5XFAD mouse liver is likely caused by PMZ retention by A β in the brain allowing PMZ to remain in the mouse's system. Furthermore, PMZ does not permanently bind to A β in 5XFAD mouse brains when analyzed by HPLC coupled to ultraviolet spectroscopy.¹⁵ Nearly 2% of the initial dose was retained in the brain 10 minutes post-dose while 0.5% remained four hours post-dose. Within a wildtype brain under the same conditions, 0.5% of the initial dose was retained in the brain after 10 minutes while 0.01% remained after four hours.¹⁵ Therefore, it is likely PMZ was metabolized later in the 5XFAD livers than in the wildtype liver, leading to a higher concentration of PMZ detected four hours post-dose in the 5XFAD liver.

These data further validated the methods of quantitative MALDI IMS using a different pharmaceutical in liver tissue. The similarities between the MALDI IMS and HPLC-MS/MS

analyses were quite high (greater than 92.9%). However, the quantitative MALDI IMS data revealed the spatial localization of PMZ in the liver tissue section, which was lost during the homogenization process required for HPLC-MS/MS analysis.

MALDI MS/MS of Calibration Standards Applied to Different Tissue Types

Before performing quantitative MALDI IMS on tissues containing multiple cell types within a single section, the ability of the internal standard to account for ionization efficiency and extraction differences among tissue types was investigated to determine if the calibration curves generated from them were equivalent. An internal standard can account for ionization and extraction differences between the white and grey matter in the brain according to the literature, but no conclusions have been made with respect to other tissue types, and they have not been analyzed on the microspotted size regime.⁷

To perform these experiments, 12 μm thick tissue sections of control rat liver, kidney, brain, and heart (Pel-Freez Biologicals, Rogers, AR) were thaw-mounted onto a gold-coated stainless steel target. PMZ calibration standards (5.00-75.0 μM PMZ with 20.0 μM $^2\text{H}_3$ -PMZ) were deposited onto each tissue section using the robotic spotter; they were deposited onto the liver, cortex of the kidney, medulla of the kidney, brain, and heart. A QC solution (25.0 μM PMZ with 20.0 μM $^2\text{H}_3$ -PMZ) was also deposited onto the different tissue types. After the standards were deposited onto the sections, matrix (20 mg/mL DHB in 50% methanol/water with 0.1% trifluoroacetic acid) was deposited onto each calibration standard microspot. Eight microspots were averaged for each concentration to construct the calibration curve for each tissue type. The calibration microspots were analyzed using the same method as previously performed to analyze the liver sections with a MALDI LTQ XL. A total of 13 analytical scans with 3 microscans

of 5 laser shots each were collected for each microspot to average the signal throughout the area (200 μm diameter circle). The precursor ions for the analyte and the internal standard were selected in a single isolation window (m/z 286.6 ± 3.0) and fragmented using a normalized collision energy of 27%.

The average detected $^2\text{H}_3$ -PMZ intensities for each calibration microspot on each tissue type are shown in Figure 4.8. For each tissue type, the average detected intensities of the internal standard remains consistent among all concentrations of PMZ. However, there is a pattern with respect to the detected intensity based upon the tissue type. The $^2\text{H}_3$ -PMZ intensities detected from the liver are consistently higher for each concentration than those from the other tissue types. Furthermore, the $^2\text{H}_3$ -PMZ intensities detected from the medulla of the kidney are consistently lower than those detected from the other tissue types, including the cortex of kidney.

To determine if there were any statistically significant differences among the detected $^2\text{H}_3$ -PMZ intensities for the different tissue types, an analysis of variance (ANOVA) was performed for each calibration standard concentration (Tables 4.2-4.6). The computed F statistics were 27.7 (p-value = $2.05\text{E-}10$), 13.3 (p-value = $1.09\text{E-}6$), 14.8 (p-value = $3.58\text{E-}7$), 12.6 (p-value = $1.82\text{E-}6$), and 4.52 (p-value = $4.76\text{E-}3$) for the 5.00, 10.0, 20.0, 40.0, and 75.0 μM calibration standards, respectively. These data indicate there were statistically significant differences amongst the detected $^2\text{H}_3$ -PMZ intensities from the tissue types at the 0.05 significance level.

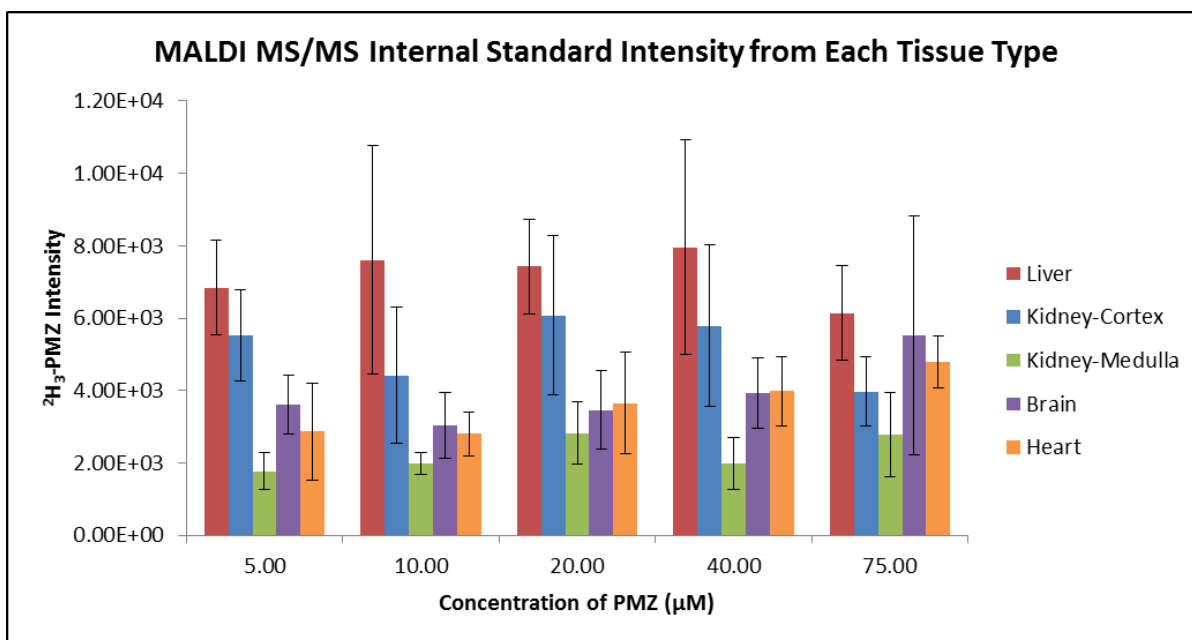


Figure 4.8. Detected average internal standard (²H₃-PMZ) intensities from each calibration standard on each tissue type. The error bars represent the standard deviation of 8 microspots.

ANOVA - 5.00 μM					
	Sum of Squares	df	Mean Square	F	p-value
Between Groups	1.34E+08	4	3.35E+07	27.7	2.05E-10
Within Groups	4.24E+07	35	1.21E+06		
Total	1.77E+08	39			

Table 4.2. Analysis of variance (ANOVA) for the intensities of ²H₃-PMZ detected from the 5.00 μM calibration standard on each tissue type.

ANOVA - 10.0 μM					
	Sum of Squares	df	Mean Square	F	p-value
Between Groups	1.57E+08	4	3.94E+07	13.3	1.09E-06
Within Groups	1.04E+08	35	2.96E+06		
Total	2.61E+08	39			

Table 4.3. Analysis of variance (ANOVA) for the intensities of ²H₃-PMZ detected from the 10.0 μM calibration standard on each tissue type.

ANOVA - 20.0 μM					
	Sum of Squares	df	Mean Square	F	p-value
Between Groups	1.24E+08	4	3.10E+07	14.8	3.58E-07
Within Groups	7.32E+07	35	2.09E+06		
Total	1.97E+08	39			

Table 4.4. Analysis of variance (ANOVA) for the intensities of $^2\text{H}_3\text{-PMZ}$ detected from the 20.0 μM calibration standard on each tissue type.

ANOVA - 40.0 μM					
	Sum of Squares	df	Mean Square	F	p-value
Between Groups	1.63E+08	4	4.08E+07	12.6	1.82E-06
Within Groups	1.13E+08	35	3.23E+06		
Total	2.76E+08	39			

Table 4.5. Analysis of variance (ANOVA) for the intensities of $^2\text{H}_3\text{-PMZ}$ detected from the 40.0 μM calibration standard on each tissue type.

ANOVA - 75.0 μM					
	Sum of Squares	df	Mean Square	F	p-value
Between Groups	5.55E+07	4	1.39E+07	4.52	4.76E-03
Within Groups	1.07E+08	35	3.07E+06		
Total	1.63E+08	39			

Table 4.6. Analysis of variance (ANOVA) for the intensities of $^2\text{H}_3\text{-PMZ}$ detected from the 75.0 μM calibration standard on each tissue type.

To determine which tissue types yielded statistically significant differences in the amount of the internal standard detected, post hoc Tukey tests were performed for each concentration (Tables 4.7-4.11). The 5.00 μM standard yielded statistically significant differences in the detected intensities between the liver and the medulla (p-value = 6.47E-10), the liver and the brain (p-value = 1.01E-5), the liver and the heart (p-value = 1.93E-7), the cortex and the medulla

(p-value = 6.12E-7), the cortex and the brain (p-value = 1.07E-2), the cortex and the heart (p-value = 2.54E-4), and the medulla and the brain (p-value = 1.62E-2). The 10.0 μM standard yielded statistically significant differences in the detected intensities between the liver and cortex (p-value = 6.06E-3), the liver and medulla (p-value = 1.42E-6), the liver and the brain (p-value = 5.65E-5), and the liver and the heart (p-value = 2.51E-5). The 20.0 μM standard yielded statistically significant differences between the liver and the medulla (p-value = 2.45E-6), the liver and the brain (p-value = 3.42E-5), the liver and the heart (p-value = 7.59E-5), the cortex and the medulla (p-value = 6.73E-4), the cortex and the brain (p-value = 7.88E-3), and the cortex and the heart (p-value = 1.58E-2). The 40.0 μM standard yielded statistically significant differences between the liver and the medulla (p-value = 9.77E-7), the liver and brain (p-value = 6.84E-4), the liver and the heart (7.78E-4), and the cortex and the medulla (p-value = 1.31E-3). Finally, the 75.0 μM calibration standard yielded statistically significant differences between the liver and the medulla (4.45E-3) and the medulla and the brain (p-value = 2.71E-2). No statistically significant differences were detected between the medulla and the heart or the brain and the heart for any of the calibration standards. These data indicate there are differences in extraction and/or ionization of analytes from different tissue types, including those within the same tissue (cortex and medulla).

Multiple Comparisons - 5.00 μM						
Tukey Test for Differences in $^2\text{H}_3\text{-PMZ}$ Intensity						
(I) TissueType	(J) Tissue Type	Mean Difference (I-J)	Std. Error	p-value	95% Confidence Interval	
					Lower Bound	Upper Bound
Liver	Kidney-Cortex	1.32E+03	5.50E+02	1.39E-01	-2.61E+02	2.90E+03
	Kidney-Medulla*	5.08E+03	5.50E+02	6.47E-10	3.50E+03	6.66E+03
	Brain*	3.24E+03	5.50E+02	1.01E-05	1.66E+03	4.83E+03
	Heart*	3.97E+03	5.50E+02	1.93E-07	2.39E+03	5.55E+03
Kidney-Cortex	Liver	-1.32E+03	5.50E+02	1.39E-01	-2.90E+03	2.61E+02
	Kidney-Medulla*	3.76E+03	5.50E+02	6.12E-07	2.18E+03	5.34E+03
	Brain*	1.92E+03	5.50E+02	1.07E-02	3.41E+02	3.51E+03
	Heart*	2.65E+03	5.50E+02	2.54E-04	1.07E+03	4.23E+03
Kidney-Medulla	Liver*	-5.08E+03	5.50E+02	6.47E-10	-6.66E+03	-3.50E+03
	Kidney-Cortex*	-3.76E+03	5.50E+02	6.12E-07	-5.34E+03	-2.18E+03
	Brain*	-1.84E+03	5.50E+02	1.62E-02	-3.42E+03	-2.53E+02
	Heart	-1.11E+03	5.50E+02	2.82E-01	-2.69E+03	4.75E+02
Brain	Liver*	-3.24E+03	5.50E+02	1.01E-05	-4.83E+03	-1.66E+03
	Kidney-Cortex*	-1.92E+03	5.50E+02	1.07E-02	-3.51E+03	-3.41E+02
	Kidney-Medulla*	1.84E+03	5.50E+02	1.62E-02	2.53E+02	3.42E+03
	Heart	7.28E+02	5.50E+02	6.79E-01	-8.54E+02	2.31E+03
Heart	Liver*	-3.97E+03	5.50E+02	1.93E-07	-5.55E+03	-2.39E+03
	Kidney-Cortex*	-2.65E+03	5.50E+02	2.54E-04	-4.23E+03	-1.07E+03
	Kidney-Medulla	1.11E+03	5.50E+02	2.82E-01	-4.75E+02	2.69E+03
	Brain	-7.28E+02	5.50E+02	6.79E-01	-2.31E+03	8.54E+02

* on the (J) Tissue Type indicates the mean difference is significant at the 0.05 level.

Table 4.7. Post hoc Tukey test for differences in detected $^2\text{H}_3\text{-PMZ}$ intensities from the 5.00 μM calibration standard on each tissue type.

Multiple Comparisons - 10.0 μM						
Tukey Test for Differences in $^2\text{H}_3\text{-PMZ}$ Intensity						
(I) TissueType	(J) Tissue Type	Mean Difference (I-J)	Std. Error	p-value	95% Confidence Interval	
					Lower Bound	Upper Bound
Liver	Kidney-Cortex*	3.19E+03	8.60E+02	6.06E-03	7.17E+02	5.66E+03
	Kidney-Medulla*	5.63E+03	8.60E+02	1.42E-06	3.16E+03	8.11E+03
	Brain*	4.58E+03	8.60E+02	5.65E-05	2.11E+03	7.05E+03
	Heart*	4.81E+03	8.60E+02	2.51E-05	2.34E+03	7.29E+03
Kidney-Cortex	Liver*	-3.19E+03	8.60E+02	6.06E-03	-5.66E+03	-7.17E+02
	Kidney-Medulla	2.44E+03	8.60E+02	5.43E-02	-3.08E+01	4.92E+03
	Brain	1.39E+03	8.60E+02	4.99E-01	-1.08E+03	3.86E+03
	Heart	1.62E+03	8.60E+02	3.44E-01	-8.52E+02	4.09E+03
Kidney-Medulla	Liver*	-5.63E+03	8.60E+02	1.42E-06	-8.11E+03	-3.16E+03
	Kidney-Cortex	-2.44E+03	8.60E+02	5.43E-02	-4.92E+03	3.08E+01
	Brain	-1.05E+03	8.60E+02	7.37E-01	-3.53E+03	1.42E+03
	Heart	-8.21E+02	8.60E+02	8.73E-01	-3.29E+03	1.65E+03
Brain	Liver*	-4.58E+03	8.60E+02	5.65E-05	-7.05E+03	-2.11E+03
	Kidney-Cortex	-1.39E+03	8.60E+02	4.99E-01	-3.86E+03	1.08E+03
	Kidney-Medulla	1.05E+03	8.60E+02	7.37E-01	-1.42E+03	3.53E+03
	Heart	2.32E+02	8.60E+02	9.99E-01	-2.24E+03	2.71E+03
Heart	Liver*	-4.81E+03	8.60E+02	2.51E-05	-7.29E+03	-2.34E+03
	Kidney-Cortex	-1.62E+03	8.60E+02	3.44E-01	-4.09E+03	8.52E+02
	Kidney-Medulla	8.21E+02	8.60E+02	8.73E-01	-1.65E+03	3.29E+03
	Brain	-2.32E+02	8.60E+02	9.99E-01	-2.71E+03	2.24E+03

* on the (J) Tissue Type indicates the mean difference is significant at the 0.05 level.

Table 4.8. Post hoc Tukey test for differences in detected $^2\text{H}_3\text{-PMZ}$ intensities from the 10.0 μM calibration standard on each tissue type.

Multiple Comparisons - 20.0 µM						
Tukey Test for Differences in ² H ₃ -PMZ Intensity						
(I) TissueType	(J) Tissue Type	Mean Difference (I-J)	Std. Error	p-value	95% Confidence Interval	
					Lower Bound	Upper Bound
Liver	Kidney-Cortex	1.36E+03	7.23E+02	3.47E-01	-7.20E+02	3.44E+03
	Kidney-Medulla*	4.60E+03	7.23E+02	2.45E-06	2.53E+03	6.68E+03
	Brain*	3.97E+03	7.23E+02	3.42E-05	1.89E+03	6.05E+03
	Heart*	3.78E+03	7.23E+02	7.59E-05	1.70E+03	5.86E+03
Kidney-Cortex	Liver	-1.36E+03	7.23E+02	3.47E-01	-3.44E+03	7.20E+02
	Kidney-Medulla*	3.25E+03	7.23E+02	6.73E-04	1.17E+03	5.32E+03
	Brain*	2.61E+03	7.23E+02	7.88E-03	5.32E+02	4.69E+03
	Heart*	2.42E+03	7.23E+02	1.58E-02	3.40E+02	4.50E+03
Kidney-Medulla	Liver*	-4.60E+03	7.23E+02	2.45E-06	-6.68E+03	-2.53E+03
	Kidney-Cortex*	-3.25E+03	7.23E+02	6.73E-04	-5.32E+03	-1.17E+03
	Brain	-6.34E+02	7.23E+02	9.04E-01	-2.71E+03	1.45E+03
	Heart	-8.26E+02	7.23E+02	7.83E-01	-2.91E+03	1.25E+03
Brain	Liver*	-3.97E+03	7.23E+02	3.42E-05	-6.05E+03	-1.89E+03
	Kidney-Cortex*	-2.61E+03	7.23E+02	7.88E-03	-4.69E+03	-5.32E+02
	Kidney-Medulla	6.34E+02	7.23E+02	9.04E-01	-1.45E+03	2.71E+03
	Heart	-1.92E+02	7.23E+02	9.99E-01	-2.27E+03	1.89E+03
Heart	Liver*	-3.78E+03	7.23E+02	7.59E-05	-5.86E+03	-1.70E+03
	Kidney-Cortex*	-2.42E+03	7.23E+02	1.58E-02	-4.50E+03	-3.40E+02
	Kidney-Medulla	8.26E+02	7.23E+02	7.83E-01	-1.25E+03	2.91E+03
	Brain	1.92E+02	7.23E+02	9.99E-01	-1.89E+03	2.27E+03

* on the (J) Tissue Type indicates the mean difference is significant at the 0.05 level.

Table 4.9. Post hoc Tukey test for differences in detected ²H₃-PMZ intensities from the 20.0 µM calibration standard on each tissue type.

Multiple Comparisons - 40.0 μM						
Tukey Test for Differences in $^2\text{H}_3\text{-PMZ}$ Intensity						
(I) TissueType	(J) Tissue Type	Mean Difference (I-J)	Std. Error	p-value	95% Confidence Interval	
					Lower Bound	Upper Bound
Liver	Kidney-Cortex	2.17E+03	8.98E+02	1.35E-01	-4.13E+02	4.75E+03
	Kidney-Medulla*	5.99E+03	8.98E+02	9.77E-07	3.41E+03	8.58E+03
	Brain*	4.03E+03	8.98E+02	6.84E-04	1.44E+03	6.61E+03
	Heart*	3.99E+03	8.98E+02	7.78E-04	1.40E+03	6.57E+03
Kidney-Cortex	Liver	-2.17E+03	8.98E+02	1.35E-01	-4.75E+03	4.13E+02
	Kidney-Medulla*	3.82E+03	8.98E+02	1.31E-03	1.24E+03	6.41E+03
	Brain	1.86E+03	8.98E+02	2.57E-01	-7.26E+02	4.44E+03
	Heart	1.82E+03	8.98E+02	2.77E-01	-7.66E+02	4.40E+03
Kidney-Medulla	Liver*	-5.99E+03	8.98E+02	9.77E-07	-8.58E+03	-3.41E+03
	Kidney-Cortex*	-3.82E+03	8.98E+02	1.31E-03	-6.41E+03	-1.24E+03
	Brain	-1.97E+03	8.98E+02	2.07E-01	-4.55E+03	6.14E+02
	Heart	-2.01E+03	8.98E+02	1.91E-01	-4.59E+03	5.74E+02
Brain	Liver*	-4.03E+03	8.98E+02	6.84E-04	-6.61E+03	-1.44E+03
	Kidney-Cortex	-1.86E+03	8.98E+02	2.57E-01	-4.44E+03	7.26E+02
	Kidney-Medulla	1.97E+03	8.98E+02	2.07E-01	-6.14E+02	4.55E+03
	Heart	-3.96E+01	8.98E+02	1.00E+00	-2.62E+03	2.54E+03
Heart	Liver*	-3.99E+03	8.98E+02	7.78E-04	-6.57E+03	-1.40E+03
	Kidney-Cortex	-1.82E+03	8.98E+02	2.77E-01	-4.40E+03	7.66E+02
	Kidney-Medulla	2.01E+03	8.98E+02	1.91E-01	-5.74E+02	4.59E+03
	Brain	3.96E+01	8.98E+02	1.00E+00	-2.54E+03	2.62E+03

* on the (J) Tissue Type indicates the mean difference is significant at the 0.05 level.

Table 4.10. Post hoc Tukey test for differences in detected $^2\text{H}_3\text{-PMZ}$ intensities from the 40.0 μM calibration standard on each tissue type.

Multiple Comparisons - 75.0 μM						
Tukey Test for Differences in $^2\text{H}_3\text{-PMZ}$ Intensity						
(I) TissueType	(J) Tissue Type	Mean Difference (I-J)	Std. Error	p-value	95% Confidence Interval	
					Lower Bound	Upper Bound
Liver	Kidney-Cortex	2.17E+03	8.76E+02	1.19E-01	-3.47E+02	4.69E+03
	Kidney-Medulla*	3.35E+03	8.76E+02	4.45E-03	8.30E+02	5.87E+03
	Brain	6.06E+02	8.76E+02	9.57E-01	-1.91E+03	3.12E+03
	Heart	1.36E+03	8.76E+02	5.39E-01	-1.16E+03	3.88E+03
Kidney-Cortex	Liver	-2.17E+03	8.76E+02	1.19E-01	-4.69E+03	3.47E+02
	Kidney-Medulla	1.18E+03	8.76E+02	6.67E-01	-1.34E+03	3.70E+03
	Brain	-1.57E+03	8.76E+02	3.96E-01	-4.09E+03	9.52E+02
	Heart	-8.15E+02	8.76E+02	8.83E-01	-3.33E+03	1.70E+03
Kidney-Medulla	Liver*	-3.35E+03	8.76E+02	4.45E-03	-5.87E+03	-8.30E+02
	Kidney-Cortex	-1.18E+03	8.76E+02	6.67E-01	-3.70E+03	1.34E+03
	Brain*	-2.74E+03	8.76E+02	2.71E-02	-5.26E+03	-2.24E+02
	Heart	-1.99E+03	8.76E+02	1.78E-01	-4.51E+03	5.27E+02
Brain	Liver	-6.06E+02	8.76E+02	9.57E-01	-3.12E+03	1.91E+03
	Kidney-Cortex	1.57E+03	8.76E+02	3.96E-01	-9.52E+02	4.09E+03
	Kidney-Medulla*	2.74E+03	8.76E+02	2.71E-02	2.24E+02	5.26E+03
	Heart	7.52E+02	8.76E+02	9.10E-01	-1.77E+03	3.27E+03
Heart	Liver	-1.36E+03	8.76E+02	5.39E-01	-3.88E+03	1.16E+03
	Kidney-Cortex	8.15E+02	8.76E+02	8.83E-01	-1.70E+03	3.33E+03
	Kidney-Medulla	1.99E+03	8.76E+02	1.78E-01	-5.27E+02	4.51E+03
	Brain	-7.52E+02	8.76E+02	9.10E-01	-3.27E+03	1.77E+03

* on the (J) Tissue Type indicates the mean difference is significant at the 0.05 level.

Table 4.11. Post hoc Tukey test for differences in detected $^2\text{H}_3\text{-PMZ}$ intensities from the 75.0 μM calibration standard on each tissue type.

Though the detected $^2\text{H}_3\text{-PMZ}$ intensities were different among the tissue types, the calibration curves were expected to be similar, because the internal standard and the calibration standard are chemically analogous and should be extracted, ionized, and analyzed similarly. The generated calibration curves from each tissue type are shown in Figure 4.9. The internal standard accounts for the extraction or ionization efficiency differences caused by the different tissues to produce identical calibration curves. Additionally, the QC solutions were

greater than 93.3% accurate for each tissue type. The average for the accuracy on all tissue types was 98.9%.

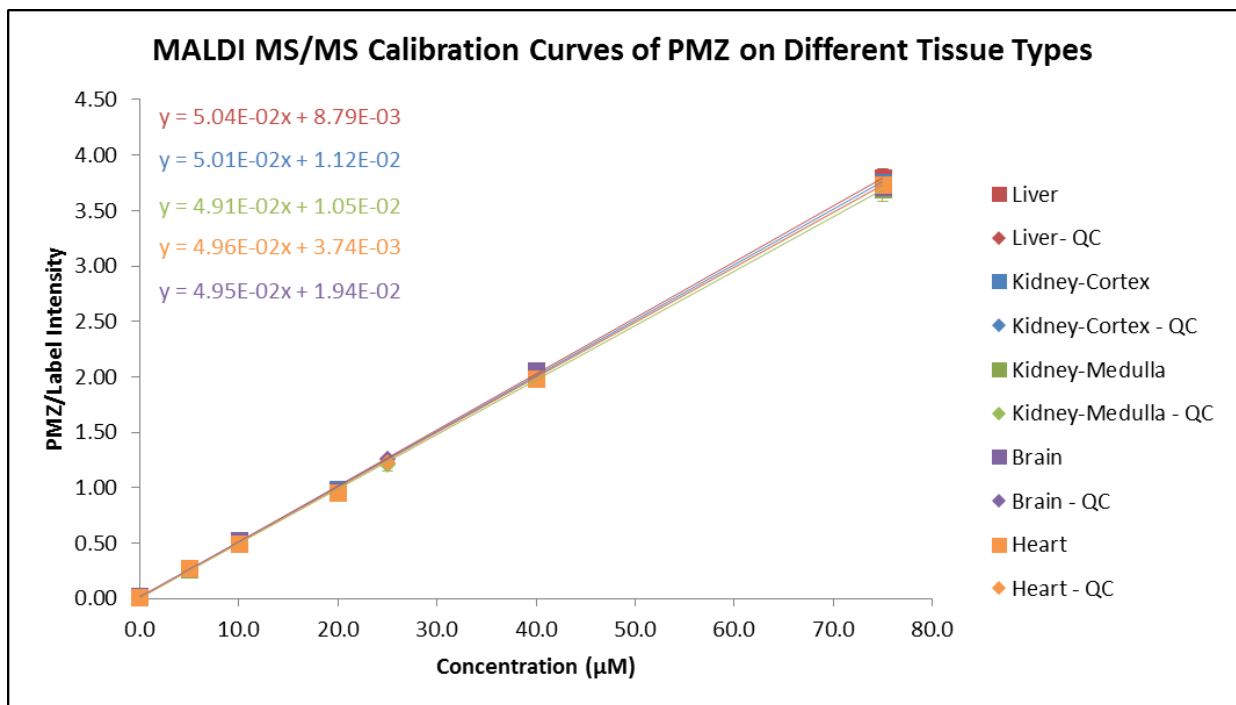


Figure 4.9. Calibration curves of PMZ detected from each tissue type using MALDI MS/MS. They are very similar to one another with the QC solutions depicted as a diamond with each microspot exhibiting greater than 93.3% accuracy. The error bars represent the standard deviation of 8 microspots.

Based upon the nearly identical calibration curves from two different trials ($F = 0.53, 5.62, 1.45, 1.98, 1.56,$ and 2.22 for $5.00, 10.0, 20.0, 40.0,$ and $75.0 \mu\text{M}$, respectively; $p\text{-value} > 0.05$ except for $F = 5.62$ where $p\text{-value} = 0.001$), a single calibration curve could potentially be applied if analyzing a heterogeneous tissue. The only statistically significant difference detected was from the $10.0 \mu\text{M}$ solution in which the responses from the heart tissue were statistically significantly different from the responses from the liver ($p\text{-value} = 0.008$), medulla

(p-value = 0.001), and brain (p-value = 0.003) tissues. The standard deviation of the responses from the heart tissue at this concentration was lower than that from the other concentrations, yielding the statistically significant differences at this concentration. Furthermore, the errors in the y-intercepts and slopes yielded 95% confidence intervals that overlapped for all intercepts and for all slopes except for the liver (5.00E-2 to 5.08E-2) and the medulla (4.85E-2 to 4.97E-2).

Though the calibration curves were nearly identical, there may be differences in the limits of quantitation among the different tissue types depending on the extraction and ionization efficiency. A separate experiment determining the limits of quantitation was performed by measuring the response of a wide range of PMZ calibration standards (0.0500-200. μM PMZ with 20.0 μM $^2\text{H}_3$ -PMZ) deposited onto each tissue type. Eight replicates were analyzed to determine the lowest and highest concentrations with less than 20% precision around and a mean ten-fold higher than the blank response.⁶⁷ The lowest and highest concentrations of PMZ meeting these criteria were 3.00 μM and 150. μM for the liver, 5.00 μM and 200. μM for the cortex, 3.00 μM and 200. μM for the medulla, 3.00 μM and 150. μM for the brain, and 3.00 μM and 150. μM for the heart. These data indicate a single calibration curve could potentially be used, but the limits of quantitation must be evaluated for each tissue type.

Quantitative MALDI IMS of Promethazine in Kidney Tissue Sections

Kidneys from one 5XFAD transgenic mouse and one wildtype mouse administered 25 mg/kg PMZ five times via tail vein injections were analyzed for their quantitative PMZ distribution. A wildtype mouse administered the vehicle as a control was used for the calibration standards. The kidneys were resected with the previously analyzed livers four hours post-injection, flash-frozen, and stored at -80°C until analysis. The control and two dosed kidneys were

cryosectioned (12 μm thick) and thaw-mounted onto a gold-coated stainless steel MALDI target. Calibration standards of PMZ (5.00-75.0 μM PMZ with 20.0 μM $^2\text{H}_3\text{-PMZ}$) were applied using the robotic spotter to the non-dosed tissue section. A QC solution (25.0 μM PMZ with 20.0 μM $^2\text{H}_3\text{-PMZ}$) was also deposited onto the non-dosed tissue section. The two dosed tissue sections were prepared by applying 20.0 μM $^2\text{H}_3\text{-PMZ}$ in an array with a spatial resolution of 350 μm across each section. After applying the calibration and internal standards, matrix (30 mg/mL DHB in 50% methanol/water with 0.1% trifluoroacetic acid) was applied to all of the microspots. The matrix and the standards were applied using 20 passes of 2 droplets (169.7 ± 5.1 pL/droplet) with 60 seconds between each pass to allow for drying.

The kidney sections were analyzed using a MALDI LTQ XL with the same method as previously performed to analyze the liver tissue sections. A total of 13 analytical scans with 3 microscans of 5 laser shots each were collected for each microspot to average the signal throughout the area (200 μm diameter circle). The precursor ions for the analyte and the internal standard were selected in a single isolation window (m/z 286.6 ± 3.0) and fragmented using a normalized collision energy of 27%. The quantitative MALDI MS/MS images were generated with in-house software developed using MATLAB. This experiment was performed in triplicate on different sections from the same kidney tissues.

The spectra for PMZ and $^2\text{H}_3\text{-PMZ}$ with DHB as the matrix and for DHB alone spotted onto a control kidney tissue section provided no biological or matrix interferences in the analysis (Figure 4.10). The primary fragment ions for PMZ are m/z 86, 198, and 240. The only fragment ion of $^2\text{H}_3\text{-PMZ}$ containing the deuterated isotopic label is m/z 89, corresponding to fragmentation at the phenothiazine nitrogen-carbon bond (Figure 4.10). The spectrum for the

matrix alone indicates no biological or matrix ions interfering with the analysis of PMZ or $^2\text{H}_3$ -PMZ from kidney tissues.

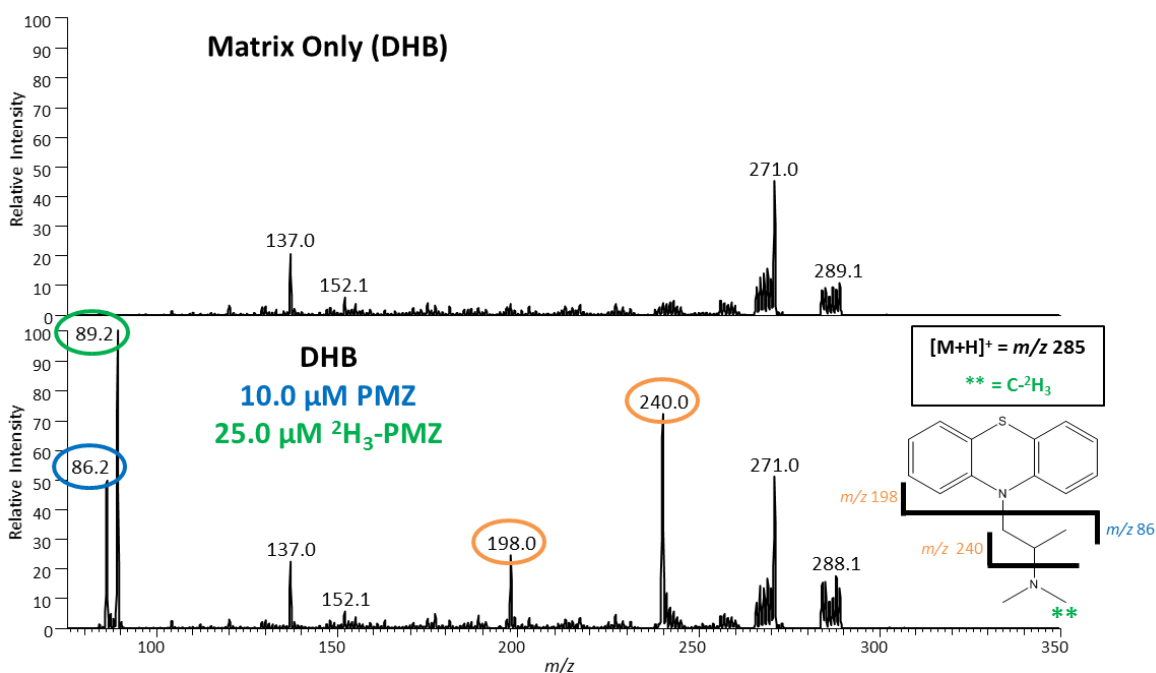


Figure 4.10. Product ion spectra isolating and fragmenting $m/z\ 286.6 \pm 3.0$ of DHB alone and a calibration standard of PMZ deposited onto a non-dosed kidney tissue section. The major fragments for PMZ ($m/z\ 86$) and $^2\text{H}_3$ -PMZ ($m/z\ 89$) are circled in blue and green, respectively, and represent the fragmentation at the phenothiazine nitrogen-carbon bond. The other two fragments circled in orange ($m/z\ 198$ and 240) are shared for both analytes.

As expected from the experiments analyzing calibration curves on different tissue types, the calibration curves generated on the cortex and medulla were nearly identical with slopes of $4.86\text{E}-2 \pm 4.22\text{E}-4$ and $4.79\text{E}-2 \pm 4.79\text{E}-4$, respectively (Figure 4.11A). Furthermore, the errors in the slopes and the y-intercepts overlapped with one another indicating the two curves were equivalent. The localization of PMZ throughout the 5XFAD and wildtype kidneys is very similar (Figure 4.11B). More PMZ was localized in the cortex of the kidneys, with very little PMZ

detected in the medulla. Higher concentrations detected in the renal cortex is consistent with its primary function of ultrafiltration, in which small molecules are filtered out of the blood within the kidney. Because most of this occurs in the glomeruli within the cortex, less PMZ was expected from the medulla as previously shown with other pharmaceutical drugs.^{5, 68} Additionally, $69.7 \pm 2.4 \mu\text{g PMZ/g}$ tissue were detected in the 5XFAD kidney, and $43.9 \pm 1.0 \mu\text{g PMZ/g}$ tissue were detected in the wildtype kidney (Table 4.12). This is consistent with the previous results in the liver where more PMZ was detected in the 5XFAD mouse than in the wildtype mouse.

The distribution of PMZ in a dosed mouse kidney was further validated using MALDI IMS at an improved spatial resolution. The other kidney from the 5XFAD mouse dosed with PMZ was cryosectioned, and the $12 \mu\text{m}$ thick sections were thaw-mounted onto a gold-coated stainless steel target. The section was manually coated with 30 mg/mL DHB and analyzed using a MALDI LTQ XL at a spatial resolution of $75 \mu\text{m}$. The precursor ion for PMZ ($m/z 285.1 \pm 0.5$) was isolated and fragmented using a normalized collision energy of 27%. The MALDI MS/MS image was generated by plotting the intensity of the primary PMZ fragment ion $m/z 86$.

As demonstrated in the MALDI MS/MS image (Figure 4.12), PMZ is localized to the cortex of the kidney. Very little PMZ is detected in the medulla region. In particular, more PMZ is detected in the inner cortex of the kidney. This is consistent with the quantitative MALDI MS/MS image (Figure 4.11B) collected from the 5XFAD kidney dosed with PMZ.

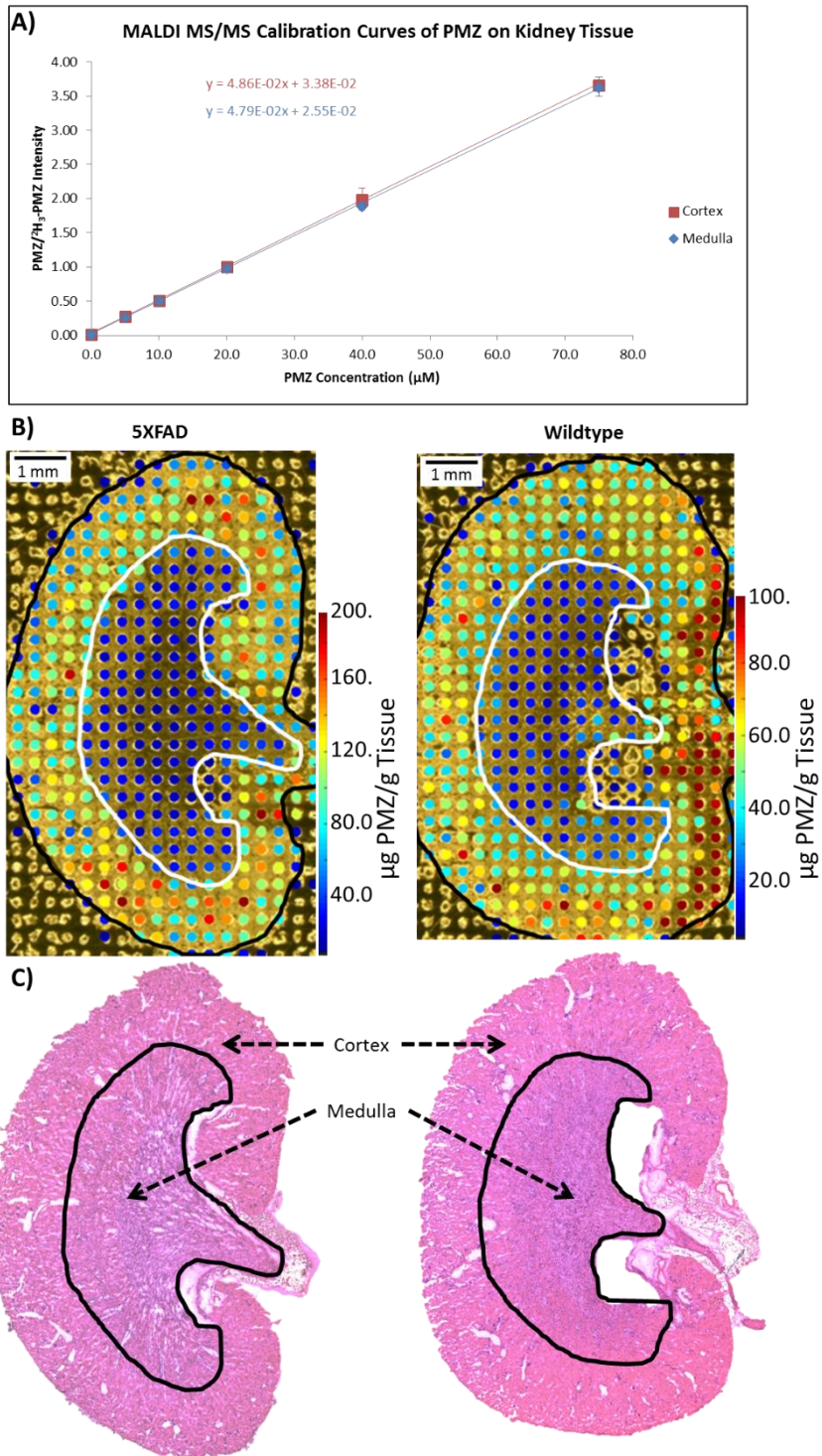


Figure 4.11. MALDI MS/MS calibration curves of PMZ (A) on the medulla and cortex of a control kidney section. Quantitative MALDI MS/MS images of PMZ (B) and H&E stained serial sections (C) of kidneys from a 5XFAD and a wildtype mouse dosed *in vivo*. Each microspot in the MALDI MS/MS images represents the detected amount of PMZ. The medulla is outlined in white in the images and in black in the stained sections. More PMZ is localized to the cortex of the kidneys.

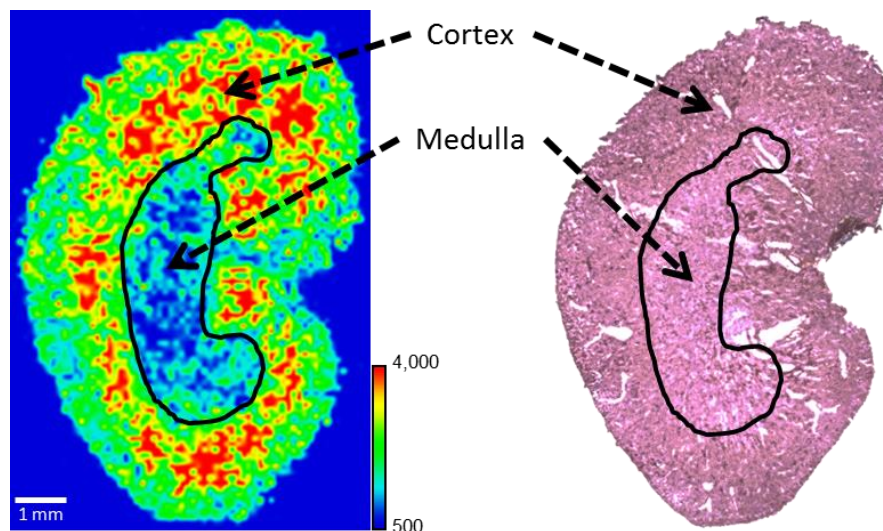


Figure 4.12. MALDI IMS of PMZ (m/z 86) detected from a dosed kidney section. The tissue was analyzed using MALDI MS/MS at a spatial resolution of 75 μm .

To further validate the quantitative measurements, the dosed kidney tissues and a control kidney tissue were cut (~ 75 mg), homogenized in 10% methanol/water (~ 30 mg/mL), and analyzed as previously described.⁶³ The dosed kidneys were cut immediately following the MALDI IMS analyses to ensure similar amounts of the medulla and cortex were present in the HPLC-MS/MS samples and in the MALDI IMS sections. Stock solutions of PMZ (0.449 mg/mL) and $^2\text{H}_3$ -PMZ (0.397 mg/mL) were used to spike calibration standards (1.12E-2 to 2.25 μg PMZ with 1.98E-1 μg $^2\text{H}_3$ -PMZ) into 150 μL of the control liver homogenate. Only the internal standard was spiked into 150 μL of the dosed tissue homogenates. The transitions of m/z 285 to 86 (PMZ) and m/z 288 to 89 ($^2\text{H}_3$ -PMZ) were monitored with the retention times at approximately 3.9 minutes. The calibration curves for three trials of HPLC-MS/MS analysis were nearly identical with the slopes ranging from 5.11 to 5.39 (Figure 4.13).

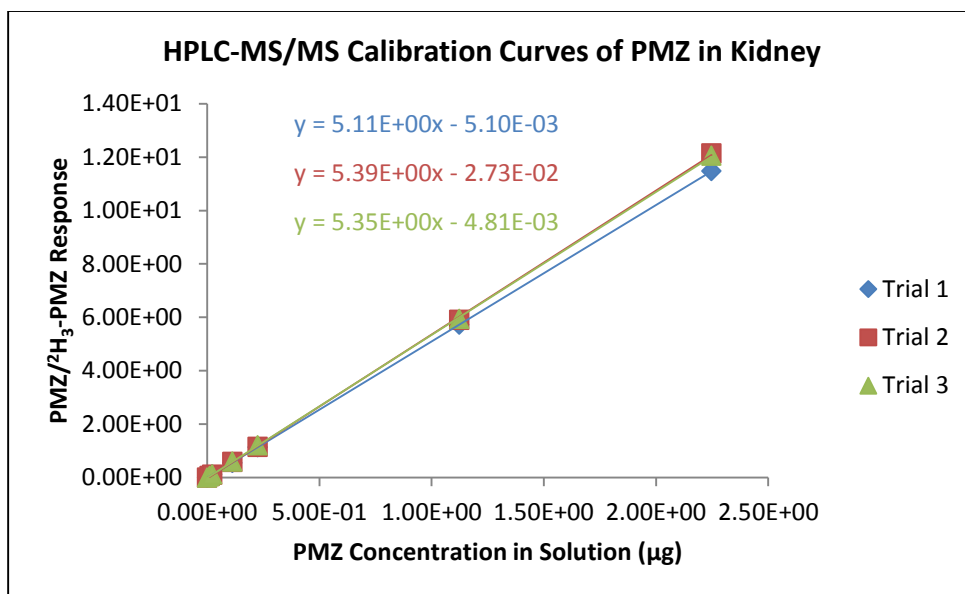


Figure 4.13. Calibration curves of PMZ spiked into control kidney homogenates and analyzed by HPLC-MS/MS.

The responses from the dosed tissue extracts were compared to the calibration curve to determine the amount of PMZ detected from the dosed kidney tissues. The amounts detected by HPLC-MS/MS were $69.3 \pm 1.1 \mu\text{g PMZ/g tissue}$ in the 5XFAD kidney and $40.9 \pm 2.3 \mu\text{g PMZ/g tissue}$ in the wildtype kidney (Table 4.12). When comparing the average concentrations detected using MALDI IMS and HPLC-MS/MS, they were 99.4% and 93.4% similar for the 5XFAD and the wildtype kidneys, respectively. These concentration values obtained from three trials of each methodology were not statistically significantly different when performing a t-test with 95% confidence (p-value = 0.81 and 0.11, respectively).

Kidney Tissue Concentration ($\mu\text{g PMZ/g Tissue}$)		
	HPLC-MS/MS	MALDI IMS
5XFAD	69.3 \pm 1.1	69.7 \pm 2.4
Wildtype	40.9 \pm 2.3	43.9 \pm 1.0

Table 4.12. Concentrations of PMZ detected in the 5XFAD and wildtype kidneys by HPLC-MS/MS and MALDI IMS. As with the livers, more PMZ was detected in the 5XFAD kidney than in the wildtype kidney. The similarity between HPLC-MS/MS and MALDI IMS quantitation of the 5XFAD and wildtype kidneys were 99.4 and 93.4 percent, respectively.

As previously mentioned with the liver analyses and based upon previous studies examining the pharmacokinetics of PMZ, the pharmaceutical drug undergoes first-pass liver metabolism by the cytochrome P450 enzyme CYP2D6 when injected with over half of the initial blood concentration metabolized within four hours.^{65, 66} Similar to the amounts detected in the livers, the higher concentration detected in the 5XFAD mouse kidney is likely caused by PMZ retention by A β in the brain, allowing it to remain in the mouse's system. Therefore, it is likely PMZ was metabolized later in the 5XFAD kidney than in the wildtype kidney, leading to a higher concentration of PMZ detected four hours post-dose in the 5XFAD kidney. Quantitative MALDI IMS provided the quantitative localization of PMZ within the kidney, demonstrating a higher concentration in the cortex than in the medulla. These data were confirmed by homogenization and analysis by HPLC-MS/MS, but the localization was only revealed by MALDI IMS.

Conclusions

Microspotted quantitative MALDI IMS provides the absolute quantitative distribution of a pharmaceutical drug within a thin tissue section. These data provide an example in which quantitative MALDI IMS was used to elucidate the distribution of a more hydrophobic drug, PMZ, in the livers of dosed mice. Furthermore, the technology was used to provide the absolute quantitative localization of the drug in a heterogeneous tissue, the kidney, of the same dosed mice. The analyses indicated more PMZ was present in the dosed livers and kidneys of the 5XFAD mouse than in those of the wildtype mouse. This is likely because the drug remained bound to A β in the brain of the 5XFAD mouse, delaying its metabolism in the liver and kidneys.

The quantitative MALDI IMS results indicate very little PMZ was detected from the blood vessels within the livers of either mouse, likely because it was bound to albumin within the blood. Furthermore, more PMZ was detected in the cortexes of the kidneys from both mice than in the medullas as expected based upon renal functionality. The quantitative MALDI IMS data from the tissues were further validated with HPLC-MS/MS. The similarities between the MALDI IMS and HPLC-MS/MS analyses of the livers and kidneys were quite high (greater than 92.9%). However, the quantitative MALDI IMS data revealed the spatial localization of PMZ in the sections, which was lost during the homogenization process required for HPLC-MS/MS analysis.

References

1. C. W. Chumbley, M. L. Reyzer, J. L. Allen, G. A. Marriner, L. E. Via, C. E. Barry III and R. M. Caprioli, *Analytical Chemistry*, 2016, **88**, 2292-2398.
2. K. Shrivastava, T. Hayasaka, N. Goto-Inoue, Y. Sugiura, N. Zaima and M. Setou, *Analytical Chemistry*, 2010, **82**, 8800-8806.

3. N. R. Katz, *Journal of Nutrition*, 1992, **122**, 843-849.
4. K. J. Grove, P. A. Voziyan, J. M. Spraggins, S. Wang, P. Paueksakon, R. C. Harris, B. G. Hudson and R. M. Caprioli, *Journal of Lipid Research*, 2014, **55**, 1375-1385.
5. M. R. Groseclose, S. B. Laffan, K. S. Frazier, A. Hughes-Earle and S. Castellino, *Journal of the American Society for Mass Spectrometry*, 2015, **26**, 887-898.
6. J. M. Spraggins, D. G. Rizzo, J. L. Moore, K. L. Rose, N. D. Hammer, E. P. Skaar and R. M. Caprioli, *Journal of the American Society for Mass Spectrometry*, 2015, **26**, 974-985.
7. D. A. Pirman, A. Kiss, R. M. A. Heeren and R. A. Yost, *Analytical Chemistry*, 2013, **85**, 1090-1096.
8. D. A. Pirman and R. A. Yost, *Analytical Chemistry*, 2011, **83**, 8575-8581.
9. G. Hamm, D. Bonnel, R. Legouffe, F. Pamelard, J. Delbos, F. Bouzom and J. Stauber, *Journal of Proteomics*, 2012, **75**, 4952-4961.
10. D. A. Pirman, R. F. Reich, A. Kiss, R. M. A. Heeren and R. A. Yost, *Analytical Chemistry*, 2013, **85**, 1081-1089.
11. M. R. Groseclose and S. Castellino, *Analytical Chemistry*, 2013, **85**, 10099-10106.
12. T. Porta, A. Lesur, E. Varesio and G. Hopfgartner, *Analytical and Bioanalytical Chemistry*, 2015, **407**, 2177-2187.
13. D. A. Pirman, *Bioanalysis*, 2015, **7**, 2649-2656.
14. D. S. Wishart, C. Knox, A. C. Guo, D. Cheng, S. Shrivastava, D. Tzur, B. Gautam and M. Hassanali, *Nucleic Acids Research*, 2008, **36**, D901-D906.
15. R. A. McClure, C. W. Chumbley, M. L. Reyzer, K. Wilson, R. M. Caprioli, J. C. Gore and W. Pham, *Neuroimage-Clinical*, 2013, **2**, 620-629.
16. M. Hintersteiner, A. Enz, P. Frey, A. L. Jatou, W. Kinzy, R. Kneuer, U. Neumann, M. Rudin, M. Staufenbiel, M. Stoeckli, K. H. Wiederhold and H. U. Gremlich, *Nature Biotechnology*, 2005, **23**, 577-583.
17. J. Hort, J. T. O'Brien, G. Gainotti, T. Pirttila, B. O. Popescu, I. Rektorova, S. Sorbi and P. Scheltens, *European Journal of Neurology*, 2010, **17**, 1236-1248.
18. S. Sorbi, J. Hort, T. Erkinjuntti, T. Fladby, G. Gainotti, H. Gurvit, B. Nacmias, F. Pasquier, B. O. Popescu, I. Rektorova, D. Religa, R. Rusina, M. Rossor, R. Schmidt, E. Stefanova, J. D. Warren and P. Scheltens, *European Journal of Neurology*, 2012, **19**, 1159-1179.
19. R. C. Petersen, R. Doody, A. Kurz, R. C. Mohs, J. C. Morris, P. V. Rabins, K. Ritchie, M. Rossor, L. Thal and B. Winblad, *Archives of Neurology*, 2001, **58**, 1985-1992.
20. J. Hardy and D. J. Selkoe, *Science*, 2002, **297**, 353-356.
21. S. Artero, M. C. Tierney, J. Touchon and K. Ritchie, *Acta Psychiatrica Scandinavica*, 2003, **107**, 390-393.
22. R. L. Van Heertum and R. S. Tikofsky, *Seminars in Nuclear Medicine*, 2003, **33**, 77-85.
23. K. Ritchie, M. Ancelin, E. Beaino, F. Portet, A. M. Brickman, J. Dartigues, C. Tzourio, A. Dupuy, C. W. Ritchie, C. Berr and S. Artero, *American Journal of Geriatric Psychiatry*, 2010, **18**, 692-700.
24. M. S. Albert, S. T. DeKosky, D. Dickson, B. Dubois, H. H. Feldman, N. C. Fox, A. Gamst, D. M. Holtzman, W. J. Jagust, R. C. Petersen, P. J. Snyder, M. C. Carrillo, B. Thies and C. H. Phelps, *Alzheimers & Dementia*, 2011, **7**, 270-279.
25. S. M. Landau, M. A. Mintun, A. D. Joshi, R. A. Koeppe, R. C. Petersen, P. S. Aisen, M. W. Weiner and W. J. Jagust, *Annals of Neurology*, 2012, **72**, 578-586.

26. H. Braak and E. Braak, *Neurobiology of Aging*, 1995, **16**, 271-278.
27. G. Merlini and V. Bellotti, *New England Journal of Medicine*, 2003, **349**, 583-596.
28. P. T. Lansbury, Jr., *Nature Medicine*, 2004, S51-S57.
29. R. N. Rosenberg, *Archives of General Psychiatry*, 2005, **62**, 1186-1192.
30. J. Delrieu, P. J. Ousset, C. Caillaud and B. Vellas, *Journal of Neurochemistry*, 2012, **120**, 186-193.
31. P. S. Aisen and B. Vellas, *Journal of Nutrition Health & Aging*, 2013, **17**, 49-50.
32. B. J. Cummings and C. W. Cotman, *Lancet*, 1995, **346**, 1524-1528.
33. B. J. Cummings, C. J. Pike, R. Shankle and C. W. Cotman, *Neurobiology of Aging*, 1996, **17**, 921-933.
34. R. J. Perrin, A. M. Fagan and D. M. Holtzman, *Nature*, 2009, **461**, 916-922.
35. L. C. de Souza, S. Lehericy, B. Dubois, F. Stella and M. Sarazin, *Current Opinion in Psychiatry*, 2012, **25**, 473-479.
36. S. L. Risacher and A. J. Saykin, *Annual Review of Clinical Psychology*, Vol 9, 2013, **9**, 621-648.
37. J. D. D'Amore, S. T. Kajdasz, M. E. McLellan, B. J. Bacskai, E. A. Stern and B. T. Hyman, *Journal of Neuropathology and Experimental Neurology*, 2003, **62**, 137-145.
38. C. R. Jack, R. C. Petersen, Y. C. Xu, P. C. O'Brien, G. E. Smith, R. J. Ivnik, B. F. Boeve, S. C. Waring, E. G. Tangalos and E. Kokmen, *Neurology*, 1999, **52**, 1397-1403.
39. P. N. Wang, J. F. Lirng, K. N. Lin, F. C. Chang and H. C. Liu, *Neurobiology of Aging*, 2006, **27**, 1797-1806.
40. D. Yanagisawa, T. Amatsubo, S. Morikawa, H. Taguchi, M. Urushitani, N. Shirai, K. Hirao, A. Shiino, T. Inubushi and I. Tooyama, *Neuroscience*, 2011, **184**, 120-127.
41. G. A. Kerchner, *Journal of Alzheimers Disease*, 2011, **26**, 91-95.
42. R. M. Koffie, C. T. Farrar, L. Saidi, C. M. William, B. T. Hyman and T. L. Spires-Jones, *Proceedings of the National Academy of Sciences of the United States of America*, 2011, **108**, 18837-18842.
43. A. D. Cohen, G. D. Rabinovici, C. A. Mathis, W. J. Jagust, W. E. Klunk and M. D. Ikonovic, *Current State of Alzheimer's Disease Research and Therapeutics*, 2012, **64**, 27-81.
44. M. D. Ikonovic, E. E. Abrahamson, J. C. Price, R. L. Hamilton, C. A. Mathis, W. R. Paljug, M. L. Debnath, A. D. Cohen, K. Mizukami, S. T. DeKosky, O. L. Lopez and W. E. Klunk, *Acta Neuropathologica*, 2012, **123**, 433-447.
45. G. J. O'Keefe, T. H. Saunderson, S. Ng, U. Ackerman, H. J. Tochon-Danguy, J. G. Chan, S. Gong, T. Dyrks, S. Lindemann, G. Holl, L. Dinkelborg, V. Villemagne and C. C. Rowe, *Journal of Nuclear Medicine*, 2009, **50**, 309-315.
46. S. R. Choi, G. Golding, Z. Zhuang, W. Zhang, N. Lim, F. Hefti, T. E. Beneditum, M. R. Kilbourn, D. Skovronsky and H. F. Kung, *Journal of Nuclear Medicine*, 2009, **50**, 1887-1894.
47. V. L. Villemagne, K. Ong, R. S. Mulligan, G. Holl, S. Pejoska, G. Jones, G. O'Keefe, U. Ackerman, H. Tochon-Danguy, J. G. Chan, C. B. Reininger, L. Fels, B. Putz, B. Rohde, C. L. Masters and C. C. Rowe, *Journal of Nuclear Medicine*, 2011, **52**, 1210-1217.
48. W. E. Klunk, H. Engler, A. Nordberg, Y. M. Wang, G. Blomqvist, D. P. Holt, M. Bergstrom, I. Savitcheva, G. F. Huang, S. Estrada, B. Ausen, M. L. Debnath, J. Barletta, J. C. Price, J.

- Sandell, B. J. Lopresti, A. Wall, P. Koivisto, G. Antoni, C. A. Mathis and B. Langstrom, *Annals of Neurology*, 2004, **55**, 306-319.
49. M. A. Mintun, G. N. LaRossa, Y. I. Sheline, C. S. Dence, S. Y. Lee, R. H. Mach, W. E. Klunk, C. A. Mathis, S. T. DeKosky and J. C. Morris, *Neurology*, 2006, **67**, 446-452.
50. W. E. Klunk, J. C. Price, C. A. Mathis, N. D. Tsopelas, B. J. Lopresti, S. K. Ziolkow, W. Bi, J. A. Hoge, A. D. Cohen, M. D. Ikonovic, J. A. Saxton, B. E. Snitz, D. A. Pollen, M. Moonis, C. F. Lippa, J. M. Swearer, K. A. Johnson, D. M. Rentz, A. J. Fischman, H. J. Aizenstein and S. T. DeKosky, *Journal of Neuroscience*, 2007, **27**, 6174-6184.
51. C. A. Mathis, N. S. Mason, B. J. Lopresti and W. E. Klunk, *Seminars in Nuclear Medicine*, 2012, **42**, 423-432.
52. E. H. Seeley and R. M. Caprioli, *Proceedings of the National Academy of Sciences of the United States of America*, 2008, **105**, 18126-18131.
53. D. D. Nolting, J. C. Gore and W. Pham, *Current Organic Synthesis*, 2011, **8**, 521-534.
54. E. E. Nesterov, J. Skoch, B. T. Hyman, W. E. Klunk, B. J. Bacskai and T. M. Swager, *Angewandte Chemie-International Edition*, 2005, **44**, 5452-5456.
55. H. Levine, *Protein Science*, 1993, **2**, 404-410.
56. S. A. Hudson, H. Ecroyd, T. W. Kee and J. A. Carver, *Febs Journal*, 2009, **276**, 5960-5972.
57. W. M. A. Niessen, *Mass Spectrometry Reviews*, 2011, **30**, 626-663.
58. M. Stoeckli, D. Staab, M. Staufienbiel, K. Wiederhold and L. Signor, *Analytical Biochemistry*, 2002, **311**, 33-39.
59. M. Stoeckli, D. Staab, A. Schweitzer, J. Gardiner and D. Seebach, *Journal of the American Society for Mass Spectrometry*, 2007, **18**, 1921-1924.
60. H. Oakley, S. L. Cole, S. Logan, E. Maus, P. Shao, J. Craft, A. Guillozet-Bongaarts, M. Ohno, J. Disterhoft, L. Van Eldik, R. Berry and R. Vassar, *Journal of Neuroscience*, 2006, **26**, 10129-10140.
61. R. F. Reich, K. Cudzilo, J. A. Levisky and R. A. Yost, *Journal of the American Society for Mass Spectrometry*, 2010, **21**, 564-571.
62. A. B. Khan, J. M. Khan, M. S. Ali, R. H. Khan and K. U. Din, *Colloids and Surfaces B-Biointerfaces*, 2011, **87**, 447-453.
63. P. F. Fang, H. L. Cai, H. D. Li, R. H. Zhu, Q. Y. Tan, W. Gao, P. Xu, Y. P. Liu, W. Y. Zhang, Y. C. Chen and F. Zhang, *Journal of Chromatography B-Analytical Technologies in the Biomedical and Life Sciences*, 2010, **878**, 2286-2291.
64. G. Taylor and J. B. Houston, *Journal of Chromatography*, 1982, **230**, 194-198.
65. G. Taylor, J. B. Houston, J. Shaffer and G. Mawer, *British Journal of Clinical Pharmacology*, 1983, **15**, 287-293.
66. K. Nakamura, T. Yokoi, K. Inoue, N. Shimada, N. Ohashi, T. Kume and T. Kamataki, *Pharmacogenetics*, 1996, **6**, 449-457.
67. T. A. Little, *Biopharm International*, 2015, **28**, 48-51.
68. A. Nilsson, R. J. A. Goodwin, J. G. Swales, R. Gallagher, H. Shankaran, A. Sathe, S. Pradeepan, A. Xue, N. Keirstead, J. C. Sasaki, P. E. Andren and A. Gupta, *Chemical Research in Toxicology*, 2015, **28**, 1823-1830.

CHAPTER V

CONCLUSIONS AND PERSPECTIVES

High-Throughput MALDI MS/MS Imaging of Pharmaceutical Drugs

Continuous laser raster sampling has been previously explored to improve the throughput of matrix-assisted laser desorption/ionization (MALDI) mass spectrometers.^{1, 2} In Chapter II, a high-speed continuous laser raster sampling MALDI time-of-flight/time-of-flight (TOF/TOF) mass spectrometer was used to improve the throughput of MALDI tandem mass spectrometry (MS/MS) imaging experiments. The use of continuous laser raster sampling on a MALDI TOF/TOF system improves the throughput ~8-10 fold compared to an ion trap or a non-continuous sampling TOF/TOF system, resulting in overall effective pixel and spectral acquisition rates of up to 10 Hz and 1,000 Hz, respectively.³ MS/MS is particularly important when analyzing small molecules, including pharmaceutical drugs, where other isobaric species may complicate spectral and image interpretation.

As demonstrated in Chapter II, MS/MS improved the molecular specificity and sensitivity of the resulting MS/MS ion image of rifampicin (RIF) in a liver dosed *in vivo*, and continuous laser raster sampling dramatically reduced the analysis time. As MALDI imaging mass spectrometry (IMS) analyses are extended to improved spatial resolutions and larger tissue areas, throughput becomes an important analytical figure of merit. Coupled with the benefits of MS/MS methodology such as improved sensitivity and chemical specificity, continuous laser raster

sampling on a MALDI TOF/TOF mass spectrometer offers a higher throughput method capable of imaging larger datasets.

Quantitative Multiplexed MALDI MS/MS of Pharmaceutical Drugs in Plasma

A quantitative pharmaceutical drug assay for enalapril was also developed using a MALDI TOF/TOF mass spectrometer in Chapter II. The instrument has the capability of not only continuous laser raster sampling, but also isolating and fragmenting multiple precursor ions within the same laser shot, thereby multiplexing MS/MS analyses. This capability was first used to demonstrate the improvements in quantitative accuracy and reproducibility by using a structurally similar pharmaceutical drug as the internal standard. A quantitative assay of enalapril from human plasma was performed utilizing ramipril as the internal standard. While the two drugs differ in a pyrrolidine versus a cyclopentapyrrole moiety, they yield identical dominant fragment ions. The precision of the analysis improved nearly four-fold after normalizing to the internal standard. The linearity and the accuracy also improved upon normalization spanning a range of 2.5 orders of magnitude that included the therapeutic range.

Furthermore, a multiplexed quantitative assay was developed for the analysis of promethazine, enalapril, and verapamil in a single MALDI MS/MS analysis of human plasma. Isotopically labeled internal standards for each pharmaceutical drug were used as the internal standard. Each pharmaceutical drug and its internal standard were isolated and fragmented together. Therefore, there were three different isolation windows analyzed on each laser shot. As with the enalapril experiments, normalization to their respective internal standard improved the precision of the analysis. While the lower limits of quantitation for these pharmaceutical drugs were higher than the individual enalapril analysis, the toxic levels fall within the range of

this analysis.⁴⁻⁸ Additionally, these data provide a proof of principle for the quantitative MALDI TOF/TOF analysis of multiple analytes in a single laser shot.

Quantitative MALDI IMS of Pharmaceutical Drugs in Thin Tissue Sections

Classic approaches to pharmaceutical drug quantitation, such as quantitative whole body autoradiography (QWBA) and high performance liquid chromatography-mass spectrometry (HPLC-MS), provide complementary quantitative information about a potential therapeutic. However, microspotted pixel-to-pixel quantitative MALDI imaging mass spectrometry (IMS) combines the benefits of both technologies into a single analysis.⁹ It provides both spatial and molecular specificity in obtaining an absolute amount of a pharmaceutical drug present within a thin tissue section.

In Chapter III, different methods for depositing isotopically labeled internal standards for MALDI IMS were analyzed on a homogenous standard tissue dosed *in vitro* with rifampicin (RIF). The standard tissue allowed for accuracy comparisons between MALDI IMS data from thin tissue sections and HPLC-MS results from tissue extracts of the same tissue. Depositing the internal standard onto the tissue section followed sequentially by matrix deposition yielded the most accurate results when compared to HPLC-MS/MS.

The quantitative distributions of two different pharmaceutical drugs, RIF in Chapter III and promethazine (PMZ) in Chapter IV, were elucidated in the livers of animals dosed *in vivo*. Low concentrations of both pharmaceutical drugs were detected in the blood vessels within the tissue sections. This was likely caused by the pharmaceutical drugs being bound to a protein, such as albumin, within the blood. Furthermore, utilizing calibration microspots equivalent in size to the microspots on the dosed tissue section allowed for quality control (QC) validations of

the method. These QC microspots were deposited and analyzed in the same manner as the calibration microspots and those from the dosed tissue sections allowing for the accuracy and precision to be assessed in every quantitative MALDI IMS experiment.

Furthermore, quantitative MALDI IMS experiments were performed using two different mass analyzers, a linear ion trap mass spectrometer and a high-speed time-of-flight/time-of-flight (TOF/TOF) mass spectrometer, in Chapter III. Both analyzers yielded concentrations similar to HPLC-MS/MS analyses of extracts from the same liver tissues. They also provided equivalent quantitative information and localization of RIF throughout a liver dosed *in vivo* indicating different mass analyzers can be used and compared for quantitative MALDI IMS analyses. The linear ion trap mass spectrometer provided better sensitivity and spatial resolution (350 μm vs. 1 mm) for the analyses, but the TOF/TOF allows for structurally similar drugs to be analyzed using multiplexed MS/MS. If an isotopically labeled internal standard is not available or is too expensive to synthesize, the TOF/TOF mass spectrometer is one alternative for quantitative MALDI IMS.

As described in Chapter IV, quantitative MALDI IMS was also performed on kidneys dosed *in vivo* with PMZ to elucidate its quantitative distribution in a heterogeneous tissue section. Calibration curves of PMZ were applied to different tissue types yielding nearly identical calibration curves. The internal standard accounted for any ionization efficiency or extraction differences caused by the different tissue types. However, the limits of quantitation must be verified for the different tissue types, because they may be different. Once the limits of quantitation are verified, it may be possible to analyze a single set of calibration solutions for all

tissue types in an experiment. This is especially important for reducing the analysis time of heterogeneous tissue types and whole animal studies.

Future Research Directions

The capabilities of a high-speed, continuous laser raster sampling MALDI TOF/TOF mass spectrometer with multiplexed MS/MS have not been fully explored. Though the mass-to-charge ratio (m/z) difference for individual precursor ions must be greater than 6-7%, any number of precursor ions could theoretically be analyzed as long as they meet this requirement. In these experiments, three MS/MS isolations were performed in a single laser shot. The addition of other drugs to the quantitative drug assay would improve the applicability of the analysis to clinical samples. Other applications where multiplexed MS/MS analysis would be beneficial must also be explored. A pharmaceutical drug panel for a particular class of drugs or the analysis of specific lipids in an imaging experiment could benefit from this technology. This allows for the structural confirmation and analysis of all analytes of interest within a single analysis.

Currently, the microspotted method of quantitative MALDI IMS is limited by the spot size of the robotic spotter to a spatial resolution of approximately 250 μm . As previously mentioned, the spot size of the matrix microspots on tissue were approximately 200 μm in diameter for these experiments.⁹ The spatial resolution of many imaging experiments is approaching the sub-micron regime.^{10, 11} Robotic spotters having reduced droplet sizes and improved deposition accuracies may provide better resolution for future quantitative imaging experiments. For example, when the 28 MHz transducer on the acoustic robotic spotter was replaced with a 50 MHz transducer and the droplet volumes for 50% ethanol/water and 50% methanol/water

were measured, the droplet volume decreased from 171.3 pL to 133.3 pL and 169.7 to 133.4 pL, respectively. Furthermore, smaller droplet volumes and increasing the distance between the solvent reservoir and the MALDI target decreased the spot size diameter from 190 μm to 105 μm on water sensitive paper. With this spot size, quantitative MALDI MS images with spatial resolutions of around 150 μm may be achieved. Additionally, the use of inkjet printers to deposit the internal and/or calibration standards could be explored. Though they may clog when applying a nearly saturated matrix solution, the standards could be applied using the inkjet printer in much smaller spot sizes (~ 20 μm in diameter). After the standard application, a robotic sprayer for matrix application could be used to improve the spatial resolution.

The potential of robotic sprayers for quantitative MALDI IMS should also be thoroughly examined for improving the spatial resolution of quantitative MALDI IMS experiments.¹²⁻¹⁴ The homogeneity of the internal standard in a quantitative MALDI IMS experiment is imperative for the accuracy of the measurements. As demonstrated in these experiments, the robotic spotter allows for the reproducible deposition of a known amount of internal standard and calibration standards in microspots across the tissue. A robotic sprayer could be used to homogeneously coat the target before thaw-mounting the tissue sections or to homogeneously coat the tissue sections prior to matrix deposition, but the homogeneity must be validated. Furthermore, the two different methods of internal standard application with the sprayer must be analyzed to determine which best mimics the analyte when dosed *in vivo*. This could be examined using the standard tissue dosed *in vitro* developed herein if the homogeneity of the standard tissue is also validated on the smaller size regime. Additionally, methods for depositing calibration

standards must be developed and evaluated on the size scale of the pixels within the experiment.

Conclusions

The methods presented herein provide a foundation for high-speed MALDI TOF/TOF analyses, multiplexed quantitative MALDI TOF/TOF analyses, and quantitative MALDI IMS. As previously mentioned, these methods can be improved with additional pharmaceutical drugs or improving the spatial resolution of the quantitative MALDI IMS analysis. Nevertheless, the developments of multiplexed MS/MS on a high-speed MALDI TOF/TOF platform and quantitative MALDI IMS methodologies allowed for important advancements in the scientific community. MS/MS imaging of pharmaceutical drugs using a continuous laser raster sampling MALDI TOF/TOF mass spectrometer increases the speed of a typical analysis by 8-10 fold. Multiplexed quantitative MS/MS assays allow for higher throughput along with structural confirmation when screening plasma for different pharmaceutical drugs. Finally, quantitative MALDI IMS allows for the direct quantitation of pharmaceutical drugs in relation to histological and anatomical features within tissue sections, providing unparalleled information about drugs and their targets. This information is vital in the pharmaceutical discovery process in determining efficacy and potential toxicity.

References

1. D. A. Simmons, *Applied Biosystems Technical Note*, 2008, 1-5.
2. J. M. Spraggins and R. M. Caprioli, *Journal of the American Society for Mass Spectrometry*, 2011, **22**, 1022-1031.
3. B. M. Prentice, C. W. Chumbley and R. M. Caprioli, *Journal of Mass Spectrometry*, 2015, **50**, 703-710.
4. H. P. Gelbke, H. J. Schlicht and G. Schmidt, *Archives of Toxicology*, 1977, **37**, 89-94.
5. J. F. Koepke and A. J. McBay, *Journal of Forensic Sciences*, 1987, **32**, 1431-1434.
6. W. J. Allender and A. W. Archer, *Journal of Forensic Sciences*, 1984, **29**, 515-526.
7. D. Macdonald and P. C. Alguire, *American Journal of the Medical Sciences*, 1992, **303**, 115-117.

8. R. Skowronek, R. Celinski, M. Krzystanek, M. Korczynska, J. Kulikowska, J. Nowicka and C. Chowanec, *European Neuropsychopharmacology*, 2011, **21**, S498-S499.
9. C. W. Chumbley, M. L. Reyzer, J. L. Allen, G. A. Marriner, L. E. Via, C. E. Barry III and R. M. Caprioli, *Analytical Chemistry*, 2016, **88**, 2292-2398.
10. A. Zavalin, E. M. Todd, P. D. Rawhouser, J. Yang, J. L. Norris and R. M. Caprioli, *Journal of Mass Spectrometry*, 2012, **47**, 1473-1481.
11. G. Thiery-Lavenant, A. I. Zavalin and R. M. Caprioli, *Journal of the American Society for Mass Spectrometry*, 2013, **24**, 609-614.
12. J. Stauber, *Bioanalysis*, 2012, **4**, 2095-2098.
13. S. R. Ellis, A. L. Bruinen and R. M. A. Heeren, *Analytical and Bioanalytical Chemistry*, 2014, **406**, 1275-1289.
14. D. A. Pirman, *Bioanalysis*, 2015, **7**, 2649-2656.

APPENDIX

CURRICULUM VITAE

Education

Vanderbilt University, Nashville, TN (August 2010-Present)

- Ph.D. in Chemistry (Defense: March 21, 2016)
- Research Advisor: Richard M. Caprioli
- GPA: 3.94/4.00
- Dissertation: Absolute Quantitative Matrix-Assisted Laser Desorption/Ionization Mass Spectrometry and Imaging Mass Spectrometry of Pharmaceutical Drugs from Biological Specimens

Eastern Kentucky University, Richmond, KY (2006-2010)

- Bachelor of Science in Chemistry (American Chemical Society Certified)
- Bachelor of Science in Forensic Science (American Academy of Forensic Sciences Accredited)
- GPA: 4.00/4.00
- Honors Diploma and *Summa Cum Laude*

Research Experience

Vanderbilt University Department of Chemistry (August 2010-Present)

Graduate Research Assistant; Advisor: Dr. Richard M. Caprioli

- Developed methodology for a multiplexed quantitative MALDI TOF/TOF assay for pharmaceutical drugs (enalapril, verapamil, and promethazine) in plasma
- Developed methodology for pixel-to-pixel absolute quantitative MALDI imaging mass spectrometry (IMS) of drugs from tissue sections using isotopically labeled internal standards
 - Determined the optimal application method of an isotopically labeled internal standard to tissue sections using a novel standard tissue homogeneously dosed *in vitro*
 - Quantitatively analyzed tissue sections (livers and kidneys) from animals dosed with a drug (rifampicin or promethazine) using MALDI IMS and with HPLC-MS/MS
- Analyzed promethazine and amyloid beta peptide distributions in dosed brain tissue sections of an Alzheimer's disease mouse model (5XFAD) using MALDI IMS

Eastern Kentucky University Department of Chemistry (August 2008-May 2010)

Undergraduate Researcher; Advisor: Dr. Darrin L. Smith

- Titrated solutions of 2,6-dichlorophenolindophenol (DCIP) to develop an undergraduate chemistry laboratory demonstrating distribution coefficients
 - Performed spectroscopic analyses for DCIP quantitation and liquid-liquid extractions for visualization of the two DCIP forms after adding known volumes of hydrochloric acid

Louisville Water Company (June-August 2009)

Intern; Advisor: Dr. Rengao Song

- Researched methods for advanced water treatment to extend shelf-life of Louisville Pure Tap
- Performed water quality analyses, including QA/QC, on the drinking water at all stages of treatment

Publications

- **Chad W. Chumbley**, Michelle L. Reyzer, Jamie L. Allen, Gwendolyn A. Marriner, Laura E. Via, Clifton E. Barry III, Richard M. Caprioli. Absolute Quantitative MALDI Imaging Mass Spectrometry: A Case of Rifampicin in Liver Tissues. *Analytical Chemistry*. **2016**, DOI: 10.1021/acs.analchem.5b04409.
- Boone M. Prentice, **Chad W. Chumbley**, Richard M. Caprioli. High-speed MALDI MS/MS imaging mass spectrometry using continuous raster sampling. *Journal of Mass Spectrometry*. **2015**, *50*, 703-710.
- Richard A. McClure, **Chad W. Chumbley**, Michelle L. Reyzer, Kevin Wilson, Richard M. Caprioli, John C. Gore, Wellington Pham. Identification of promethazine as an amyloid-binding molecule using a fluorescence high-throughput assay and MALDI imaging mass spectrometry. *NeuroImage: Clinical*. **2012**, *2*, 620-629.
- Senior Honors Thesis: **Chad W. Chumbley**, Darrin L. Smith. "Development of a Novel Extraction Laboratory for Undergraduate Chemistry and Forensic Science Students." May, **2010**. Eastern Kentucky University Honors Program.

Presentations (Presenter Underlined)

Oral Presentations

- Boone M. Prentice, **Chad W. Chumbley**, Brian C. Hachey, Jeremy L. Norris, Richard M. Caprioli. Multiplexed TOF/TOF Analysis in a Single Laser Shot for Improved Quantification and Applications to MALDI Imaging Mass Spectrometry. 63rd American Society for Mass Spectrometry Conference on Mass Spectrometry and Allied Topics: St. Louis, MO, 2015.
- **Chad W. Chumbley**, Richard M. Caprioli. Spatially Correlated Analysis of Drugs in Tissue. Aegis Sciences Symposium: Vanderbilt University, Nashville, TN, 2014.
- **Chad W. Chumbley**, Richard M. Caprioli. Toward Quantitative MALDI Imaging Mass Spectrometry of Pharmaceuticals using Internal Standards. Chemistry 301 Seminar: Vanderbilt University, Nashville, TN, 2013.

Poster Presentations

- **Chad W. Chumbley**, Michelle L. Reyzer, Jamie L. Allen, Gwendolyn A. Marriner, Laura E. Via, Clifton E. Barry, III, Richard M. Caprioli. Validating Quantitative Imaging Mass Spectrometry of Pharmaceuticals in Tissue Sections. 63rd American Society for Mass Spectrometry Conference on Mass Spectrometry and Allied Topics: St. Louis, MO, 2015.
- Michelle L. Reyzer, **Chad W. Chumbley**, Michael DeLisi, Louise Mawn, Eva M. Harth, Robert Galloway, Richard M. Caprioli. Visualizing Brimonidine Distribution in Pig Optic Nerve Tissue by Imaging Mass Spectrometry. 63rd American Society for Mass Spectrometry Conference on Mass Spectrometry and Allied Topics: St. Louis, MO, 2015.
- **Chad W. Chumbley**, Michelle L. Reyzer, Jamie L. Allen, Gwendolyn A. Marriner, Laura E. Via, Clifton E. Barry, III, Richard M. Caprioli. Spatially Correlated Quantitative MALDI Analyses of Rifampicin in Liver. 62nd American Society for Mass Spectrometry Conference on Mass Spectrometry and Allied Topics: Baltimore, MD, 2014.
- Boone M. Prentice, **Chad W. Chumbley**, Richard M. Caprioli. Multiple MS/MS Transition Monitoring in a Single Laser Shot on a MALDI TOF/TOF Mass Spectrometer. 62nd American Society for Mass Spectrometry Conference on Mass Spectrometry and Allied Topics: Baltimore, MD, 2014.
- **Chad W. Chumbley**, Richard A. McClure, Michelle L. Reyzer, Wellington Pham, Richard M. Caprioli. Promethazine as a PET Probe for Amyloid Beta in Alzheimer's Disease using MALDI

Imaging Mass Spectrometry. 61st American Society for Mass Spectrometry Conference on Mass Spectrometry and Allied Topics: Minneapolis, MN, 2013.

- **Chad W. Chumbley**, Michelle L. Reyzer, Jamie L. Allen, Gwendolyn A. Marriner, Laura E. Via, Clifton E. Barry, III, Richard M. Caprioli. Quantitative Imaging Mass Spectrometry Using Internal Standards: A Case Study of Rifampicin in Rabbit Liver Tissue. 60th American Society for Mass Spectrometry Conference on Mass Spectrometry and Allied Topics: Vancouver, British Columbia, 2012.
- **Chad W. Chumbley**, Darrin L. Smith. Development of a novel extraction laboratory for undergraduate chemistry and forensic science students. 239th American Chemical Society Spring National Meeting and Exhibition: San Francisco, CA, 2010.
- **Chad W. Chumbley**, Darrin L. Smith. Utilizing 2,6-Dichlorophenolindophenol (DCIP) Towards the Development of a Novel Undergraduate Chemistry Laboratory for Distribution Coefficients. Kentucky Academy of Science's Annual Meeting: Northern Kentucky University, Highland Heights, KY, 2009.

Teaching Experience

- Roundtable Discussion Leader: Small Molecule Analysis, Advanced Imaging Mass Spectrometry Course, National Research Resource for Imaging Mass Spectrometry, Vanderbilt University (2014-2015)
- Workshop Designer and Leader: Manual Spraying, Advanced Imaging Mass Spectrometry Course, National Research Resource for Imaging Mass Spectrometry, Vanderbilt University (2012-2015)
- Workshop Designer and Leader: Linear Ion Trap, Advanced Imaging Mass Spectrometry Course, National Research Resource for Imaging Mass Spectrometry, Vanderbilt University (2012-2015)
- Teaching Assistant: CHEM 104B – General Chemistry II Lab, Vanderbilt University (Spring 2011)
- Teaching Assistant: CHEM 104A – General Chemistry I Lab, Vanderbilt University (Fall 2010)

Fellowships and Awards

Graduate

- Graduate Student Travel Fellowship (2012-2015)
- Aegis Sciences Corporation Fellowship (2012-2015)

Undergraduate

- American Chemical Society Analytical Chemistry Award (2009, 2010)
- American Chemical Society Inorganic Chemistry Award (2010)
- Top Chemistry Senior Award (2010)
- Top Forensic Science Award (2009, 2010)
- President's List (4.0 GPA) (2006-2010)
- Commonwealth Scholarship from Eastern Kentucky University (2006-2010)

Professional Affiliations, Memberships, and Leadership Roles

- American Society for Mass Spectrometry (2011-Current)
- American Chemical Society (2010-Current)
- Eastern Kentucky University Forensic Science Club (2007-2010)
 - President (2009-2010); Secretary (2008-2009)
- Golden Key National Honor Society (2007-2010)
- Delta Epsilon Iota (2007-2010)
- Eastern Kentucky University Honors Program (2006-2010)